Vector magnetometry using cavity-enhanced microwave readout of solid-state spin sensors

by

Erik Roger Eisenach

B.S. in EECS, The Citadel, The Military College of South Carolina (2015)
S.M. in EECS, Massachusetts Institute of Technology (2018)

Submitted to the Department of Electrical Engineering and Computer Science
in partial fulfillment of the requirements for the degree of

Doctor of Philosophy in Electrical Engineering and Computer Science

at the

MASSACHUSETTS INSTITUTE OF TECHNOLOGY

May 2022

Author .....
Department of Electrical Engineering and Computer Science
May 09, 2022

Certified by .....
Dirk R. Englund
Associate Professor of Electrical Engineering and Computer Science
Thesis Supervisor

Accepted by .....
Leslie A. Kolodziejski
Professor of Electrical Engineering and Computer Science
Chair, Department Committee on Graduate Students

Vector magnetometry using cavity-enhanced microwave readout of solid-state spin sensors

by

Erik Roger Eisenach

Submitted to the Department of Electrical Engineering and Computer Science
on May 09, 2022, in partial fulfillment of the
requirements for the degree of
Doctor of Philosophy in Electrical Engineering and Computer Science

Abstract

Robust, high-fidelity readout is central to quantum device performance. Overcoming poor readout is therefore an increasingly urgent challenge for devices based on solid-state spin defects, particularly given their rapid adoption in quantum sensing, quantum information, and tests of fundamental physics. However, in spite of experimental progress in specific systems, solid-state spin sensors still lack a universal technique for high-fidelity readout. One leading research avenue is to engineer state-of-the-art microwave delivery systems which improve the coherent control of large spin ensembles as they are manipulated for readout. Another is to develop novel readout techniques that go beyond measuring optical fluorescence signals, which are often difficult to detect, and unique only to some solid-state spin systems. In this thesis, I discuss these two approaches, and begin by designing a three dimensional microwave resonator that overcomes the many shortcomings of conventional microwave delivery systems, which limit the readout fidelity of devices employing large spin systems. Next, I demonstrate a novel readout technique that provides high-fidelity, room-temperature readout of an ensemble of nitrogen-vacancy centers via strong coupling to a dielectric microwave cavity. This strong collective interaction allows the spin ensemble's microwave transition to be probed directly, thereby overcoming the optical photon shot noise limitations of conventional fluorescence readout. Applying this technique to magnetometry, I first build a proof-of-concept magnetometer with the capability of measuring magnetic fields along a single vector axis, with a sensitivity better than the optical shot noise limit of the system. I then expand on the initial demonstration, by building a prototype capable of measuring three-dimensional dynamic vector fields with high sensitivity. While the current device performance is limited by technical noise, the method promises what has long been elusive for quantum sensors based on solid-state spin ensembles: a clear path to readout at the spin-projection limit.

Thesis Supervisor: Dirk R. Englund
Title: Associate Professor of Electrical Engineering and Computer Science

Acknowledgments

The past seven years have been an incredibly challenging, but rewarding experience. Without the support of so many others, this thesis would likely have never been completed. I want to start off by thanking my two advisors Dirk Englund and Danielle Braje for all the work they put into allowing me to complete the research presented here. I want to thank Karl Berggren for being a member of my thesis committee, and for always being available to discuss my progress. In addition, I want to thank Leslie Kolodziejski for all her time and advice in helping me navigate the final months of my PhD. I also want to highlight all the people who were integral to the successful completion of all this work. In particular, I want to thank John Barry and Michael O'Keeffe for their outstanding work in bringing both the experiment and the theory of cavity-enhanced microwave readout to fruition. I also want to thank Jennifer Schloss and Matthew Steinecker, without whom the resulting paper would have never been as thorough and clear as it is today. I also want to thank Linh Pham for all her efforts on the loop gap resonator project, and for meeting the challenge of transforming the cavity-enhanced microwave readout magnetometer from an initial demonstration to a full three-dimensional vector magnetometer. In conjunction, I also want to thank Henry Timmers, Kurt Vogel, Kevin Knabe, Jason Pinon, Jessica Kedziora, Jacob Harburg, Monica Coakley, and others for their work.

In the Quantum Sensing Laboratory at Lincoln, I would like to thank my fellow graduate students Scott Alsid and Reginald Wilcox. They are both amazing engineers and scientists, and I wish them all the best in their future endeavors. I also want to thank Quantum Sensing Lab friends and alumns Ed Chen, Hannah Clevenson, and Carson Teale, for always providing guidance and giving great advice. In the Quantum Photonics Laboratory at MIT, I want to thank all my good friends including Michael Walsh, Eric Bersin, Mihika Prabhu, and many others. Outside of the laboratory I thank my friends Joseph and Rebecca Finley, and Josué Lopez and Jessica Ruiz, for keeping me sane these past years with lots of laughter and good times. I want to thank Marvin and Susan Krause (the best in-laws anyone could ask for) for their love and support, and my Grandma Carmen, Aunt Sheila, Uncle Dave, Gordon, and others in my family who have supported me in my journey. I want to thank

my father Hans Eisenach, and my mother Paula Eisenach for their love and hard work in shaping me into the person I am today. And, finally, I want to thank my wonderful wife Monique Eisenach, who has lived through the pain of long nights and weekends lost to me working in the laboratory. Her sacrifices enabled me to complete my PhD, and, without her support, I would have given up many years ago. I look forward to all our future adventures together, and to spending time with our new puppy and family member Ripley.

I want to dedicate this thesis to my mom, Paula Eisenach. Her resiliency in life taught me what it really means to be tough. Without her influence, none of this would have been possible. I love and miss her every day.

The Lincoln Laboratory portion of this thesis is based upon work supported by the Under Secretary of Defense for Research and Engineering under Air Force Contract No. FA8702-15-D-0001. Any opinions, findings, conclusions or recommendations expressed in this material are those of the author(s) and do not necessarily reflect the views of the Under Secretary of Defense for Research and Engineering.

Contents

List of Figures

List of Tables

Chapter 1

Introduction

The term quantum sensor describes a host of different technologies [10, 13, 86, 88, 139, 170], designed for a multitude of different modalities [32, 47, 74, 92, 107, 113, 116, 156, 175, 179] and application spaces [43, 121, 173, 181]. Although technologies vary greatly, each device class shares the same basic function: it exploits quantum phenomena to measure weak or nanoscale signals. The advantage quantum sensors therefore have over their classical counterparts, lies in that their outputs are tied to fundamental constants which are not affected by the mechanical or electrical properties of the device [29]. Quantum sensors have therefore achieved a number of impressive feats including record breaking sensitivity [36,141], and stability [22,47,114]. By improving the ability to measure incredibly small signals at long timescales, humanity unlocks the capability to, for example, explore new physics [59, 104], develop new medical devices [37, 130], and even peer deeper into the history of our own universe [45, 104].

Among sensor modalities, magnetometry has garnered particular interest as a vast array of natural phenomena produce magnetic fields which convey information about their underlying physical systems. For example, measuring the weak magnetic signatures of the brain produced by neuronal activity, can allow the examination of the neural correlates of motor coordination, and describe their breakdown in movement disorders [25, 68, 133]. Paleomagnetic studies of primitive meteorites can yield insights into planetary formation within solar nebulae [61]. And studies of the magnetic field produced by charge carriers, can aid in understanding the complex nature of transport phenomena in all modern electronics, opening

pathways to engineering smaller and more efficient devices [157].

Among magnetometry applications, many require the ability to measure both the magnitude and direction of the magnetic fields under study [19, 41, 63, 67, 96, 98, 99, 165, 166, 168]. In three dimensional space, this is usually accomplished by measuring the projection of the vector field along three linearly independent axes. As a result, vector-projection magnetometers use multiple sensors aligned along different orientations, which can lead to heading errors if these orientations drift over time [100, 128]. Solid-state quantum sensors are therefore attracting wide interest, as their fixed crystallographic axes allow for complete vector field sensing, free from systematic drifts [41, 97, 103, 115]. The negatively charged nitrogen-vacancy (NV^-) defect center in diamond is a particularly promising solid-state platform, as it combines the capability for long term stability, high dynamic range, and low power operation into a single compact sensor package [85, 151]. The NV^- center's excellent coherence properties at room temperature also allow high sensitivity operation [11, 12, 17], however NV-based magnetometer systems have been held back by poor readout [14], and have yet to perform even close to the standard quantum limit.

Conventionally, NV centers and other solid-state systems are read out via optically detected magnetic resonance (ODMR). However, spin readout via optical excitation and fluorescence detection destroys the information stored by a spin defect with only a few scattered photons. Imperfect optical collection then ensures that on average far less than one fluorescence photon is typically detected per spin [156]. Moreover, spin fluorescence contrast (i.e., the normalized difference in signal from the qubit states) is far below unity, which further reduces the quantum information that conventional readout can extract from a given spin. Hence, quantum sensors employing solid-state spin ensembles with conventional optical readout exhibit sensitivities much worse than the spin-projection noise limit, with readout fidelities $\mathcal{F} \ll 1$ limited by shot noise on the detected fluorescence [14]. Here $\mathcal{F} = 1$ characterizes a measurement at the spin-projection noise limit, and $1/\mathcal{F}$ denotes the measurement uncertainty relative to that limit. In response, many alternative readout methods have been proposed and demonstrated [26, 71, 77, 81, 112, 142, 146, 149], but so far these techniques either introduce substantial overhead time [23, 71, 77, 81, 102, 112, 142] (diminishing achievable sensitivity) or offer only modest improvements over conventional optical readout [31, 149].

Regardless of the readout method employed, and with few exceptions [3, 167], solid-state spin systems require the application of microwave magnetic fields. Conventional optical readout in particular, requires that the applied field is strong and homogeneous to ensure little degradation to the spin fluorescence contrast. As the magnetic sensitivity is improved by increasing the number of interrogated spins [47, 156], many devices employ large diamond samples with high NV densities. For most microwave systems however, magnetic fields decrease by the distance squared between the sample and antenna, which makes engineering large volume strong and homogeneous microwave fields exceptionally challenging. This thesis therefore begins in chapter 2, by introducing a novel microwave delivery system which overcomes the many shortcomings of conventional microwave architectures that limit the optical readout fidelity of devices employing large solid-state spin ensembles. To overcome the sensitivity limitation due to shot noise on the detected fluorescence, Chapter 3 then shows that readout can be performed directly by measuring the interaction between the microwave field and the spin ensemble. As such interactions are generally too weak on their own to cause any perceptible changes in a microwave field, they can be enhanced by many orders of magnitude by placing the spin ensemble into a high-quality factor microwave resonator. Chapter 4 applies this technique to magnetometry by developing a proof-of-concept magnetometer which overcomes the shot noise limitation inherent in conventional optical readout, and measures magnetic fields with high sensitivity along a single vector orientation, albeit with measurement ambiguities if the field is not perfectly aligned with the sensing axis. Finally, Chapter 5 expands on the initial demonstration by developing a full vector magnetometer, capable of measuring three dimensional dynamic vector fields with high-sensitivity.

Chapter 2

Broadband loop gap resonator for nitrogen

This chapter is adapted from:

> "Broadband loop gap resonator for nitrogen vacancy centers in diamond," E. R. Eisenach, J. F. Barry, L. M. Pham, R. G. Rojas, D. R. Englund, and D. A. Braje. Review of Scientific Instruments 89, 094705 (2018)

2.1 Introduction

With notably few exceptions [3,167], all NV applications rely on employing microwave (MW) magnetic fields to drive dipole transitions between the NV ground state Zeeman sublevels. A number of these applications additionally require generation of strong and uniform MW magnetic fields over large areas ($\gtrsim$10 mm^2) or volumes ($\gtrsim$30 mm^3) [40,61,66,96,171]. In this chapter, I discuss the design considerations for a suitable MW delivery mechanism, fabricate a hole-and-slot type loop gap resonator (LGR), and evaluate its performance for relevant NV applications.

Two examples of application modalities that benefit significantly from large detection areas and volumes are multi-channel imagers and highly sensitive, single-channel bulk sensors, respectively. In the case of multi-channel imagers, increasing the detection area extends the measurement field-of-view, whereas for bulk sensors, increasing the detection volume can

considerably enhance measurement sensitivity. For example, the shot-noise-limited sensitivity of an NV magnetometer is approximately given by [156]

$$\eta \approx \frac{\hbar}{g_s \mu_B} \frac{1}{C\sqrt{\beta\tau}} \frac{1}{\sqrt{N}}, \tag{2.1}$$

where N is the number of NV sensors, τ is the duration of the measurement, C is the measurement contrast, β is the number of photons collected per NV per measurement, μ_B is the Bohr magneton, $g_s \approx 2.003$ is the ground state NV^- Landé g-factor [57], and $\hbar$ is the reduced Planck constant. The magnetic sensitivity can be improved by increasing N, achievable through higher NV density or larger detection volumes. However, NV ensemble coherence times, which limit the optimal measurement time τ, depend inversely on NV density [156]. As a result, without employing alternate techniques, there is a practical upper bound on the NV density after which further sensitivity enhancements are attained by increasing the measurement volume. Therefore, generating MW magnetic fields over large volumes can increase the number N of NV sensors addressed and consequently improve measurement sensitivity. For application modalities such as those discussed above, the MW field also requires both high power and uniformity over the full measurement region in order to achieve high-fidelity quantum-state manipulation and consequently high measurement contrast C. Finally, a MW delivery geometry with maximal optical access enables the collection of maximal number of photons β per NV per measurement.

2.2 Resonantly enhanced microwave driving

Standard approaches to applying MW drive to NV ensembles or other solid state spin systems include shorted coaxial loops [34, 40], microstrip waveguides [6, 178], coplanar waveguides [80, 177], and other coaxial transmission line approaches [111]. While such broadband approaches allow arbitrary drive frequency, the lack of resonant enhancement forces a compromise between the volume addressed (assuming a fixed homogeneity is required) and MW magnetic field strength, denoted B_1. Planar lumped-element resonators such as split-ring resonators [18, 178], planar-ring resonators [134, 160], omega resonators [72, 73, 143, 160], and

patch antennas [178] forego the flexibility of broadband solutions in favor of resonantly enhanced magnetic fields, thus enabling MW driving over larger regions. For example, the split-ring resonator presented by Bayat *et al.* achieves a MW field strength of $B_1 = 5.6$ G at 27 dBm of input power and a fractional root-mean-square inhomogeneity of $\sigma_{\mathrm{rms}} \approx 4.4\%$ over a ~ 1 mm^2 area [18]. However, such planar structures are ill-suited to providing good B_1 homogeneity away from the plane of fabrication. The community has addressed this shortcoming by employing a variety of three-dimensional resonators. Enclosed metallic cavity resonators [132], enclosed dielectric resonators [28, 44, 95], and certain three-dimensional lumped element resonators [7] all allow for good homogeneity over large volumes but unfortunately offer restricted optical access. As all-optical initialization and readout is a primary benefit for many solid-state spin systems, including NV-diamond [50], such a trade-off is incompatible with many existing and envisioned applications [135]. Open dielectric resonators [83, 94] provide good homogeneity and exhibit improved optical access, but with high Q-factors (in excess of 1,000) and consequently narrow bandwidths. As a result, such resonators are generally not able to drive multiple NV Zeeman resonances simultaneously or in rapid sequence, as is necessary for a number of magnetometry applications employing NV ensembles [39, 40, 103, 136, 177].

To address these shortcomings in a single MW delivery option, I present a three-dimensional tunable LGR, which is capable of generating strong, uniform MW magnetic fields over large length-scales and broad frequency bands while also allowing a high degree of optical access. The design is based on the anode block of a hole-and-slot-type cavity magnetron and utilizes resonant enhancement to achieve the desired MW drive strengths over large areas (>50 mm^2) and volumes (>250 mm^3). The design has an open geometry; for interrogation volumes centered within the LGR, approximately half of the 4π solid angle remains optically accessible. Importantly, for semi-standardized commercial diamond plates (2-4.5 mm side lengths with 0.5 mm thickness) this solution allows maximal access to the diamond's large front and back faces. The open access, good homogeneity, and high B_1 fields over the 8 mm diameter by 5 mm thickness cylindrical volume make the device well-suited both for wide-field magnetic imaging—applicable to studies of living systems [15, 46, 92, 96], early earth rocks or meteorites [61, 66], single cells [67], electronic devices [144], etc.—and for single-

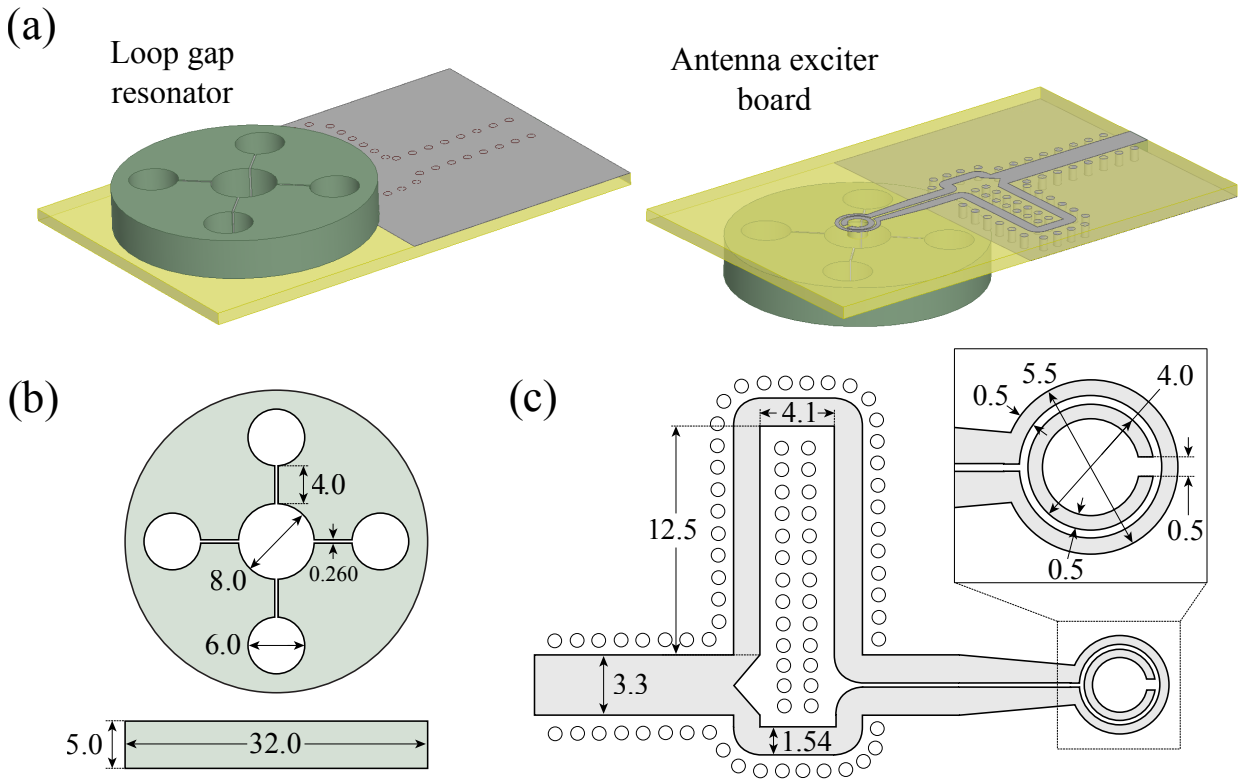

Figure 2-1: **Loop gap resonator and exciter antenna board.** (a) The metallic resonator employs a five-loop four-gap architecture. Microwaves are coupled into the LGR via the exciter antenna, which is fabricated on a printed circuit board. (b) Line drawing of LGR. (c) Exciter antenna. A feedline, 50:50 power splitter, and balun (**bal**anced **un**balanced) feed the split ring resonator, which is coupled to the LGR. The split-ring resonator has an inductance of 36 nH and a capacitance of 16 fF. All spatial dimensions are in mm. Optional mounting holes and radial access port for laser excitation are not shown.

channel bulk sensing [2, 15, 31, 40, 171] targeting, for example, geosurveying or space weather monitoring.

2.3 Microwave resonator design

A standard hole-and-slot LGR with n outer loops may be approximated as n coupled LC resonators oscillating in tandem [172]. Circulating currents around the central and outer loops create a total inductance L, given by [172]

$$L \approx \frac{1}{\frac{1}{L_c} + \frac{1}{nL_o}}, \tag{2.2}$$

where L_c and L_o denote the inductance of the central loop and of a single outer loop, respectively. Similarly, the n narrow capacitive gaps create a total capacitance C, which is given by [60]

$$C \approx \frac{\epsilon_r \epsilon_0 A}{nd}, \tag{2.3}$$

where A and d are the capacitive gap side wall area and separation, respectively. The resonant frequency of the LGR is therefore given by

$$f_0 = \frac{1}{2\pi\sqrt{LC}}. \tag{2.4}$$

In practice, the central loop diameter is set to ∼5-10 mm, corresponding to the typical size of a diamond plate, whereas d is limited by practical machining tolerances and ϵ_r by physically available materials. The capacitive gap area A is constrained by the dual LGR design objectives of (i) maintaining optical accessibility, which limits the thickness of the LGR device, and (ii) bounding f_0 above the target resonant frequency in order to allow for further tuning via shims (discussed below). Additionally, while increasing the number n of loops and gaps can improve B_1 uniformity [120], this approach results in a denser mode spectrum [60] and increases the likelihood of cross-mode excitations deleteriously altering the field distribution within the central loop. As a compromise, our design employs $n = 4$ outer loops [Fig. 2-1b], thus allowing for percent-scale uniformity over the specified area and volume (see section 2.6.1) while locating the closest eigenmode more than 1.5 GHz below the TE_{01} eigenmode.

The LGR detailed in this work consists of a central loop of radius $r_c = 4$ mm surrounded by $n = 4$ symmetrically arranged outer loops of radius $r_o = 3$ mm, as shown in fig. 2-1b. The outer loops return magnetic flux to the central loop and therefore oscillate antisymmetrically with the central loop (180° out of phase). The side walls of the capacitive gaps are separated by $d = 260$ μm. With these dimensions, Eqns. 2.2 and 2.3 predict $L = 8.7$ nH and $C = 0.17$ pF respectively, resulting in an expected resonant frequency for the naked air-gapped LGR of $f_0 = 4.1$ GHz, approximately 1.2 GHz above the NV resonance frequencies. For comparison, the measured f_0 for the air-gapped resonator is in the 4.6-4.9 GHz range. The discrepancy between the calculated and measured f_0 arises from the use of idealized physical models in

Eqs. 2.2 and 2.3, which do not account for higher order effects such as fringing electric or magnetic fields at the loop-gap boundary [172].

The LGR resonant frequency f_0 is additionally tuned by inserting and translating dielectric shims in the LGR's capacitive gaps, thereby increasing total capacitance C until f_0 overlaps the NV resonance frequencies as desired. As shimming material, we employ 200 μm thick C-plane sapphire, which is commercially available in semiconductor grade 50.8 mm diameter wafers, can be cut on standard wafer dicing saws, has a high relative permittivity of $\epsilon_r = 11.5$ parallel to the C-plane [162] (allowing for a large tuning of f_0), and exhibits low dielectric loss ($\mathrm{Tan}\,\delta < .0001$ at 3 GHz [69, 162]). The sapphire shims are cut to lengths longer than the $l_c = 4$ mm radial length of the capacitive gaps, wrapped in PTFE thread tape, and securely wedged into the $n = 4$ capacitive gaps. The sapphire shims are then translated radially until the desired value of f_0 is attained. To confirm that this method of securing the shims is stable, we measured the LGR S-parameter spectrum over 48 hours (Keysight N5232A PNA-L). During this time period, no shifts in the resonant frequency f_0 were observed down to the approximate precision of the measurement ($\sim$ 1 MHz). For applications with stricter mechanical stability requirements, the shims can be additionally secured post-tuning by applying low-loss epoxy or optical adhesive. The shims are positioned so that excess shim length extends into the outer rather than the central loop, in order to minimally perturb the central loop B_1 field. Radially symmetric shim configurations produce the highest B_1 field homogeneity, as asymmetries in shim placement perturb the desired TE_{01} field distribution. Insertion and removal of diamonds in the LGR center loop has a negligible effect on f_0, as the large electric fields of the TE_{01} mode are predominantly confined to the capacitive gaps, both in the case of the naked air-gapped LGR and to a larger extent in the case of the sapphire-shimmed LGR.

2.4 Resonator coupling

Incident MW power P is inductively coupled into the LGR by an exciter antenna, composed of a split ring resonator that is differentially driven by a microstrip balun, as shown in Fig. 2-1c. The differential driving mitigates common-mode noise on the two traces, which might

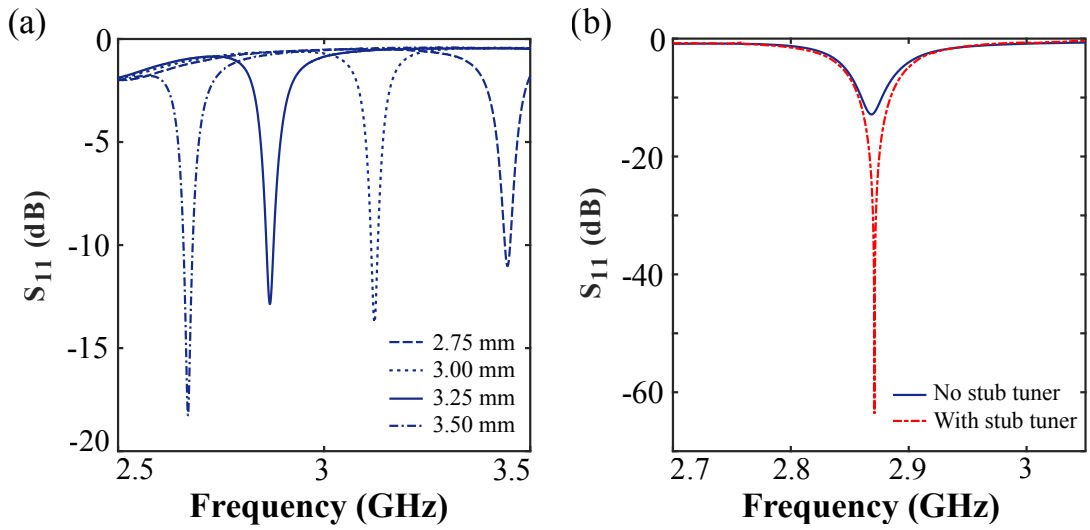

Figure 2-2: **Frequency tuning and impedance matching of LGR composite device.** (a) The resonant frequency f_0 is adjusted by translating the sapphire shims in the four capacitive gaps. In the absence of a stub tuner, the LGR composite device exhibits S_{11} values between -10 and -20 dB from 2.5 to 3.5 GHz, indicating $\gtrsim 90\%$ of power delivered to the LGR composite device contributes to B_1 in this range. (b) Nearly perfect critical coupling can be achieved with a stub tuner, allowing practically all incident MW power to contribute to B_1.

otherwise couple to the split-ring resonator. Although the microstrip balun is designed to match the feed-line and the split ring component of the exciter antenna at frequencies near 2.87 GHz, good matching is achieved over the broader range from 2.5 GHz to 3.5 GHz. For drive frequencies between 2.5 and 3.5 GHz, the exciter antenna board couples more than 90% of incident MW power into the LGR, as shown in fig. 2-2a. For a specific fixed frequency, the impedance matching may be further optimized by inserting a stub tuner between the MW source and the exciter antenna board [Fig. 2-2b]. Modification of the exciter circuit impedance via the stub tuner leaves the antenna magnetic field distribution largely unperturbed.

A via shield along a portion of the balun helps reduce interference and cross-talk between traces, controls the trace impedance, and reduces radiative losses along the balun's π-phase delay arm. The exciter antenna is fabricated from a 1 oz. copper trace with immersion silver finish on 1.524 mm thick dielectric (Rogers RO4350B, $\epsilon_r = 3.66$ at 3 GHz). Although the proximity of the split ring resonator perturbs the field distribution inside the LGR, both

simulations and measurements confirm this effect is small and not the dominant inhomogeneity source (see section 2.6.1). For applications intolerant of such perturbations or those requiring maximal diamond optical access, we achieved similar success inductively coupling a small coil of radius $\approx r_o$ to one of the outer loops [89], where the coil is translated (via mechanical stage) until the desired coupling is achieved. We expect this coupling method to be particularly suitable for laboratory or clinical imaging applications.

2.5 Effects of microwave field inhomogeneity on magnetic sensitivity

Section 2.1 discusses the ways in which the MW delivery design affects magnetic sensitivity, given approximately by Eq. 2.1. In particular, the degree of optical accessibility affects the number of photons β collected per NV per measurement; the volume over which the MW field is generated affects the number N of NV sensors that can be addressed in a measurement; and the strength and uniformity of the MW field affect the measurement contrast C. To provide more detail on the last dependency and to illustrate the importance of field uniformity, we simulated the measurement contrast achieved with the LGR design presented in this work and compared it against that achieved using solely the split-ring resonator design depicted in fig. 2-1c.

As discussed previously, split-ring resonators provide resonant enhancement and higher MW field uniformity compared to more conventional broadband approaches, such as loops, waveguides, and other coaxial transmission line geometries. However, split-ring resonators and other planar designs exhibit poor uniformity perpendicular to the plane of fabrication, and further, the MW magnetic field direction often varies significantly near the electrically conducting elements. Both effects cause variation in the NV Rabi frequency Ω_R over the measurement volume, consequently degrading the average measurement contrast and sensitivity. To illustrate, we first simulated the MW magnetic vector field generated in a volume above the split-ring resonator and in an equivalent volume centered in the central cavity of the LGR. We then calculated NV Rabi frequency, which, as discussed in section 2.6.1,

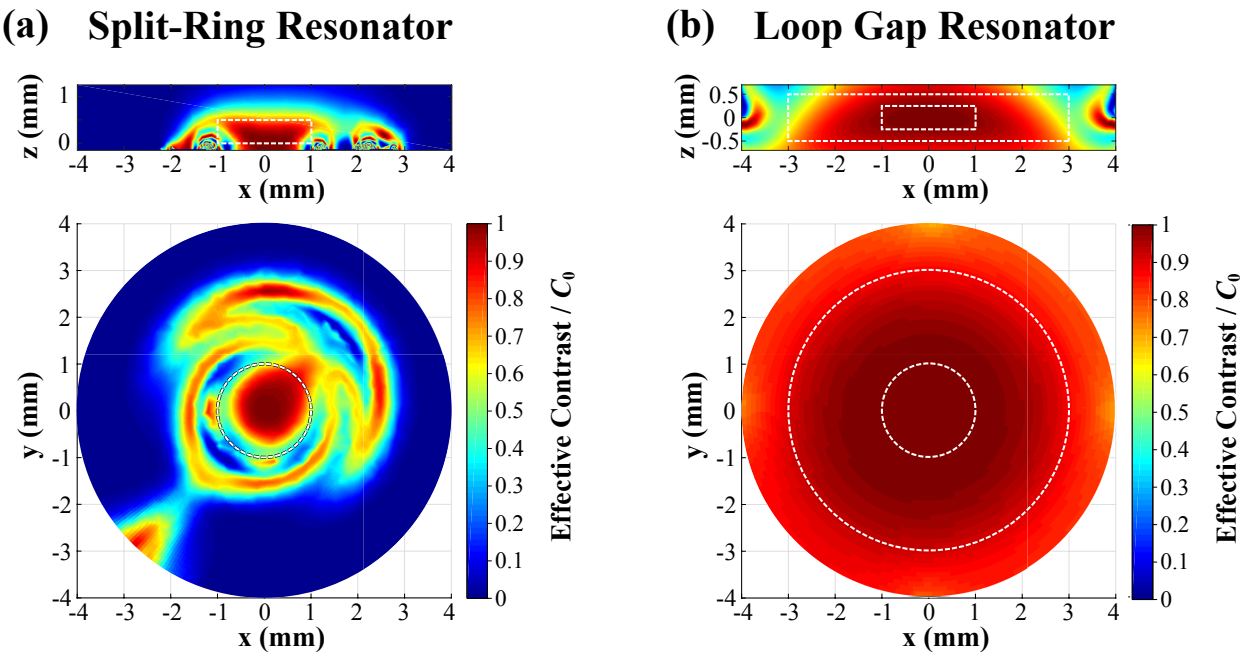

Figure 2-3: **Measurement contrast inhomogeneity.** (a) Effective contrast variation due to inhomogeneities in the MW magnetic field generated by the split-ring resonator. Cross-sections are shown at y = 0 mm in the xz plane (top) perpendicular to the split-ring resonator plane with ring centerline at x = 0 mm and the fabrication plane at z = -0.1 mm, and at z = 0.25 mm in the XY plane (bottom) parallel to the split-ring resonator plane. The measurement volume is separated from the split-ring resonator plane by a distance 0.1 mm for improved MW field uniformity within the volume and is indicated by the white dashed lines. (b) Effective contrast variation due to inhomogeneities in the MW magnetic field generated by the loop gap resonator. Cross-sections are shown at y = 0 mm in the xz plane (top) along the LGR symmetry axis with the LGR centered at z = 0 mm, and at z = 0 mm in the XY plane (bottom) perpendicular to the LGR symmetry axis. The measurement volumes are indicated by the white dashed lines.

is proportional to the MW magnetic field component *transverse* to the NV symmetry axis. However, since NV centers can be oriented along any of four possible crystallographic directions in single-crystal diamond, it was necessary to separately calculate Rabi frequencies corresponding to each NV orientation.

To relate NV Rabi frequency to measurement contrast, we note that in most standard pulsed measurement protocols, finite MW pulses are applied to coherently manipulate the NV spin states. For example, a MW π pulse of Rabi frequency Ω_R and duration $\tau = (\pi/\Omega_R)$ may be applied to transfer the NV spin from the $m_s = 0$ to the $m_s = +1$ ground-state spin

sublevel. However, when the MW magnetic field and consequently the NV Rabi frequency are inhomogeneous over the measurement volume, the amount of rotation a MW pulse of fixed duration induces on an NV spin likewise varies over the volume. Thus, we next calculated the effective contrast C_{eff} as a function of Rabi frequency Ω_R for each NV orientation, employing a fixed MW pulse duration τ:

$$C_{\text{eff}} = \frac{C_0}{2}\left[1 - \cos(\Omega_R \tau)\right], \tag{2.5}$$

where C_0 is the maximal contrast, achieved when the NV spin undergoes a perfect π rotation. In an NV ensemble measurement, the normalized effective contrast is given by the average of all four NV orientations. Considering a measurement volume given by a cylinder of radius 1 mm and thickness 0.5 mm, we show cross-sectional slices of the normalized effective contrast for the split-ring resonator [Fig. 2-3a] and LGR [Fig. 2-3b]. The fixed MW pulse duration τ was set for each resonator individually using the duration of a π-pulse at the center-points of the cylindrical measurement volumes. The regions of high spatial variation near the electrically conducting elements of the split-ring resonator are the result of significant deviation in the MW field direction combined with the sinusoidal dependence in Eq. 2.5. Note that performing NV spin rotations significantly greater than the targeted π-rotation yields unpredictable behavior; consequently, operation in these highly fringed regions is ill-advised. The volume-averaged effective contrast is $0.79C_0$ for the split-ring geometry and $0.995C_0$ for the LGR geometry. From Eq. 2.1, this $\approx$25% difference in contrast corresponds to a 25% improvement in magnetic sensitivity achieved by the LGR compared to that achieved by the less uniform split-ring resonator.

Finally, it is worth noting that the LGR design's MW field is uniform over such an extended spatial range that even a larger measurement volume defined by a cylinder of radius 3 mm and thickness 1 mm results in only a $\approx$ 3% reduction in effective contrast averaged over the 18x increased measurement volume, which is proportional to the number N of NV sensors addressed. Thus, taking advantage of the LGR's uniform MW field to increase the measurement volume yields a net improvement in the magnetic sensitivity by a factor of $\approx$4.

2.6 Microwave loop gap resonator performance

2.6.1 Strength and homogeneity

The strength and homogeneity of B_1 within the LGR central loop is evaluated employing standard NV techniques, as described in detail in Ref. [119] and elsewhere [33,106]. A {100}-cut diamond plate containing $\sim 1 \times 10^{14}$ NV/cm^3 is mounted at the center of the LGR with the <100> crystallographic axis collinear with the LGR axis. A rare earth magnet creates a static magnetic bias field B_0, which shifts the energies of the $m_s = \pm 1$ ground-state Zeeman sublevels. The energy shifts are given to first order by [156]

$$\Delta E \approx \mathrm{g_s}\mu_\mathrm{B} m_s \vec{B}_0 \cdot \hat{n}_i, \tag{2.6}$$

where $\hat{n}_i$ denotes a unit vector oriented along one of the four diamond crystallographic axes. By judicious choice of $\vec{B}_0$, all eight energy levels and associated $m_s = 0 \leftrightarrow m_s = \pm 1$ magnetic dipole transitions can be isolated as shown in Fig. 2-4a. The resonator is tuned to excite a single NV transition, yielding Rabi oscillations [Fig. 2-4b]. The data is fit to an exponentially decaying sinusoid in order to extract the Rabi frequency Ω_R, from which the magnitude of B_1 can be calculated as

$$B_1 = \sqrt{3}\frac{\hbar\Omega_R}{\mathrm{g_s}\mu_\mathrm{B}}. \tag{2.7}$$

In this geometry, the B_1 field is oriented along the [100] crystallographic axis of the diamond, degenerately offset from all four NV axis orientations by half the tetrahedral bond angle $\theta_{\mathrm{tet}}/2 = \mathrm{ArcCos}\frac{1}{\sqrt{3}} \approx 54°$. NV Rabi oscillations are driven by the B_1 field component transverse to the NV symmetry axis, reducing the Rabi frequency by $\sqrt{2/3}$ [134]. Accounting for the rotating wave approximation introduces another factor of $1/\sqrt{2}$, resulting in the conversion factor $\sqrt{3}$ in Eq. 2.7. To ensure $\vec{B}_0$ is consistent for all measurements across the LGR central loop [Fig. 2-5a], the confocal excitation volume is held fixed with respect to the B_0-generating permanent magnet, and the diamond and LGR composite device are translated together. We employ a long working distance objective (Mitutoyo 378-803-3, M Plan Apo 10× NA=0.28) to collect the NV fluorescence; the 34 mm working distance is necessary to minimize perturbation of the B_1 field by the metal objective housing. Future

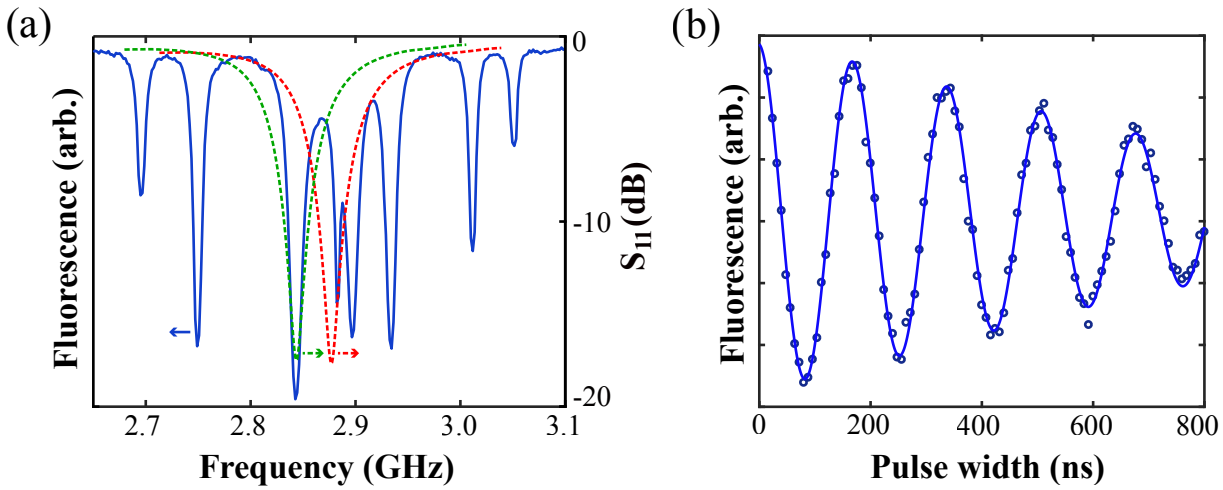

Figure 2-4: **LGR driving of an NV ensemble**. (a) The NV electron spin resonance spectrum (—) measured under the application of bias field B_0 with the LGR tuned to resonant frequency $f_0 = 2.84$ GHz. The bias field allows individual addressing of all eight NV resonances, arising from the combination of the two allowed magnetic dipole transitions with the four possible NV orientations. The NV hyperfine structure is obscured by MW power broadening and the contrast variation between the NV resonances is attributed primarily to the S_{11} line-shape, where the NV resonances closer to the LGR resonant frequency f_0 are driven more strongly and thus exhibit higher contrast. The S_{11} parameter is shown before (- - -) and after (- - -) shifting the LGR resonant frequency f_0 to the target NV resonance. Arrows indicate corresponding y axes. (b) Typical data depicting Rabi oscillations under MW excitation at the target NV resonance frequency indicated in (a). Data (∘) is fit (—) to an exponentially decaying sinusoid.

NV wide-field imaging applications may require ceramic-tipped objectives.

Application of incident MW power $P \approx 42$ dBm yields an axially oriented B_1 at the center of the LGR with magnitude 4.7 G. The corresponding Rabi frequency $\Omega_R = 2\pi \times 7.7$ MHz for NV centers oriented at half the tetrahedral bond angle relative to the LGR axis. Qualitatively, as shown in fig. 2-5c, B_1 displays a minimum at the LGR center, increases in magnitude with increasing radial displacement from the center, and is approximately radially symmetric. The highest homogeneity is therefore expected at the LGR center.

The B_1 field uniformity is quantitatively characterized using both the fractional root-mean-square inhomogeneity σ_{rms} and the fractional peak-to-peak variation $\sigma_{\mathrm{pp}} = \left[B_1^{\mathrm{max}} - B_1^{\mathrm{min}}\right]/B_1^{\mathrm{average}}$. The use of both metrics facilitates comparison with alternative existing designs. Over a 32 mm^2 circular area axially centered in the LGR central loop, we observe $\sigma_{\mathrm{rms}} = 3.2\%$ and $\sigma_{\mathrm{pp}} = 10.5\%$, as shown in fig. 2-5c. Over a smaller 11 mm^2 circular area, we

observe $\sigma_{\rm rms} = 1.6\%$ and $\sigma_{\rm pp} = 3\%$.

The LGR performance is modeled using a commercial finite element MW simulation package (Ansys HFSS). Simulations include the exciter antenna board and indicate that its magnetic field drops by a factor of >15 at a distance 4 mm away from the plane of fabrication. In addition, the electrically-conductive exciter antenna causes a small perturbation to the otherwise radially symmetric field (<2% maximum azimuthal variation) [Fig. 2-5b]. The simulation predicts $B_1 \approx 4.8$ G at the LGR center with incident MW power $P = 42$ dBm. Within a 32 mm^2 circular area centered in the LGR central loop, simulations indicate $\sigma_{\rm rms} = 3.8\%$ and $\sigma_{\rm pp} = 11\%$, whereas within a smaller 11 mm^2 circular area, simulations indicate $\sigma_{\rm rms} = 1\%$ and $\sigma_{\rm pp} = 2\%$. These simulation results are in good agreement with the measurements.

As a three-dimensional cavity resonator, the LGR provides better axial field uniformity than planar-only geometries [7, 83, 95]. For example, for a 3.14 mm^3 cylindrical volume (1 mm radius disk with 1 mm thickness), simulations yield $\sigma_{\rm rms} = 0.8\%$, $\sigma_{\rm pp} = 3.7\%$, and an average B_1 of 4.8 G.

2.6.2 Resonator power handling

Heat loads applied to the LGR composite system are expected to result in thermal drift and other non-linearities, degrading device performance and measurement reproducibility. For example, thermal expansion of the resonator slightly alters the values of L and C, causing the resonant frequency to shift. The main source of direct heating in the LGR composite system is incident MW power. Under the approximation that all MW power is dissipated by the finite resistivity of the titanium alloy, the heat load is expected to be the product of the MW power and the MW duty cycle. Fortunately, in standard pulsed NV measurement protocols, the MW power is applied with low duty cycle (in this work < 1.3%), resulting in little heating of the resonator. For example, the Rabi frequency measurements performed in this work employed a maximum MW pulse duration of 1 μs with input power 42 dBm. Using the specific heat capacity of Ti-6A-4V grade 5 titanium [≈ 0.526 J/(g·K)] and the resonator mass (≈ 14 g), a single MW pulse induces at most a ~ 2 μK increase in the average LGR temperature.

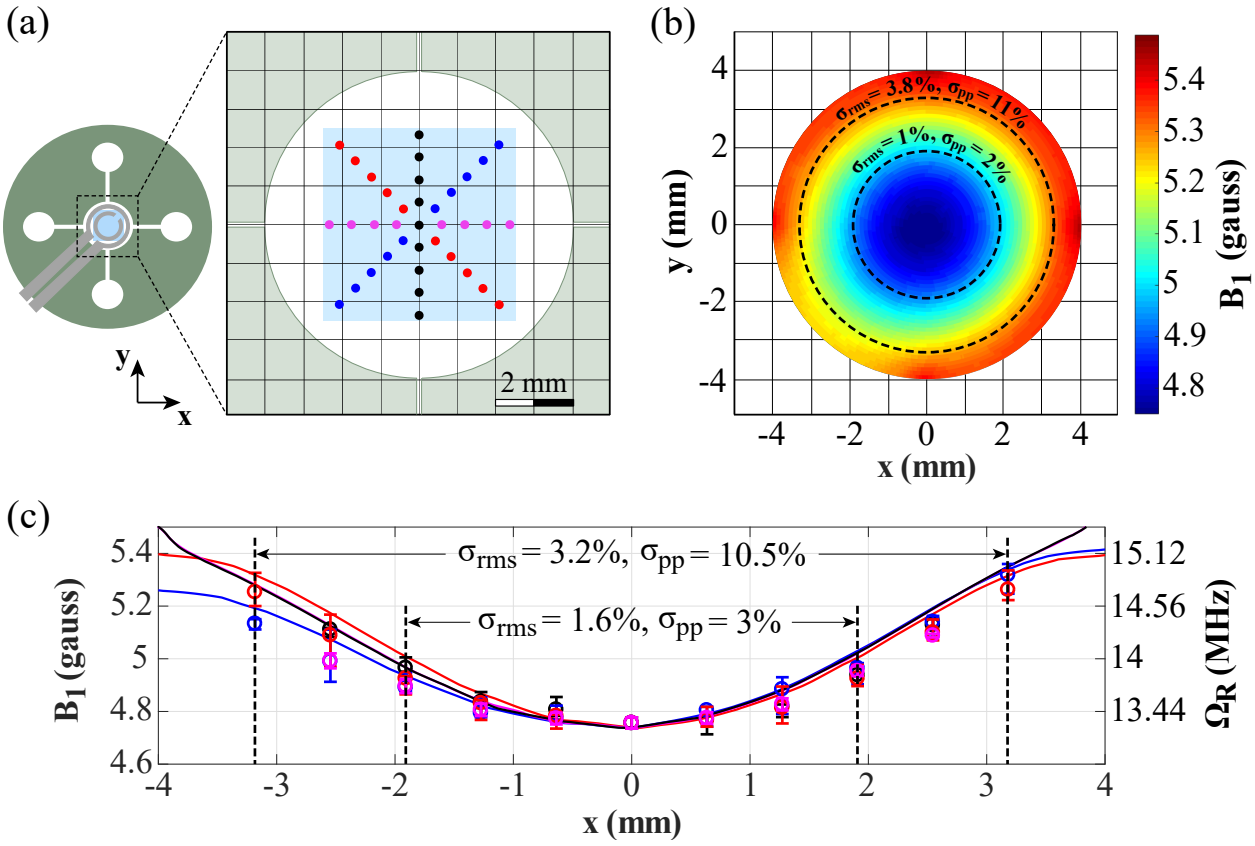

Figure 2-5: ***B*$_1$ field uniformity of LGR composite device.** (a) An NV-containing 4.5 mm × 4.5 mm diamond plate is placed in the LGR central loop, and the Rabi frequency is measured where indicated (•,•,•,•) to characterize B_1. (b) The B_1 field is simulated in an axial slice at the resonator center (symmetry plane of the LGR). The B_1 field distribution is approximately radially symmetric, with the leading order deviation resulting from the exciter antenna. Dashed lines indicate the 32 mm^2 and 11 mm^2 areas within which the B_1 field uniformity is evaluated. (c) B_1 field measurements (○,○,○,○) at the points depicted in (a) and simulations (–,–,–,–) along each locus of points are in good agreement. Error bars indicate 1-sigma uncertainty for the B_1 measurement. Dashed lines indicate the radial boundaries of the 32 mm^2 and 11 mm^2 areas over which B_1 field uniformity is evaluated. The measured B_1 uniformity is given for each area.

Measurements show the cavity resonant frequency shifts down by ∼ 6 MHz/Watt of time-averaged power applied to the device. Detailed analysis of thermal effects are beyond the scope of this chapter. For applications where heat loads induce undesirably large temperature shifts, the resonator can be affixed to an electrically insulating heat sink or heat spreader to more efficiently dissipate the input heat.

The LGR composite system may also experience indirect heating due to optical driving, which is applied in most NV measurements, typically at higher duty cycles compared to

those of MW driving. For example, the Rabi frequency measurements performed in this work employed an optical drive power of 13 mW at a duty cycle of ∼84%. Assuming at most half of the optical power is absorbed into the diamond as heat, the estimated increase in the diamond's equilibrium temperature is <1 K. Since the diamond is not in contact with the MW resonator, such a temperature change has negligible effect on the LGR temperature for the measurements performed in this work. However, significantly higher optical drive powers may be used in a number of the applications expected to benefit from employing the LGR design for MW delivery. For example, we have observed optical powers in excess of 4 W to increase the diamond equilibrium temperature by $\gtrsim$250 K. In this case, properly heat sinking the diamond can reduce indirect heating effects on the LGR.

It is also worth noting that heating of the system can additionally cause thermal expansion of the diamond mounting material, consequently displacing the diamond as a function of temperature. In this case, the LGR provides an important benefit: due to the high degree of MW field uniformity over long length-scales, the MW magnetic field experienced by the diamond is minimally affected by small displacements in its position within the resonator cavity. For example, displacing a 4 mm x 4 mm x 1 mm diamond axially by 0.1 mm causes a <0.05% change in the average MW field strength. However, if desired, diamond displacement can be minimized by employing mounting material with high heat capacity, low thermal expansion, and/or high thermal conductivity.

2.6.3 Axial field uniformity

Figure 2-6 plots the simulated magnitude of B_1 along the LGR's symmetry axis, illustrating the improved axial field uniformity possible with three-dimensional cavity resonators [7, 83, 95], compared to that of planar-only geometries. The presence of the split ring resonator at $z = 4.024$ mm perturbs B_1 inside the LGR, shifting the point of maximal B_1 down by 0.4 mm, away from the split ring resonator. Within a cylindrical volume of 3.14 mm^3 (1 mm radius and 1 mm thickness), centered around the point of maximal B_1, the simulation predicts $\sigma_{\text{rms}} = 0.78\%$ and $\sigma_{\text{pp}} = 3.7\%$. For a larger cylindrical volume of 12.6 mm^3 (2 mm radius and 1 mm thickness), the simulation predicts $\sigma_{\text{rms}} = 2\%$ and $\sigma_{\text{pp}} = 8\%$. These dimensions are comparable to those of commercially available single-crystal diamonds.

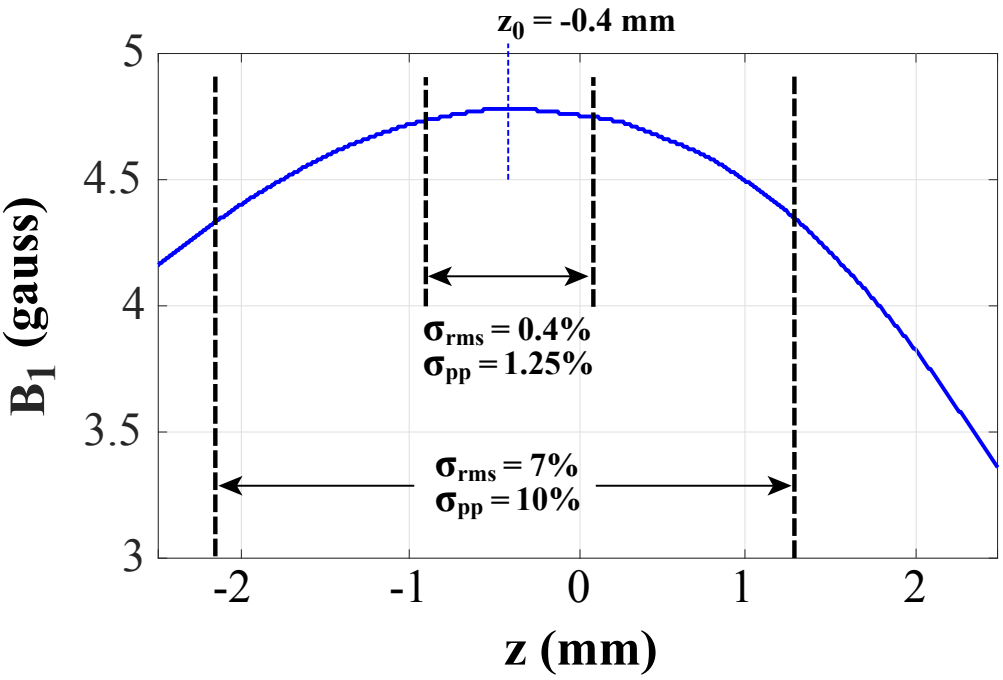

Figure 2-6: **Simulated B_1 field along LGR symmetry axis.** The symmetry plane of the LGR is located at $z = 0$ mm. The edges of the LGR are at $z = \pm 2.5$ mm, and the split-ring resonator is located at position $z = 4.0$ mm. The presence of the split-ring resonator shifts the point of maximal B_1 off center to $z_0 = -0.4$ mm.

Outside of the LGR cavity, the simulated magnitude of B_1 decays approximately exponentially as a function of distance from the LGR surface in the near field, resulting in a hundred-fold reduction in the field magnitude approximately 1.5 cm from either surface (in the absence of the split ring resonator). In the far field ($>10\lambda$), the LGR behaves like a dipole, with the MW field falling off as z^{-3}, where z is the axial distance from the LGR center.

2.7 Discussion

The device presented here exhibits further benefits, along with extensions tailored for specific applications. For example, for ubiquitously employed pulsed measurement protocols, a short ring-down time

$$\tau_{\text{ring}} = \frac{Q}{\pi f_0}, \tag{2.8}$$

(i.e., the characteristic time for B_1 to decay to $1/e$ times its maximum value) is necessary for high-fidelity pulse shape control. Although techniques to compensate for long ring-down times are effective [24, 117, 152], shorter native values of τ_{ring} are nonetheless generally desired [118, 129]. The observed loaded quality factor $Q_L = 36$ corresponds to a ring-down time of $\tau_{\text{ring}} = 4$ ns, making the device suitable for standard pulsed protocols [78, 148].

Due to square-root scaling of B_1 with incident MW power ($B_1 \propto \sqrt{P}$), higher power handling can allow for stronger B_1 fields. The non-planar resonator design allows for otherwise higher incident MW powers as currents circulate over an extended 2D surface (versus the 1D edge for a planar structure). Further, the metallic LGR thermal mass and thermal conductivity allow efficient heat transfer and sinking, resulting in improved device stability and power handling. The LGR composite device is expected to allow > 100 W for CW and pulsed operation, limited by dielectric breakdown of air in the 260 μm capacitive gaps. Should available MW power be constrained, stronger B_1 can be achieved by fabricating the LGR from a more electrically conductive material (e.g. silver or copper) at the expense of bandwidth. In such circumstances, the bandwidth can be continuously adjusted above its minimum value by over-coupling the resonator (at the expense of reduced Q_L).

While the presented LGR is 5 mm thick, the fundamental hole-and-slot approach is expected to be feasible for a variety of thicknesses. A thicker device will provide better field uniformity at the expense of optical access. In contrast, for applications requiring MW delivery over a thin planar volume, we expect the LGR can be fabricated via deposition on an appropriate insulating substrate, as discussed in Refs. [159, 160]. We have found semi-insulating silicon carbide [136] suitable due to the material's high thermal conductivity (≈490 W/(m·K) [125, 127], high Young's modulus, moderate cost, and wide availability in semi-conductor grade wafers. Our simulations suggest the planar LGR approach can offer modest improvements in B_1 homogeneity over split ring resonators.

As discussed previously, although the exciter antenna facilitates a compact, vibration-resistant, and portable device, this component introduces non-idealities in both field uniformity and optical access (see section 2.6.3). As similar scattering parameters are obtained by inductively coupling a small coil to one of the LGR outer loops, this latter solution may find favor for applications requiring maximal optical access and, furthermore, requires no PCB

fabrication.

2.8 Conclusion

In summary, this chapter presents an S-band tunable loop gap resonator (LGR), which provides strong, homogeneous, and directionally uniform broadband microwave (MW) drive for nitrogen-vacancy (NV) ensembles. With 42 dBm of input power, the composite device provides drive field amplitudes approaching 5 G over a circular area $\gtrsim 50$ mm^2 or cylindrical volume $\gtrsim 250$ mm^3. The wide 80 MHz device bandwidth allows driving all NV Zeeman resonances for bias magnetic fields below 20 G. The device realizes percent-scale MW drive inhomogeneity; we measure a fractional root-mean-square inhomogeneity $\sigma_{\mathrm{rms}} = 1.6\%$ and a peak-to-peak variation $\sigma_{\mathrm{pp}} = 3\%$ over a circular area of 11 mm^2 and $\sigma_{\mathrm{rms}} = 3.2\%$ and $\sigma_{\mathrm{pp}} = 10.5\%$ over a larger 32 mm^2 circular area. We demonstrate incident MW power coupling to the LGR using two methodologies: a printed circuit board-fabricated exciter antenna for deployed compact bulk sensors and an inductive coupling coil suitable for microscope-style imaging. The inductive coupling coil allows for approximately 2π steradian combined optical access above and below the device, ideal for envisioned and existing NV imaging and bulk sensing applications.

Chapter 3

Cavity-enhanced microwave readout of solid-state spin sensors

Portions of this chapter have appeared in print in the following publication:

> "Cavity-enhanced microwave readout of a solid-state spin sensor," E. R. Eisenach, J. F. Barry, M. F. O'Keeffe, J. M. Schloss, M. H. Steinecker, D. R. Englund, and D. A. Braje. Nature Communications 12, Article number: 1357 (2021)

3.1 Introduction

Quantum devices employing optically active solid-state spin ensembles promise broad utility [32, 47, 70, 113, 156] but are plagued by poor readout [14]. In this chapter, I demonstrate a non-optical readout technique for solid-state spin-ensemble sensors. The technique leverages strong collective coupling between a dielectric resonator cavity and a spin ensemble at room temperature. Similar coupled spin-cavity systems have recently been harnessed to demonstrate a room-temperature maser [28] and Dicke superradiance [27, 48]. Related cavity quantum electrodynamics (CQED) effects have also been employed for quantum information applications in cryogenic solid-state [5,8,9,76,91,95,124,126] and superconducting qubit [20, 163, 174] systems. Cavities also have been used to great effect in electron paramagnetic resonance (EPR) to amplify weak signals from samples under study [122], including

for the observation of the spectrum of a nitrogen-vacancy (NV) center in diamond on illumination with light [101]. Quantitative EPR spectroscopy remains an area of active research for biological, medical, and industrial applications [52]. Here I report the use of a strongly coupled, room temperature spin-cavity system for sensor applications, providing in detail new insights into optimization of such systems for sensing.

This advance promises what has long been elusive for quantum sensors based on solid-state spin ensembles: a clear avenue to readout at the spin-projection limit. Because the sensor's limiting noise source is independent of the number of polarized spin defects N, the device's sensitivity is expected to improve linearly with increasing N until the spin-projection limit is reached.

3.2 Results

The readout technique operates by measuring changes in an applied MW field following cavity-enhanced interactions with a spin ensemble. When the MW frequency is tuned near-resonant with the spin defect's resonance frequency, both absorptive and dispersive interactions occur [158]. These interactions encode the spin resonance in the amplitude and phase of the transmitted or reflected MWs. While the absorptive and dispersive interactions may be too weak on their own to cause perceptible changes in the MW field, even for a sizeable spin ensemble, these effects can be enhanced more than ten-thousandfold by placing the ensemble in a high-quality-factor cavity resonant with the applied MWs. Dispersion and absorption by the spin ensemble then modify the resonance frequency and linewidth of the composite cavity-spin system, respectively. Consequently, detection of the transmission through or reflection from the composite cavity provides readout of the spin resonance [52].

3.2.1 Experimental setup

In the experiments described here, NV^- defects are continuously initialized by applying 532 nm laser light. This optical pumping preferentially populates the spin-1 NV^- ground-state sublevel $|m_s = 0\rangle$, spin-polarizing the NV^- ensemble, as shown in the energy level diagram in Fig. 3-1a. At zero magnetic field, the defect has a splitting $D \approx 2.87$ GHz between the

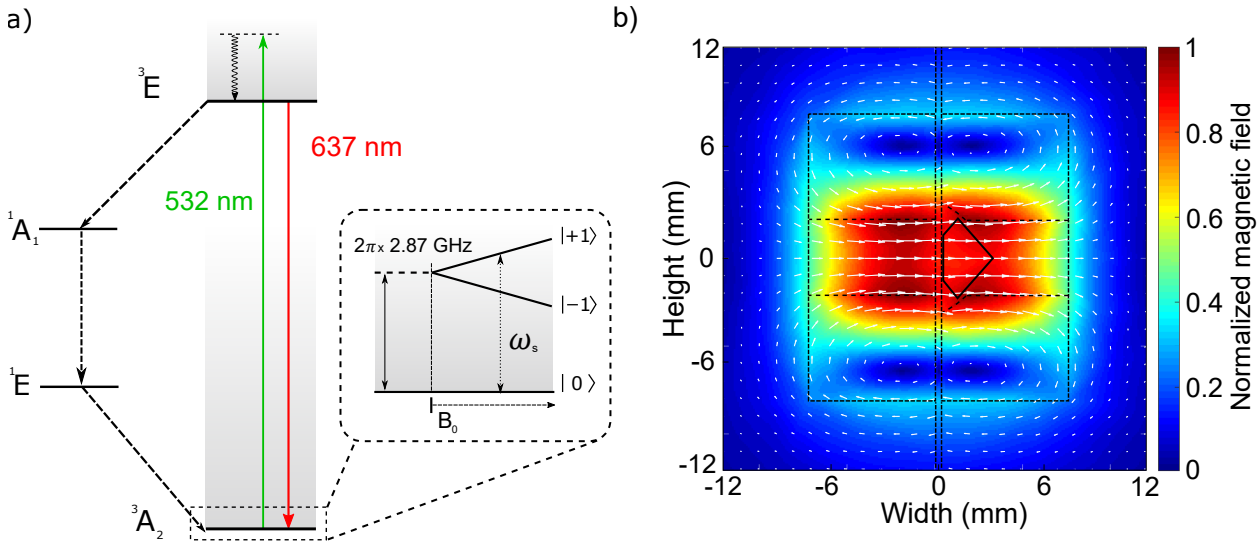

Figure 3-1: **Experimental setup for MW cavity readout of NV$^-$ centers in diamond.** (a) Level diagram. The NV$^-$ ground-state spin triplet (^{3}A$_2$) exhibits a 2.87 GHz zero-field splitting between the $|m_s = 0\rangle$ and degenerate $|m_s = \pm 1\rangle$ states. This degeneracy may be lifted by application of a bias magnetic field B_0, allowing individual addressing of either the $|m_s = 0\rangle \leftrightarrow |m_s = -1\rangle$ or $|m_s = 0\rangle \leftrightarrow |m_s = +1\rangle$ transitions. Optical pumping with 532 nm light initializes spins to the $|m_s = 0\rangle$ state via a non-radiative decay path (^{1}A$_1 \rightarrow {}^1$E). (b) Microwave cavity magnetic field. Interactions between the interrogation photons and the NV$^-$ ensemble can be enhanced by placing the diamond inside a cavity resonant with the applied photons. As illustrated in the axial cut of the composite cavity, the diamond (solid black) is placed near the antinode of the magnetic field (white arrows) created by the two dielectric resonators (black dashed).

$|m_s = 0\rangle$ state and the $|m_s = \pm 1\rangle$ states. Application of a tunable bias magnetic field $\vec{B}_0$ lifts the degeneracy of the $|m_s = \pm 1\rangle$ states, allowing either of the $|m_s = 0\rangle \leftrightarrow |m_s = \pm 1\rangle$ MW transitions to be individually addressed spectroscopically. The external bias field $\vec{B}_0$ is oriented along the diamond's $\langle 100 \rangle$ axis to project equally onto all four NV$^-$ orientations. The MWs are applied with drive frequency ω_d near-resonant with the $|m_s = 0\rangle \leftrightarrow |m_s = +1\rangle$ transition (with resonance frequency ω_s), and we restrict our discussion to the effective two-level system formed by these states.

The composite MW cavity consists of two concentric cylindrical dielectric resonators surrounding a high-NV$^-$-density diamond mounted on a mechanical support wafer. We define the bare cavity resonance frequency ω_c as the resonance frequency of the system in the absence of laser-induced spin polarization. Positioning the diamond at the MW magnetic field anti-node, as shown in Fig. 3-1b, maximizes the ensemble-photon coupling. An adjustable

input coupling loop couples the MW field into the composite cavity. A circulator allows for reflection measurements, while a supplementary output coupling loop allows for transmission measurements, as depicted in Fig. 3-2. The composite MW cavity exhibits an unloaded quality factor of $Q_0 = 22,000$.

We use a natural, brilliant-cut diamond with volume $V_{\text{dia}} = 25$ mm^3 which was subsequently HPHT-processed and irradiated following the Lucent process [161]. From electron paramagnetic resonance (EPR) measurements and comparison with a reference sample, the NV$^-$ density is estimated to be [NV$^-$] $= 5 \pm 2.5$ ppm, corresponding to a total NV$^-$ number $N_{\text{tot}} = 2 \pm 1 \times 10^{16}$. As a natural diamond, the sample displays substantial strain and exhibits an inhomogeneous dephasing time T_2^* of 40 ns. The P1 centers (as interrogated via EPR) exhibit a full-width-half-maximum linewidth of 910 kHz, of which approximately 300 kHz can be attributed to broadening from ^{13}C spins [14]. The residual 610 kHz linewidth suggests an approximate total nitrogen concentration [N$^{\text{T}}$]=18 ppm [17], while integration of the P1 EPR signal suggests [N_s^0] = 22 ppm. For simplicity we assume [N$^{\text{T}}$] = 20 ppm, which corresponds to an estimated NV$^-$ decoherence time $T_2 = 8$ μs. The value of [NV^0] is evaluated using the method of Alsid et al to be [NV^0] $= 1 \pm 0.5$ ppm [4].

The diamond is affixed to a semi-insulating wafer of silicon carbide (SiC) for mechanical support and located coaxially between two cylindrical dielectric resonators (relative dielectric $\epsilon_r \approx 34$, radius $a = 8.17$ mm, cylindrical length $L = 7.26$ mm, with a 4 mm diameter center-cut hole). The combined diamond-resonator composite cavity has a resonance frequency $\omega_c = 2\pi \times 2.901$ GHz and an unloaded quality factor $Q_0 \approx 22000$. The composite cavity is centered inside an aluminum shield (inner diameter = 50.8 mm, length = 89 mm) to reduce radiative losses. NV$^-$ centers within the diamond are continuously polarized into the $|m_s = 0\rangle$ Zeeman sublevel energy level by approximately 12 W of 532 nm optical excitation. A neodymium-iron-boron permanent magnet applies a 19.2 G static magnetic field $\vec{B}_{\text{perm}}$ along the diamond's $\langle 100 \rangle$ axis. An additional test coil applies a tunable magnetic field ($\vec{B}_{\text{coil}}$) along the same direction; the total bias field $\vec{B}_0$ can then be varied over the range 19.2 ± 25 G.

Fig. 3-2 depicts the main MW circuit components. Microwaves (produced by a Keysight E8257D PSG) at frequency ω_d are split into a signal and reference component, with the signal

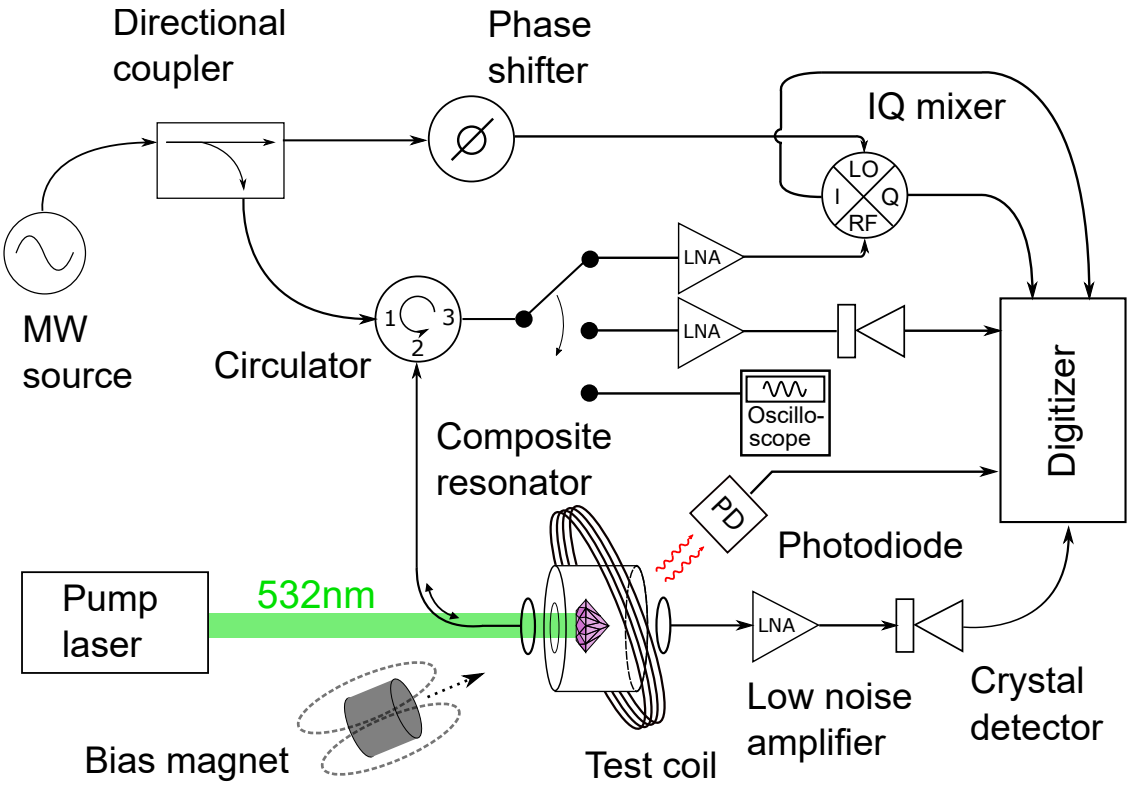

Figure 3-2: **Device schematic.** Applied MWs near-resonant with both the cavity and spin transitions are split into a signal component which interrogates the composite cavity through a circulator (lower branch) and a reference component (upper branch). Microwaves reflected from the composite cavity are amplified before being mixed with the reference component by an IQ mixer whose dual outputs are digitized. Alternatively, reflected MWs can be read out via a MW crystal detector or measured directly using an oscilloscope with sufficiently high sampling rate. Transmission measurements employ only an amplifier and a crystal detector. A photodiode monitoring red fluorescence allows simultaneous optical readout.

components passing through an attenuator and circulator before coupling into the composite cavity. The MWs are inductively coupled to the composite cavity by a wire loop (the input coupling loop) mounted on a translation stage. MWs reflected from the cavity can be measured in one of three ways: directly via the 50 Ω termination of an oscilloscope; through an amplifier followed by a crystal detector (which measures a correlate of the reflected power); or through an amplifier to the RF port of an IQ mixer, with the local oscillator (LO) port driven by the reference MW component. Transmission occurs through an additional wire loop (the output coupling loop) on a translation stage and is measured on a crystal detector.

3.2.2 Spin-cavity interaction

The interaction between a MW photon and a single spin is described by the Jaynes-Cummings Hamiltonian [38],

$$\mathcal{H} = \hbar\omega_c \hat{a}^\dagger \hat{a} + \frac{1}{2}\hbar\omega_s \hat{\sigma}_z + \hbar g_s \left(\hat{a}^\dagger \hat{\sigma}^- + \hat{a}\hat{\sigma}^+\right), \tag{3.1}$$

where $\hat{a}^\dagger$ and $\hat{a}$ are the creation and annihilation operators respectively (for photons at the bare cavity frequency ω_c); ω_s is the spin resonance frequency; and $\hat{\sigma}_z$, $\hat{\sigma}^+$, and $\hat{\sigma}^-$ are the Pauli-Z, raising, and lowering operators. The single-spin-photon coupling g_s at the cavity antinode is $g_s = \frac{\gamma}{2}\mathfrak{n}_\perp\sqrt{\frac{\hbar\omega_c\mu_0}{V_{\text{cav}}}}$ [7,137,180], where γ is the electron gyromagnetic ratio, μ_0 is the vacuum permeability, $\hbar$ is the reduced Plank constant, and V_{cav} is the mode volume of the microwave cavity resonance. The coefficient $\mathfrak{n}_\perp \leq 1$ is a geometrical factor, which is required because only the component of the cavity field transverse to the spin quantization axis can drive transitions (and the spin quantization axis may be set by a crystallographic axis, at an energy scale much greater than that of the coupling between the magnetic field and the spin). When the cavity and spin resonances are nearly degenerate, which is the regime employed in this work, the hybridized spin-cavity modes result in the familiar spectroscopic feature known as Rabi splitting.

For an ensemble of N polarized spins, the Jaynes-Cummings model is generalized to the Tavis-Cummings model [87, 155], with g_s replaced by the effective collective coupling $g_{\text{eff}} = g_s\sqrt{N}$ [42]. Predictions of this model are consistent with measurements of the MW response of solid-state spin ensembles strongly coupled to dielectric resonators at room temperature [27,28]. Since the MW cavity magnetic field varies by only a small amount ($\approx \pm 3.5\%$) over the diamond volume, we assume each spin has an identical coupling strength g_s.

In order to provide connection with the physical parameters of the experimental apparatus, it is convenient to develop a description of the system in terms of an equivalent circuit model (the full derivation of which is described in the Appendix B-E). The resulting RLC circuit model provides expressions for the reflection and transmission coefficients, which can then be formulated in terms of the quantum mechanical parameters of the system. With an ensemble undergoing constant optical-pumping-induced spin polarization at a rate

$\kappa_{\rm op} = 1/T_1^{\rm op}$, the voltage reflection coefficient is given by

$$\Gamma = -1 + \frac{\kappa_{c1}}{\frac{\kappa_c}{2} + j(\omega_d - \omega_c) + \frac{g_{\rm eff}^2}{\frac{\kappa_s}{2} + j(\omega_d - \omega_s) + \frac{g_s^2 n_{\rm cav} \cdot \kappa_s/(2\kappa_{\rm op})}{\frac{\kappa_s}{2} - j(\omega_d - \omega_s)}}}, \tag{3.2}$$

where the cavity loss rate $\kappa_c \equiv \kappa_{c0} + \kappa_{c1} + \kappa_{c2}$ is the sum of the unloaded, input port, and output port loss rates, respectively; $\kappa_s = 2/T_2$ is the homogeneous width of the spin resonance (with decoherence time T_2); and $n_{\rm cav}$ is the average number of cavity photons. In section B I derive the corresponding expression for the transmission coefficient. Here, to simplify the presentation, we have omitted in (3.2) integration over the inhomogeneous distribution of spin resonance frequencies; this distribution can be included following the methods of Refs. [49, 90]. We find that the inhomogeneous linewidth must be accounted for to produce optimal agreement in numerical models used to fit the experimental data. The reflection and transmission equations including integration over the inhomogeneous linewidth are discussed and depicted in Appendix E.

3.2.3 Readout mechanism

To understand the readout mechanism, we first consider only the dispersive effect of the NV$^-$ ensemble, neglecting the effect of absorption. (This simplification is valid for sufficiently high MW power, where the absorptive effect is suppressed relative to the dispersive effect). With $\omega_s = \omega_c$ (and neglecting absorption), reflection from the cavity remains unchanged regardless of the state of the NV$^-$ ensemble (e.g., regardless of whether optical spin-polarization light is applied). As ω_s shifts away from ω_c, however, the NV$^-$ ensemble produces a dispersive shift that modifies the composite cavity's resonance frequency, resulting in an increase in reflected MW power. Moreover, the dispersive effect produces a phase shift in the reflected voltage $\Gamma V_{\rm In}$ relative to the incident MWs (where Γ is the complex reflection coefficient and $V_{\rm In}$ is the incident MW voltage), and the sign of this phase shift depends on the sign of $\omega_s - \omega_c$. This allows the use of a phase-sensitive measurement technique by monitoring the quadrature port of an IQ mixer. Because the voltage on this port changes sign for deviations of ω_s above or below ω_c, with a zero-crossing for $\omega_s = \omega_c$, this measurement technique inherently

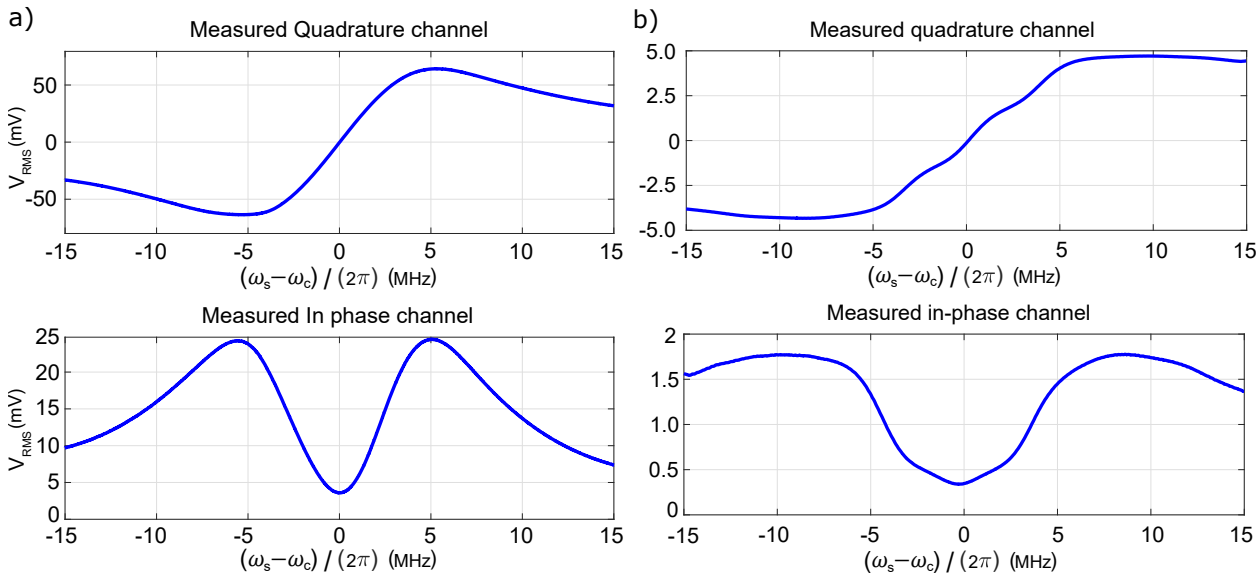

Figure 3-3: **Readout on an IQ mixer.** Measured in-phase and quadrature channels of an IQ mixer during MW cavity readout at 5 dBm of applied MW power. The MW drive ω_d is set to the bare cavity frequency ω_c, and, using the test coil, the spin-cavity detuning $(\omega_s - \omega_c)$ is swept from -15 MHz to 15 MHz. Finally, the phase of reference component (See Fig 3-2) is adjusted manually until the dispersive and absorptive signals are isolated to the quadrature and in-phase channels of the mixer, respectively. Data was taken under lower MW irradiation than in Figures 2-3 to avoid saturating the output of the low noise amplifier. The voltage signal here is measured after amplification and mixing with an effective gain (comprised of the amplifier gain 18 dB and mixer conversion loss 10.5 dB) of 7.5 dB. (a) Readout using a diamond with imhomogeneous linewidth 8 MHz. Hyperfine are not discernible due to high crystal strain. (b) Readout using a diamond with imhomogeneous linewidth 1 MHz. Hyperfine features are discernible, but partially obscured due to MW power broadening.

provides unity contrast.

3.2.4 Cavity-enhanced readout and comparison to ODMR

Readout as measured through the IQ mixer is depicted in Fig. 3-3. The signal corresponds to 5 dBm of incident MW power and the phase on the reference arm is set such that the dispersive effect of the cavity is isolated to the quadrature channel and the absorption effect is isolated to the in-phase channel. Depicted are the responses to two different diamonds subjected to the same experimental conditions. For example, Fig. 3-3b illustrates the response using a diamond that has discernible hyperfine features.

The readout method also provides a cavity-mediated narrowing of the magnetic resonance

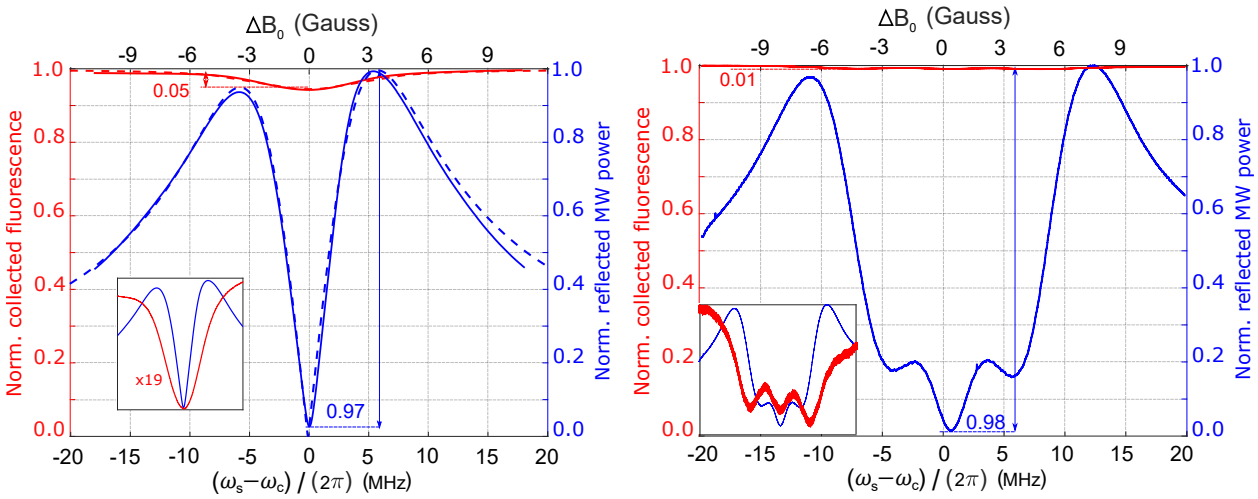

Figure 3-4: **Comparison of contrast and linewidth in MW cavity readout magnetic resonance and ODMR.** The signal associated with the NV$^-$ $|m_s = 0\rangle \leftrightarrow |m_s = +1\rangle$ magnetic resonance is recorded simultaneously using MW cavity readout (blue solid line) and conventional optical readout (red solid line). The MW cavity readout realizes contrasts $C = 0.97$ and $C = 0.98$, limited by imperfect circulator isolation, while conventional optical readout realizes contrast $C = 0.05$ and $C = 0.01$. For ease of comparison with the ODMR lineshape, MW cavity readout is performed here using a phase-insensitive measurement of reflected MW power, rather than the phase-sensitive technique. Fits from the inhomogeneously-broadened numberical model (blue dashed line) and a Lorentzian model of ODMR (red dashed line) are also shown. The inset shows both readout signals scaled to the same peak-to-peak values, highlighting the $\approx 2\times$ narrowing of the magnetic resonance feature observed with MW cavity readout. The left-right asymmetry in the MW cavity readout signal is attributed to a ≈ -20 kHz detuning of the applied microwaves from the bare cavity resonance. The applied MW power is 10 dBm.

feature. This narrowing is illustrated in Fig. 3-4, which shows the MW cavity readout magnetic resonance signals of two different diamonds plotted alongside simultaneously recorded conventional optically-detected magnetic resonance (ODMR) signals. The MW cavity readout feature of Fig. 3-4a exhibits a FWHM linewidth of 4 MHz, while the ODMR linewidth is 8.5 MHz (FWHM). To understand this narrowing, consider the resonance feature associated with reflection from the bare cavity (i.e., the composite cavity without laser light applied) vs. MW drive frequency ω_d. The cavity linewidth κ_c is independent of the spin resonance linewidth κ_s and, in principle, can be made narrower than the spin resonance by improving the cavity quality factor Q_0. The linewidth of the cavity-mediated magnetic resonance feature, however, is a function of both the cavity linewidth and the spin resonance

linewidth; roughly speaking, the former determines the dispersive shift needed to reflect 80% input power, while the latter partially determines the size of the dispersive shift for a given change in magnetic field. Moreover, the size of the dispersive shift for a given change in magnetic field is not determined solely by the spin resonance linewidth; the size of this shift increases with increased cooperativity. Thus, the cavity-mediated linewidth can be narrower than the spin resonance linewidth for sufficiently large values of g_{eff} and sufficiently small values of κ_c. The cavity-mediated narrowing is advantageous to magnetometer operation, as narrower magnetic resonance features can be localized with greater precision. The line narrowing effect is in agreement with expected behavior from the numerical model including inhomogeneous broadening, as shown in Fig. 3-4.

The data in Fig. 3-4 are collected employing the crystal detector to measure reflected MW power. The MW drive is set to the bare cavity resonance, $\omega_d = \omega_c$. The input coupling loop is critically coupled to the composite cavity, and the output coupling loop is removed, so that $\kappa_c = \kappa_{c0}/2$. The spin transition frequency ω_s is tuned across the cavity resonance ω_c by varying the value of $\vec{B}_{\text{coil}}$ as detailed above. An auxiliary photodiode allows simultaneous measurement of the NV^- fluorescence signal. In this measurement configuration, the contrast is slightly below unity due primarily to the imperfect isolation of the MW circulator. (For CW measurements, as performed here, we define the contrast $C = \frac{a-b}{a}$ where a and b denote the respective maxima and minina signal values when the bias field is swept over the magnetic resonance.)

3.3 Conclusion

The MW cavity readout method demonstrated here offers compelling advantages over alternative approaches for bulk solid-state quantum sensors. First, the method realizes unity contrast and circumvents the photon shot noise limitations inherent to conventional optical readout. In addition, unlike alternative optical readout techniques, MW cavity readout does not introduce deleterious overhead time in the measurement process. Although demonstrated here using NV^- centers in diamond, MW cavity readout can be performed on other solid-state crystals and paramagnetic spins, and is not exclusive to the small minority demonstrating

optical fluorescence with significant spin-state dependence. For example, di-vacancy [56] and silicon-vacancy centers [108] in silicon carbide can be optically spin polarized, but these defects display poor fluorescence contrast between spin states [30]; thus, cavity-enhanced MW readout could offer advantages for sensors based on these defects. As a demonstration, in the following chapter, I briefly present and discuss cavity-enhanced MW readout performed on chromium defects in sapphire (see section 4.6). Due to the high natural abundance of chromium defects, the larger zero field splitting, and the dielectric properties of the host crystal, no optical pumping is required to see a strong spin-cavity interaction. Finally, the cavity-enhanced MW readout technique promises favorable scaling; the measurement SNR increases linearly with the number (N) of defects interrogated, allowing for readout at the spin-projection limit for sufficiently large N.

Chapter 4

Magnetometry using cavity-enhanced microwave readout

Portions of this chapter have appeared in print in the following publications:

> "Cavity-enhanced microwave readout of a solid-state spin sensor," E. R. Eisenach, J. F. Barry, M. F. O'Keeffe, J. M. Schloss, M. H. Steinecker, D. R. Englund, and D. A. Braje. Nature Communications 12, Article number: 1357 (2021)
>
> "Thermally-Polarized Solid-State Spin Sensor" R. Wilcox, E. R. Eisenach, J. F. Barry, M. H. Steinecker, M. F. O'Keeffe, D. R. Englund, and D. A. Braje. Phys. Rev. Applied 17, 044004 (2022)

4.1 Introduction

In this Chapter, I demonstrate magnetometry using the cavity-enhanced microwave readout technique and an ensemble of NV^- centers in diamond–though the method has broad applicability to any paramagnetic defect with a microwave (MW) resonance (provided there is a means of inducing spin polarization). In addition to providing unity measurement contrast and circumventing the shot-noise limitation inherent to conventional optical spin readout, the readout method introduces no substantial overhead time to measurements and results in a cavity-mediated narrowing of the magnetic resonance features. This narrowing is par-

ticularly advantageous in magnetometry, as a narrower magnetic resonance feature can be localized in frequency with greater precision. Because the sensor's limiting noise source is independent of the number of polarized spin defects N, the device's sensitivity is expected to improve linearly with increasing N until the spin-projection limit is reached.

4.2 Results

4.2.1 Cooperativity and sensitivity

Neglecting absorption, the imaginary part of the reflection coefficient of eq. (3.2) can be approximately expressed in a more illuminating form within a particular regime relevant to magnetometry. For critical input coupling ($\kappa_{c1} = \kappa_{c0}$), no output coupling ($\kappa_{c2} = 0$), and $\omega_d = \omega_c$, the reflection coefficient in the limiting case of small spin-cavity detunings ($|\omega_s - \omega_c| \ll \kappa_s/2$) is approximately given by

$$\mathrm{Im}[\Gamma] \approx \frac{8g_{\mathrm{eff}}^2}{(\kappa_s^*)^2\kappa_c}\left(\omega_c - \omega_s\right), \tag{4.1}$$

where κ_s^* characterizes the inhomogeneous linewidth. This approximate expression is valid for n_{cav} high enough to saturate the homogeneous linewidth $n_{\mathrm{cav}} \gg \frac{\kappa_{op}\kappa_s}{2g_s^2}$ but below the number to produce substantial power broadening $n_{\mathrm{cav}} \lesssim \frac{\kappa_{op}\kappa_s^*}{2g_s^2}$. Equation 4.1 highlights the potential of this technique for high-sensitivity magnetometry, as $\mathrm{Im}[\Gamma]$ is proportional to spin-cavity detuning.

The prefactor $\frac{8g_s^2N}{(\kappa_s^*)^2\kappa_c}$ in (4.1) is closely related to the collective cooperativity, a dimensionless figure of merit for the ensemble-cavity coupling strength typically defined as $\xi = \frac{4g_{\mathrm{eff}}^2}{\kappa_s\kappa_c}$ [154]. To maximize spin readout fidelity, it is important to engineer the cooperativity of the ensemble-cavity system to be as large as possible.

4.2.2 Strong ensemble-cavity coupling at room temperature

The system's cooperativity is experimentally determined from the avoided crossing observed in recorded reflected and transmitted MW power, which are measured as the spin resonance

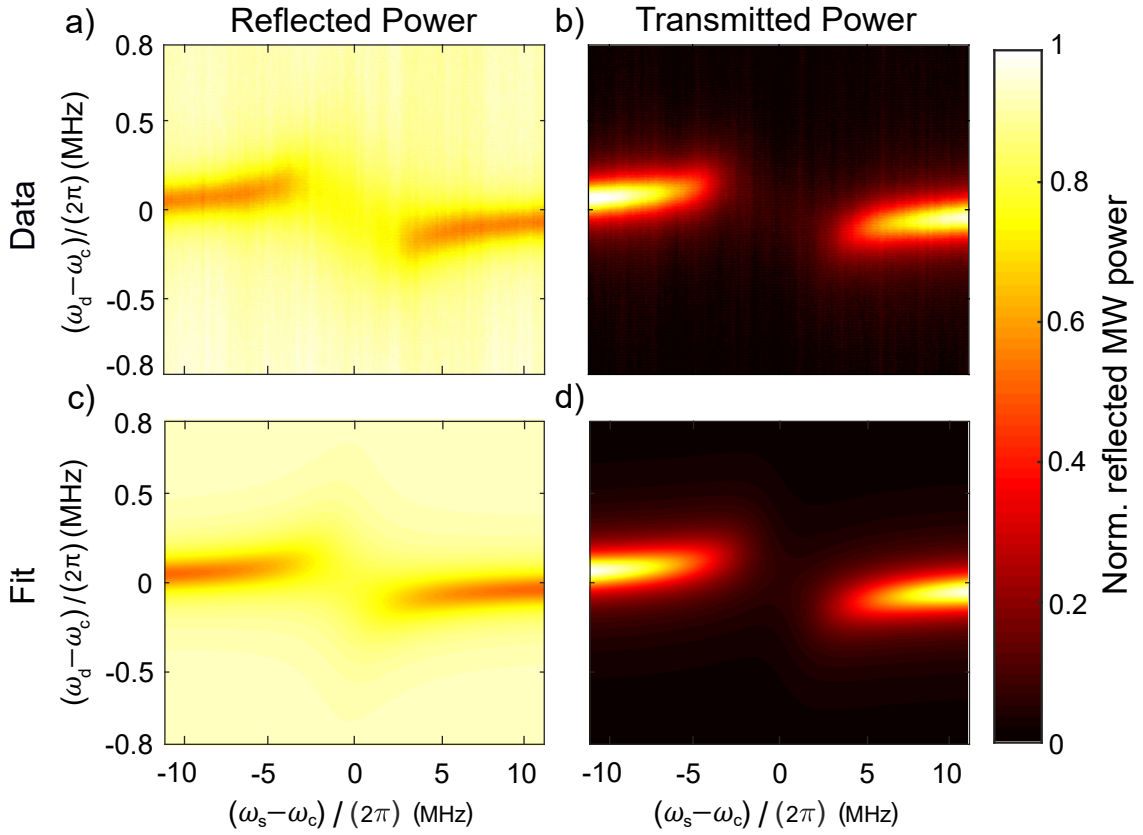

Figure 4-1: **Strong ensemble-cavity coupling under ambient conditions.** The spin resonance frequency is swept relative to the bare cavity resonance (horizontal axis) by varying the applied magnetic field; simultaneously varying the MW drive frequency (vertical axis) reveals the spin-ensemble-modified composite cavity resonance. Data are recorded both in reflection (a) and transmission (b). The data are fit (c - d) to (3.2) and (4.2) using a 2D nonlinear least-squares solver. The fit gives $g_{\text{eff}} = 2\pi \times 0.70$ MHz; see Methods for additional fit parameters. Each plot is normalized to unity, and recorded data is taken with -56 dBm of MW drive power.

frequency ω_s and MW drive frequency ω_d vary with respect to the bare cavity resonance ω_c. These measurements, shown in Fig. 4-1, are performed at low MW drive power to avoid perturbing the system. Reflection and transmission data in Fig. 4-1 are collected simultaneously. For both transmission and reflection measurements, the MWs are detected using a crystal detector operating in the linear regime. During this measurement, both the input and output coupling loops are undercoupled, resulting in a full-width-half-maximum (FWHM) loaded cavity linewidth of $\kappa_c = 2\pi \times 200$ kHz (given the measured loaded quality factor $Q_L = 14500$) . $\vec{B}_{\text{coil}}$ is increased from approximately -6.8 G to +6.8 G (altering ω_s)

in steps of 0.068 G while the MW drive $\omega_d/(2\pi)$ is varied relative to $\omega_c/(2\pi)$ over the range -800 kHz to +800 kHz. At each step of the bias field ($\vec{B}_{\text{coil}}$) sweep and at each MW drive frequency, the reflected and transmitted MWs are measured. The 2D power data are then fit to the square of the voltage reflection (eq. (3.2)) and the square of the voltage transmission, given by

$$T = \frac{\sqrt{\kappa_{c1}\kappa_{c2}}}{\frac{\kappa_c}{2} + j(\omega_d - \omega_c) + \frac{g_{\text{eff}}^2}{\frac{\kappa_s}{2} + j(\omega_d - \omega_s) + \frac{g_s^2 n_{\text{cav}} \cdot \kappa_s/(2\kappa_{\text{op}})}{\frac{\kappa_s}{2} - j(\omega_d - \omega_s)}}}. \tag{4.2}$$

The reflection and transmission coefficients are consistent with those derived from a quantum mechanical treatment of the electromagnetic field [64, 75, 153] using input-output theory [62, 164]. The final fit parameters are $g_{\text{eff}} = 2\pi \times 0.70$ MHz, $\kappa_{c0} = 2\pi \times 125$ kHz, $\kappa_{c1} = 2\pi \times 25.3$ kHz, $\kappa_{c2} = 2\pi \times 33.4$ kHz, and $\kappa_s = 2\pi \times 5.24$ MHz. Here, the fit κ_s should be interpreted as an effective linewidth including inhomogeneous broadening. Because the spin resonance linewidth arises from both homogeneous (e.g., dipolar interactions) and inhomogeneous (e.g., strain) mechanisms, with differing effects on the behavior of the system, the appropriate value of κ_s for calculating the cooperativity is not obvious. We model the cooperativity, including inhomogeneous broadening, using the method of Ref. [176]. This analysis produces a value $\xi = 1.8$ under the experimental conditions used for measurement (i.e., $\kappa_c = 2\pi \times 200$ kHz) or $\xi = 2.8$ assuming negligible losses to input and output coupling (i.e., $\kappa_c = \kappa_{c0}$).

4.2.3 Optimizing applied microwave power

While useful for characterizing spin-cavity coupling strength, operation at low applied MW power is undesirable for high-fidelity spin readout due to the fixed contribution of Johnson noise. Applying higher MW power minimizes the fractional contribution of Johnson noise, but higher applied power will also produce deleterious broadening of the spin ensemble resonance; the optimum power is set by a balance between these two considerations. To optimize MW cavity readout for magnetometry, we investigate the spin-cavity system behavior at higher MW powers by plotting the reflection signal as a function of $\omega_s - \omega_c$ for a range of MW amplitudes (Fig. 4-2). For incident MW powers above -20 dBm the fractional absorption is suppressed, resulting in little reflected power on resonance. We use the slope

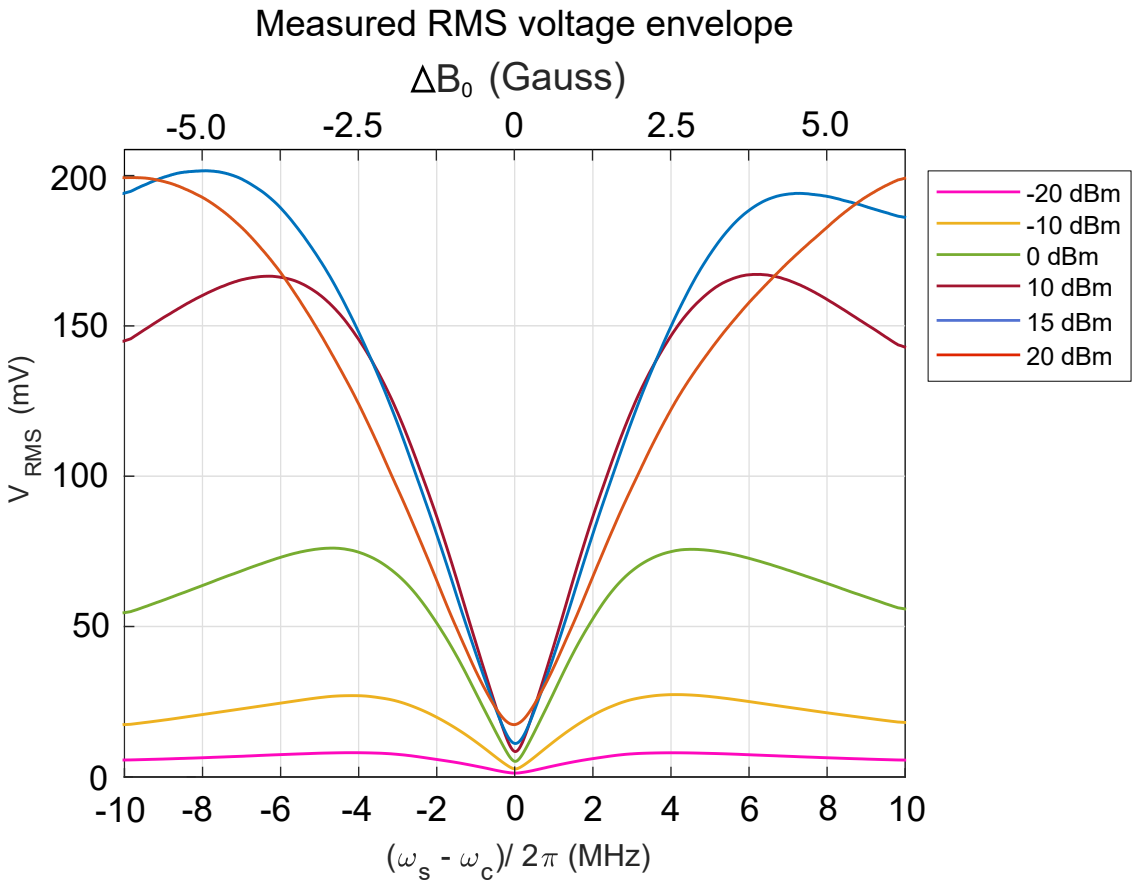

Figure 4-2: **Optimizing MW cavity readout for magnetometry.** The 2.901 GHz reflection signal is terminated into the 50 Ω input of a 40 GS/s oscilloscope. The reflected RMS voltage into 50 Ω is plotted vs the spin-cavity detuning for various MW powers. Above approximately 10 dBm, MW-induced broadening of the NV$^-$ ground state transition reduces the achievable magnetic sensitivity of the sensor; consequently 10 dBm is the near-optimal applied MW power.

$\partial V_{\mathrm{RMS}}/\partial(\omega_s - \omega_c)$ as a figure of merit to determine the optimal applied MW power for best signal-to-noise ratio, which, for the selected diamond, occurs at 10 dBm. As shown in Fig. 4-2, an increase in the applied MW power above 10 dBm yields a reduced slope due to excessive MW power broadening of the spin resonance. We therefore empirically determine that approximately 10 dBm is optimal for the present system, resulting in a maximum reflected power of -2.4 dBm. The high peak reflected MW power (3.0×10^{20} MW photons/second) for the NV$^-$ ensemble of $\approx 1.4 \times 10^{15}$ polarized spins, combined with unity contrast, ensures that MW photon shot noise does not limit the achievable readout fidelity.

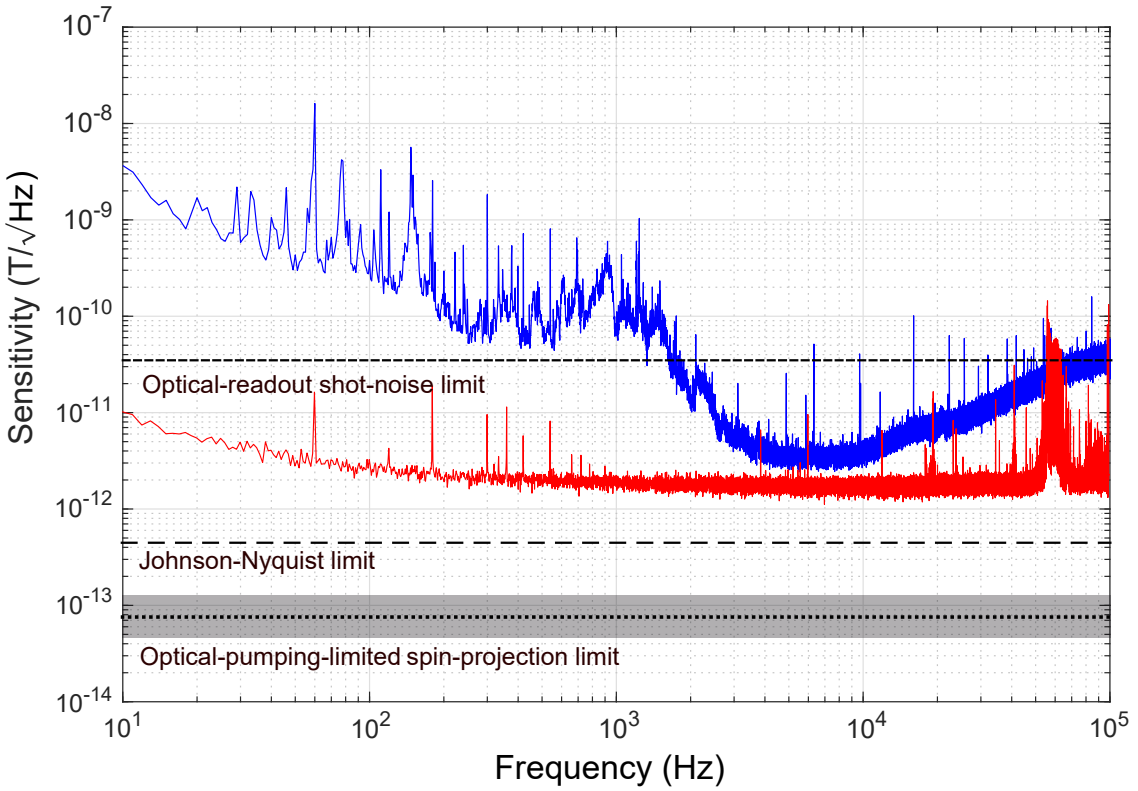

Figure 4-3: **MW cavity readout magnetometer sensitivity.** Based on noise spectral density measured during magnetometer operation (blue solid line), we project a sensitivity of ≈ 3 pT/$\sqrt{\text{Hz}}$ in the band from 5 kHz to 10 kHz, where sensitivity approaches the limit set by the measured noise floor of the amplifier and digitizer electronics (red solid line). Also depicted are the optical-readout shot-noise limit (black short dashed line) of the experimental setup, the calculated Johnson-Nyquist noise limit (black long dashed line) of 0.5 pT/$\sqrt{\text{Hz}}$ and the optical-pumping-limited spin-projection limit (black dotted line). The optical-pumping-limited spin-projection limit is bounded above and below (gray shaded box) to illustrate uncertainty arising from estimating the optical pumping relaxation time T_1^{op}. Magnetometry is performed using the phase-sensitive technique of recording reflected MW voltage through the IQ mixer; IQ traces are shown in section 3.2.4.

4.2.4 Device magnetic sensitivity

For magnetometry, MWs reflected from the composite cavity are amplified, band-pass filtered, and mixed with an attenuated and phase-shifted reference component. The reflected signal is mixed to base band using an IQ mixer. The phase of the reference component, which drives the mixer local oscillator (LO) port, is adjusted until the absorptive ($\propto \text{Re}[\Gamma]V_{\text{In}}$) and dispersive ($\propto \text{Im}[\Gamma]V_{\text{In}}$) components are isolated to the in-phase (I) and quadrature (Q) channels respectively.

The magnetometry sensisitivity is then characterized by monitoring the Q channel as a 1 μT (RMS) field is applied via the test coil. The test field is calibrated using the known dependence of the ODMR resonances on applied field. The RMS amplitude of the test field is checked with a commercial magnetometer and also via calculation from the known coil geometry and applied current. The magnetometer sensitivity is given by

$$\eta = \frac{e_n}{V_{\mathrm{Dig}}/B_{\mathrm{test}}^{\mathrm{RMS}}}, \tag{4.3}$$

where e_n is the RMS voltage noise floor (at the digitizer) of the double-sided spectrum (20 $\mathrm{nV}/\sqrt{\mathrm{Hz}}$, which occurs between 5 and 10 kHz), $B_{\mathrm{test}}^{\mathrm{RMS}}$ is a 1 μT RMS amplitude magnetic field at 10 Hz frequency, and V_{Dig} is the RMS voltage recorded at the digitizer in response to the test magnetic field.

Although applying higher MW power decreases fractional Johnson noise, it also broadens the dispersive resonance feature [1]. Hence, there exists an optimal power P to achieve a maximum absolute value of the slope $\left|d\left(\mathrm{Im}[\Gamma]V_{\mathrm{RMS}}\right)/d\omega_s\right|$ (where V_{RMS} is the RMS incident MW voltage) and thus maximal sensitivity to changes in ω_s. For the present system, we empirically determine that $P = 10$ dBm is optimal (see section 4.2.3), which results in a maximum reflected power of -2.4 dBm.

In the high-MW-drive-power (i.e., primarily dispersive) regime, the maximal slope is achieved in the Q channel when $\omega_s = \omega_c = \omega_d$. By using only the permanent magnet to set $\omega_s = \omega_c$, we ensure that the test coil current source does not contribute to the noise floor of the magnetometer.

The magnetometer is calibrated with a 10 Hz test magnetic field with a 1 μT root-mean-square (RMS) amplitude. The measured noise spectrum is scaled using this known magnetic field value to produce a noise spectrum in magnetic field units, and we project a minimum sensitivity of 3.2 $\mathrm{pT}/\sqrt{\mathrm{Hz}}$ from approximately 5 to 10 kHz (see Fig. 4-3). For a 1 nT test field measured over 1 second, this projected minimum sensitivity corresponds to a signal-to-noise ratio (SNR) of ≈310, compared to a photon-shot-noise-limited SNR of ≈40 for optical readout in this apparatus. In the following chapter, DC signals are upmodulated to this low-noise band by application of an AC magnetic bias field.

4.3 Microwave photon noise limit to readout fidelity

It is instructive to calculate the expected inverse readout fidelity $\sigma_R = 1/\mathcal{F}$ in the absence of thermal (Johnson-Nyquist) and other technical noise (e.g. phase noise). The inverse readout fidelity (equal to the factor over spin projection noise) is

$$\sigma_R = \sqrt{1 + \frac{1}{C^2 n_{\text{avg}}}}, \tag{4.4}$$

where C is the readout contrast (fringe visibility) and n_{avg} represents the average number of MW photons collected per NV$^-$ per measurement. At 10 dBm of applied MW power, the composite cavity reflects a maximum -2.4 dBm, which corresponds to 3.0×10^{20} MW photons/second. We assume $N = 1.4 \times 10^{15}$, $T_1^{\text{op}} = 130$ μs, and $C = 1$. This crude estimate gives $n_{\text{avg}} = 28$, resulting in $\sigma_R = 1.017$ and $\mathcal{F} = .983$. Employing instead $T_2 = 8$ μs results in $\sigma_R = 1.254$ and $\mathcal{F} = .798$. Employing $T_2^* = 40$ ns yields $\sigma_R = 10.7$ and $\mathcal{F} = 0.093$. For any of these timescales, the shot-noise-limited sensitivity $\eta_{\text{sh}} = \sigma_R \eta_{\text{sp}}^{\text{op}}$ is substantially less than the Johnson-Nyquist-limited sensitivity, so that the readout is not limited by MW photon shot noise.

4.4 Johnson-noise sensitivity limit

Johnson-Nyquist (thermal) noise degrades the microwave signal following interaction with the composite cavity. The composite cavity produces Johnson-Nyquist noise $V_{\text{JN}} = \sqrt{4 k_B T R_s \Delta f}$, where k_B is the Boltzmann constant, T is the cavity's temperature, R_s is the equivalent resistance of the composite cavity, and Δf is the single-sided measurement bandwidth. Assuming that the cavity is impedance matched to the termination resistance $R = 50\ \Omega$, this produces a noise voltage $\sqrt{k_B T R \Delta f}$ at the measurement device. The Johnson-Nyquist-limited sensitivity is then given by

$$\eta_{\text{JN}} = \frac{\sqrt{k_B T R}}{F_1 \cdot F_2 \cdot \left[\frac{d(\text{Im}[\Gamma] V_{\text{RMS}})}{dB_0}\right]_{\text{max}}}, \tag{4.5}$$

where $\text{Im}[\Gamma] V_{\text{RMS}}$ is the quadrature component of the reflected RMS MW voltage, B_0 is the magnetic field, and F_1 and F_2 are factors of order unity depending on details of the signal

and the processing architecture respectively. For scenarios where the phase of the signal is assumed to be known (as in this work), $F_1 = \sqrt{2}$. For architectures where all signal is isolated into the quadrature channel of the mixer (as in this work), we expect $F_2 = \sqrt{2}$. At 10 dBm of applied MW power, we then estimate $\frac{d(\mathrm{Im}[\Gamma]V_{\mathrm{RMS}})}{dB_0} \approx 0.05$ V/G (Fig. 4-2), yielding $\eta_{\mathrm{JN}} \approx 0.5$ pT/$\sqrt{\mathrm{Hz}}$.

4.5 Spin-projection sensitivity limit

The spin-projection-limited magnetic sensitivity is given by [29]

$$\eta_{\mathrm{sp}} \approx \frac{\hbar}{g_e \mu_B} \frac{1}{\sqrt{N\tau}}, \tag{4.6}$$

where τ is the free precession time. For a Ramsey measurement scheme, it is nearly optimal to choose a precession time equal to the dephasing time, T_2^* [14]. Although there is no explicit precession time in a CW measurement scheme, we make the substitution $\tau = T_2^*$ in the above equation as a crude estimate of the effective precession time. For our measurement scheme, two additional factors must be considered, each of which degrades the spin-projection-noise-limited sensitivity. First, the projection of the magnetic field on each NV^- orientation is $B_0/\sqrt{3}$, so that the magnetic sensitivity is a factor $\sqrt{3}$ larger than naïvely expected. Second, the finite time required (on average) to optically initialize a spin, T_1^{op}, produces an effective duty cycle for the measurement of τ/T_1^{op} (assuming $T_1^{\mathrm{op}} \gg \tau$). Again making the substitution $\tau = T_2^*$, this effects a degredation of the sensitivity by the factor $\sqrt{T_1^{\mathrm{op}}/T_2^*}$. With these modifications, the appropriate spin-projection-limited sensitivity for this measurement scheme (in the absence of all technical noise) is approximately given by

$$\eta_{\mathrm{sp}}^{\mathrm{op}} \approx \sqrt{3} \frac{\hbar}{g_e \mu_B} \frac{1}{\sqrt{NT_2^*}} \sqrt{\frac{T_1^{\mathrm{op}}}{T_2^*}}. \tag{4.7}$$

To compute T_1^{op}, we assume that M green photons are required, on average, to polarize one NV^- center. We expect $M > 1$ due to the limited asymmetry of decay to $|m_s = 0\rangle$ through the intersystem crossing and because green photons may be "wasted" through radiative decay

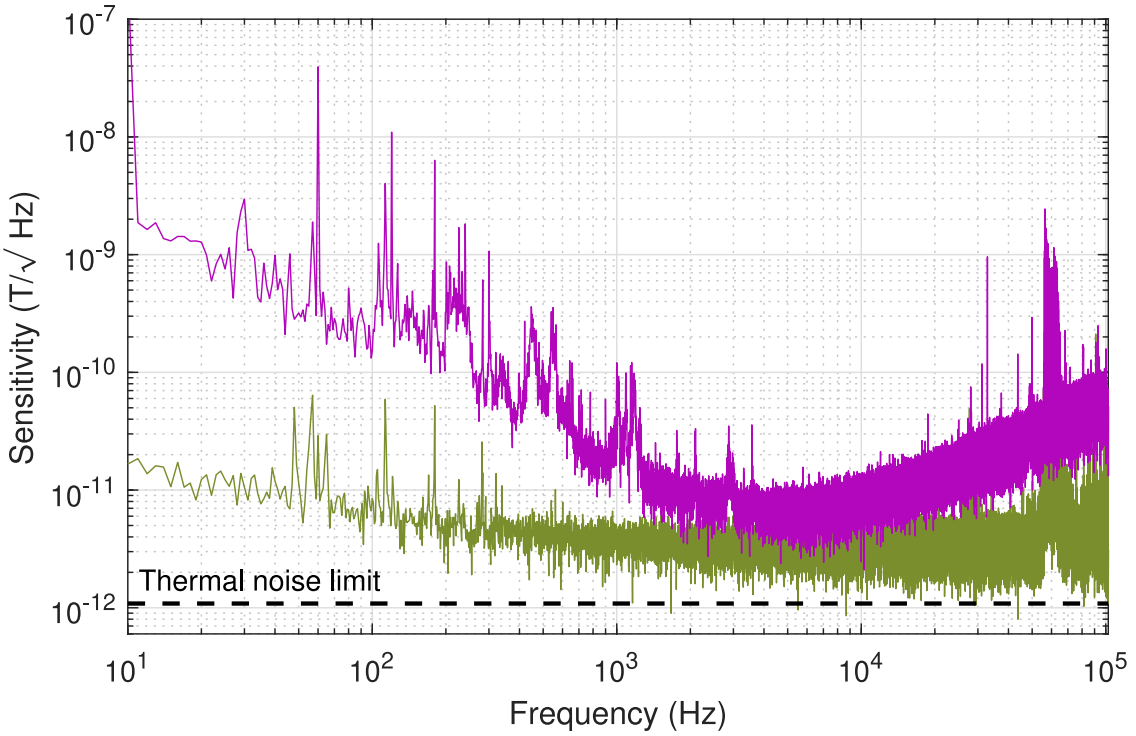

Figure 4-4: **Broadband magnetometry using Cr^{3+} ions in sapphire.** The noise spectral density measured during magnetometer operation (—) yields a projected sensitivity of ≈10 pT$\sqrt{\text{Hz}}$ in the low-noise band between 4 kHz and 6 kHz. The projected sensitivity approaches the noise floor set by amplifier, mixer, and readout electronics (—). The thermal-noise-limited sensitivity (- -) of 1.1 pT/$\sqrt{\text{Hz}}$ is also depicted.

or absorption by substitutional nitrogen, NV^0, and other defects. We crudely guess the value of M is between between 1 and 10. We calculate T_1^{op} as

$$T_1^{\text{op}} = M\frac{N}{R_{\text{pho}}} \tag{4.8}$$

where R_{pho} is the number of photons per second applied to the NV ensemble. For $M = 3$, assuming 12 W of 532 nm light and $N = 1.4 \times 10^{15}$ polarized NV^- centers, we have $T_1^{\text{op}} =$ 130 µs and $\eta_{\text{sp}}^{\text{op}} = 75$ fT/$\sqrt{\text{Hz}}$.

4.6 Thermally-polarized magnetometry

Although the cavity-enhanced MW readout technique is inherently non-optical, in the above described experiments using NV centers in diamond, a laser is still required to spin-polarize a

sizeable ensemble. Unfortunately, the light source is often the primary driver of complexity and power consumption in a sensor. However, considerable efforts are being made today for device simplification and miniaturization [31, 85, 93, 150]. Although laser initialization provides a strongly polarized ensemble (ex. $\sim 80\%$ for NVs), with enough defects concentrated at the cavity anti-node, strong coupling can be achieved passively via thermal spin polarization ($\sim 0.05\%$ in some ensembles). The requirements are two fold: first, a zero field splitting (ZFS) must exist by which a net population difference between two states can occur in thermal equilibrium; and second, a sufficient number of defects must couple to the cavity to overcome the low net-spin polarization. Such requirements are met, for example, by chromium ions (Cr^{+}) in sapphire (also known as ruby). In this section I briefly describe cavity-enhanced readout measurements of a ruby crystal, using an experimental setup which has been configured for high-sensitivity magnetometry [169].

Cr^{3+} ions in ruby have spin $S = \frac{3}{2}$ and exhibit a $2\pi \times 11.5$ GHz ZFS between the $|m_s = +\frac{3}{2}\rangle$ and $|m_s = +\frac{1}{2}\rangle$ states. At 293 K, the net population difference between these two states is 0.047%, corresponding to a polarized spin density of $\sim 7 \times 10^{15}$ cm^{-3}. The ruby crystal serves as its own high-quality factor dielectric resonator, which increases the volume of the spin ensemble that couples to the electromagnetic mode of the cavity.

Employing a similar experimental setup and MW signal chain described in section 3.2.1 and 4.2.4, the ruby-based magnetometer achieves an optimal sensitivity of $\eta = 9.7$ pT$/\sqrt{\text{Hz}}$ at 5 kHz (See Fig. 4-4). This measurement shows the applicability of the cavity-enhanced MW readout technique to defect centers other than the NV center in diamond. Furthermore, the ruby-based device is the first entirely non-optical solid-state spin sensor. By removing the need for optical spin polarization, solid-state spin sensors can be made smaller, lighter, and more power efficient. The challenges of light delivery, including heat loads and laser noise are also avoided entirely.

4.7 Conclusion

The projected sensitivity of the present NV-based magnetometer is among the highest reported broadband sensitivities of devices employing NV ensembles. For example, the best NV-ensemble-based broadband magnetometers employing conventional optical readout have achieved sensitivities ranging from 0.9 pT/$\sqrt{\text{Hz}}$ [58] to 15 pT/$\sqrt{\text{Hz}}$ [15]. The projected sensitivity using MW cavity readout is limited by phase noise of the interrogation microwaves, Johnson-Nyquist (thermal) noise, and vibration-induced changes in the coupling to the composite cavity. Phase noise manifests as frequency fluctuations, which cause variations in reflected power unrelated to the magnetic field value. Selection of a lower-phase-noise MW source would reduce these fluctuations. Vibration-induced fluctuations could be reduced by engineering a more robust cavity coupling mechanism. Together, these changes could allow the Johnson-Nyquist-noise limit of 0.5 pT/$\sqrt{\text{Hz}}$ (see Fig. 4-3) to be reached. Crucially, unlike shot noise, these limiting noise sources remain fixed as the signal strength increases. Therefore, there exists a straightforward path to improving sensitivity toward the spin-projection limit: augmenting the signal through increasing the collective cooperativity ξ. Cooperativity can be improved by increasing the number of polarized spins, increasing the cavity quality factor, or reducing the spin-resonance linewidth [16]. Furthermore, pulsed measurement protocols could be employed to avoid sensitivity degradation due to MW power broadening.

Chapter 5

Vector magnetometry using cavity-enhanced microwave readout

Portions of this chapter will appear in print in the following publication:

> "Vector magnetometry using cavity-enhanced microwave readout of a solid-state spin sensor," E. R. Eisenach, J. M. Schloss, L. M. Pham, D. R. Englund, and D. A. Braje. *In Preparation.*

5.1 Introduction

Solid-state quantum sensors are attracting wide interest as magnetometers, because their fixed crystallographic axes allow for complete vector field sensing, free from systematic drifts and heading errors [41, 97, 103, 115]. The negatively charged nitrogen-vacancy (NV^-) defect center in diamond is a particularly promising platform as it combines the capability for long term stability, high dynamic range, and low power operation into a single compact sensor package [85, 151]. The NV^- center's excellent coherence properties at room temperature also allow high sensitivity operation [11, 12, 17], however poor readout has kept the platform from performing even close to the standard quantum limit [14]. In response, many alternative readout methods have been proposed and demonstrated [26, 71, 77, 81, 112, 142, 146, 149], including the recently discovered technique of cavity-enhanced microwave (MW) readout. Although the previous demonstration of cavity readout projected sensitivities in the single

picotesla regime, the experimental implementation was held back by 1/f noise at low frequencies. Furthermore, the demonstration was constrained to sensing only along a single vector axis, with measurement ambiguities if the fields were not perfectly aligned with the sensing axis. In this chapter, we expand on the cavity readout technique, and demonstrate high sensitivity measurements of three dimensional dynamic vector fields. We enable vector functionality via application of an AC magnetic bias field. By judicious choice of the AC field frequency and direction, the projection of a dynamic field along each NV axis (Fig 5-1a) can be separately read out in the low-noise band of the readout electronics. The AC bias field also allows us to introduce a measurement scheme which suppresses drift related errors by up to two orders of magnitude, suggesting the capability for long term stable operation. Our magnetometer demonstrates an average broadband sensitivity of 160 pT/$\sqrt{\text{Hz}}$ per axis limited by magnetic noise of the AC magnetic bias field. With minor improvements to the bias field coil geometry and excitation circuitry, we project that the magnetometer can achieve an average broadband sensitivity of 35 pT/$\sqrt{\text{Hz}}$. With further improvements to the NV^- density and spin coherence properties of the diamond sample, we expect the magnetometer to achieve sub-picotesla magnetic sensitivities.

5.2 Magnetometry method

Similar to previous demonstrations of vector magnetometry using NV^- centers in diamond, we apply a magnetic bias field along the crystallographic orientation which equally separates the spin transition frequencies of different NV axes (Fig. 5-1b) [39,136]. In this work however, we oscillate the bias magnetic field at a frequency ω_{AC} which serves two primary purposes: one, as the NV^-s are read out via the interaction between the spin resonance frequency and a single MW cavity mode, the AC field sweeps the resonance frequency of each NV orientation sequentially passed the cavity resonance (at ω_c); and two, the modulation of the spin resonances due to the AC field encodes the spin information at ω_{AC} and its harmonics ($\omega_{\text{AC}}+n\omega_{\text{AC}},\ n = 1, 2, 3, ...$), effectively up-converting signals of interest away from base-band 1/f noise, and into the low-phase-noise region of the readout electronics.

For the current experimental implementation (discussed in more detail below), sweeping

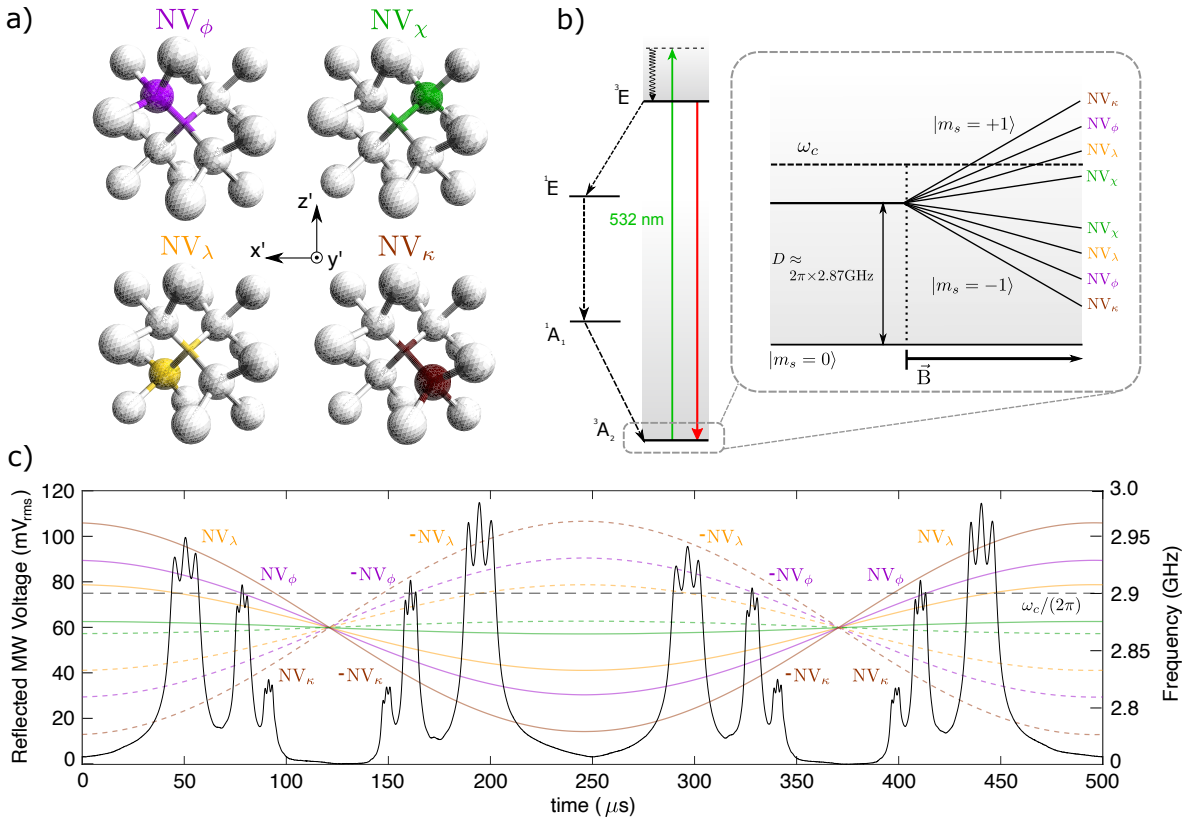

Figure 5-1: **The NV center in diamond and cavity readout spectrum** (a) The NV$^-$ exists in equal number along four different crystallographic orientations in the diamond lattice. When employed as a magnetometer, each of the four orientations NV$_\lambda$, NV$_\phi$, NV$_\kappa$, NV$_\chi$ measures the component of the magnetic field projected along its symmetry axis. (b) The NV$^-$ ground-state triplet (^{3}A$_2$) exhibits a $D \approx 2\pi\times 2.87$ GHz zero-field splitting between the $|m_s=0\rangle$ and degenerate $|m_s=\pm1\rangle$ spin states. In the presence of a magnetic field $\vec{B}(t)$ the $|m_s=\pm1\rangle$ sublevels experience a Zeeman splitting proportional to the projection of the magnetic field along the NV symmetry axis. Above-band optical excitation (typically performed with a 532 nm laser) initializes the NV$^-$ spins into the $|m_s=0\rangle$ spin state via a non-radiative decay path (^{1}A$_1 \longrightarrow {}^1$E). (c) Cavity-enhanced microwave readout absorption spectrum under the application of an AC magnetic bias field with frequency $\omega_{\rm AC} = 2\pi \times 2$ kHz. The magnetic bias field projects onto the four NV orientations causing the Zeeman shifts shown in (b). As NV orientations NV$_\lambda$, NV$_\phi$, and NV$_\kappa$ cross ω_c, MWs reflect from the cavity (which are subsequently measured) creating the depicted readout spectrum in (c). For each half-cycle of the magnetic field, both the $|m_s=+1\rangle$ spin state (solid-lines) and the $|m_s=-1\rangle$ spin state (dashed lines) cross ω_c. Differences in the amount of reflected MW voltage between NV orientations arise from differences in the vacuum coupling g_s of each NV axis with the lineraly polarized MW field. Asymmetries between $|m_s=\pm1\rangle$ spin states in each half-cycle of the spectrum are due to asymmetries in the cavity resonance profile.

all four NV spin resonances across ω_c requires a field amplitude in excess of 250 G. At such strong fields, gradients across the diamond are large enough to induce substantial broadening of the measured resonances. We therefore restrict ourselves to three NV orientations (NV_λ, NV_ϕ, and NV_κ) oriented along linearly independent vector axes which are sufficient to reconstruct the three dimensional vector field. Figure 5-1c shows the cavity readout absorption spectrum as the spin resonances sequentially interact with the cavity. In the proximity of each cross-over point between a spin resonance and ω_c, MWs are reflected off of the cavity resulting in a cavity-enhanced spin-resonance profile. A perturbing field $\vec{B}_{\text{sens}}$ causes the spin resonance to shift in frequency, which changes the time ($\tau_{\pm i=\lambda,\phi,\kappa}$, where the sign refers to each respective $|m_s = \pm 1\rangle$ spin state) at which the spin resonance crosses ω_c. We can then relate changes in the cross-over times to $\vec{B}_{\text{sens}}$ by measuring shifts in the peaks of the cavity-enhanced spin-resonance spectrum. We then apply a calibrated linear transformation matrix to the measured peak-shifts and construct the Cartesian magnetic field components in the laboratory frame of reference.

Finally, because the AC field changes sign over the course of a full oscillation period, the method interrogates both the $|m_s = \pm 1\rangle$ spin states of each NV orientation. In analogy to conventional NV magnetometry methods [40], we make use of both spin states to subtract out temperature-dependent resonance shifts of the spins and the MW cavity. For each half cycle of the AC bias field depicted in Fig. 5-1c, the peaks move common mode with changes in $\vec{B}_{\text{sens}}$, and differential mode for changes in the NV zero field splitting due to temperature (-74 kHz/K [14]), changes in the cavity frequency ω_c ($\approx +3$ kHz/K), and changes in the AC bias field amplitude. By summing the half-cycle responses of both $|m_s = \pm 1\rangle$ peaks, we reduce errors due to drifts in temperature by almost two orders of magnitude (See Appendix G.2).

5.3 Experimental setup

For mechanical stability and heat sinking, we cleave a brilliant-cut diamond with a $\{100\}$ table facet and $\langle 100\rangle$ edges at an angle $\theta = 32^\circ$ and $\phi = 22.2^\circ$ (Fig. 5-2a). The total diamond volume after cleaving is $V_{\text{dia}} \approx 6$ mm^3, and, from electron paramagnetic resonance (EPR) measurements, the $\left[\text{NV}^-\right]$ density is estimated as 3 ppm, corresponding to a total

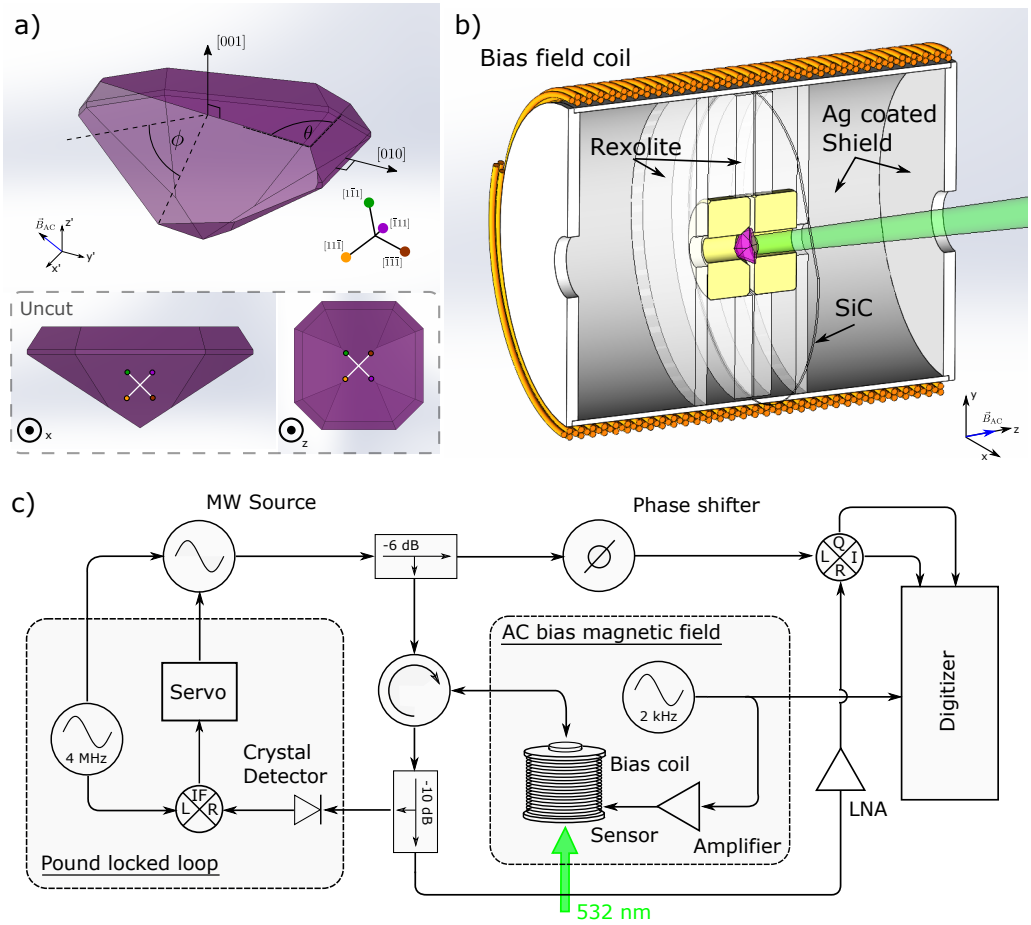

Figure 5-2: **Experimental setup and MW signal chain** (a) For better mechanical stabilization and heat sinking, a high NV^- density cushion-cut diamond is cleaved along the depicted angles ($\phi = 22.2°$ and $\theta = 32°$), such that the normal vector to the newly created plane is $\vec{u}_B = (-0.53, 0.23, 0.82)$ in the diamond coordinate system (where z' is oriented normal to the table facet). A bias magnetic field applied along $\vec{u}_B$ equally splits the NV energy levels as depicted in fig. 5-1b. Also depicted are the NV symmetry axes as oriented in the diamond, defined in terms of the diamond lattice vectors. (b) The newly cleaved face of the diamond is affixed to a semi-insulating wafer of silicon carbide (SiC) and enclosed between two concentric dielectric resonators which form the composite MW cavity. The composite cavity is centered inside an alumina ceramic shield with interior surfaces coated in 10 μm of silver to reduce radiative MW losses, and held in place using Rexolite spacers (some additional Rexolite structural components are omitted for clarity). A bias field coil produces the AC magnetic bias field $\vec{B}_{\mathrm{AC}}$ oriented along $\vec{u}_B$ in the diamond reference frame. (c) Microwave device schematic. A 4 MHz modulated MW tone, resonant with the composite cavity, is split into a signal component (lower branch) which interrogates the cavity through a circulator and a reference component (upper branch). Microwaves reflected from the cavity are then amplified before being mixed with the reference component by an IQ mixer. A small amount of reflected MW power (-10 dB) is split off and directed to a Pound-locked-loop which locks the MW carrier tone to the cavity resonance.

NV number $NV^- = 4.8 \times 10^{15}$. The sample exhibits an inhomogeneous dephasing time T_2^* of 300 ns, corresponding to a natural full-width half-max (FWHM) linewidth of ≈ 1 MHz. The cleaved face of the diamond is glued to a 50.8 mm diameter, 300 μm thick semi-insulating wafer of silicon-carbide (SiC) for mechanical stabilization and heat sinking. To correct for a 3° miscut of the diamond, we insert a fused silica shim between the diamond and SiC wafer. The diamond is then enclosed in between two cylindrical dielectric resonators ($Q_0 \approx 27,000$ and relative dielectric $\epsilon_r \approx 34$) each with a 4 mm diameter center cut hole (Fig. 5-2b). The separation between the two resonators is adjusted, so that the combined diamond-resonator composite cavity resonates at $\omega_c = 2\pi \times 2.9$ GHz. We choose ω_c with the following considerations in mind: a composite cavity resonance too close to D results in frequency-adjacent spin resonances passing ω_c in too close a succession, causing their resonance profiles to obscure one another; a higher composite cavity resonance, on the other hand, requires a stronger AC magnetic bias field magnitude to interrogate the NV axes.

The composite cavity is then placed at the center of an alumina ceramic shield with a 50.8 mm inner diameter. The shield is wrapped in 151 turns of 20 gauge magnet wire and the resulting bias coil is made to resonate with a Q of 6 at the frequency $\omega_{\mathrm{AC}} = 2\pi \times 2$ kHz (See Appendix F.1 for information on the bias field resonant circuit; and Appendix F.2 for information on the choice of ω_{AC}). By resonantly driving the bias field coil we increase the circuit efficiency by the Q-factor, and reject low frequency noise which could otherwise couple to the sensor. In the resonant configuration ≈ 1.5 A_{rms} of current produces the necessary bias magnetic field amplitude to sweep three-of-four NV orientations across ω_c. The inner surfaces of the shield are coated in ≈ 10 μm of silver to reduce radiative losses of the MW composite cavity. At 10 μm, the silver coating is thick enough to fully shield MW signals from the cavity (where the skin depth at 3 GHz is ≈ 1.2 μm), yet thin enough to not attenuate the AC magnetic bias field. The maximum bias field amplitude is $B_{\mathrm{max}} \approx 53$ G and is measured at 2 kHz using a calibrated pick-up loop and a commercial magnetometer. We measure the magnetic bias field unit vector direction $\vec{u}_B = [-0.53,\ 0.231,\ 0.82]$, and the diamond strain parameters $\vec{M}_z = \left[M_z^{\chi},\ M_z^{\kappa},\ M_z^{\phi},\ M_z^{\lambda}\right] = [140,\ -160,\ -171,\ -154]$ kHz at DC using optically detected magnetic resonance (ODMR). Finally, the diamond is illuminated with 3 W of 532 nm laser light, which continuously polarizes the NV^- centers into the $|m_s = 0\rangle$

sublevel.

The MW signal chain and main MW circuit components are depicted in fig. 5-2c. Microwaves at frequency ω_d are split into a signal arm (lower branch) which interrogates the cavity through a circulator, and a reference arm (upper branch) which, after passing through a variable phase shifter, terminates in the local oscillator (LO) port of an IQ mixer. As the cavity slope decreases farther from the composite cavity resonance, detunings between the MW drive tone and the cavity resonance (i.e. steady state conditions in which $\omega_d \neq \omega_c$) result in worse sensitivities. To maintain high sensitivity, we therefore lock the MW drive tone to the composite-cavity resonance such that $\omega_d = \omega_c$. To accomplish this, we split off a small amount of the MW power reflected from the cavity (≈ -10 dB) as feedback for a Pound-locked-loop, and adjust the locked-loop gain and PI corner to provide a 1 Hz bandwidth which compensates for slow cavity resonance drifts due to temperature. Because changes in the cavity resonance due to coupling to the spin ensemble occur at $\sim \omega_{\mathrm{AC}}/(2\pi) \gg 1$ Hz, they are unaffected by the lock. We determine that approximately -10 dBm of delivered MW power is optimal for the present system, by adjusting the incident MW power while monitoring the reflected signal voltage.

For the vector demonstration discussed below, we place the composite cavity sensor at the center of a 3-axis commercial Helmholtz coil. To reduce distortion of the AC magnetic bias field due to the non-magnetic optical table and breadboard, the composite cavity sensor is mounted on a 7.5 cm high ceramic pedestal, which is suspended 30 cm above the optical table on an 80/20 T-slot aluminum beam. Two flanking aluminum breadboards, separated from the composite cavity sensor by 10 cm, hold beam-steering mirrors to allow the laser light to impinge on the diamond. Finite element magnetostatic simulations (FEMM) of the experimental setup show distortions of the AC magnetic bias field due to the flanking breadboards, and the aluminum beam to be 1% or better. The magnetic fields applied by the Helmholtz coils are calibrated using a commercial magnetometer, and compared to fields calculated using the factory provided calibration numbers. For our measurement of the device sensitivity, the composite cavity sensor is removed from the Helmholtz coil, and placed in a 5-layer Mu-metal magnetic shield to ensure that stray magnetic signals in the laboratory do not affect the measured sensitivity.

5.4 Vector magnetometry demonstration

The responses of the NV spin-resonances to a sensing field $\vec{B}_{\text{sens}}(t)$ are linearized using a technique analogous to the one discussed in [136]. The magnetic signals are encoded in time, and we can construct a matrix $\mathbf{A}$ which provides a linear map of the components of $\vec{B}_{\text{sens}}$ onto changes in the peaks of the spin-resonance features,

$$\begin{bmatrix} \Delta\tau_\lambda \\ \Delta\tau_\phi \\ \Delta\tau_\kappa \end{bmatrix}_{\text{sens}} = \mathbf{A} \begin{bmatrix} B_x \\ B_y \\ B_z \end{bmatrix}_{\text{sens}}, \tag{5.1}$$

where $\Delta\tau_{i=\lambda,\kappa,\phi,\chi} = (\Delta\tau_{+i} + \Delta\tau_{-i})/2$ represents a shift in the measured NV$^-$-axis center hyperfine peaks in the cavity-enhanced spin-resonance spectrum (Appendix G.1). After determining $\mathbf{A}$, the matrix inverse $\mathbf{A}^{-1}$ transforms measured shifts $\Delta\tau_i$ into the magnetic field $\vec{B}_{\text{sens}}$ in the laboratory frame of reference.

To demonstrate full reconstruction of a measured magnetic field vector, each axis of the Helmholtz coil simultaneously applies a time-varying sinusoidal test field to the composite sensor. The test field frequency content, and the calibrated x, y, z vector component amplitudes, are listed in table 5.1 (the fields applied along each Cartesian axis are separated in frequency only to make clear the extent to which they can be reconstructed in the laboratory frame of reference). Figure 5-3a shows the voltage spectral density of one second of data acquisition. The NV$^-$ cavity readout spectrum is encoded at ω_{AC} and harmonics up to $\approx 2\pi \times 0.75$ MHz; the test fields are encoded at the sum and difference frequencies $\omega_{\text{AC}} \pm \omega_{j=x,y,z}$. The spectrum is high-pass filtered at 1900 Hz and low-pass filtered using a Savitzgy-Golay (S-G) filter of order 2 and frame length of 19 samples, corresponding to a 3dB cutoff frequency of ≈ 0.75 MHz. After filtering, the NV$^-$ hyperfine features of each full-cycle of the AC magnetic bias field are peak fit using polynomial interpolation. Because each full-cycle of the AC magnetic bias field samples the magnetic field twice ($Fs = \omega_{AC}/\pi$), the working bandwidth of the device is Nyquist limited to the bias field frequency.

Time traces of the peaks after summation of the $|m_s = \pm 1\rangle$ features (summation of the cross-over times for both spin states reduces the effects of temperature drifts in the

$\vec{B}_{\text{sens}}$	$\omega_{j=x,y,z}$	$\lvert B_{j=x,y,z}\rvert$ calibrated (μT)	$\lvert B_{j=x,y,z}\rvert$ measured (μT)	% deviation
$B_x(t)$	$2\pi \times 24$ Hz	5.13	5.11	0.39
$B_y(t)$	$2\pi \times 10$ Hz	5.92	5.89	0.51
$B_z(t)$	$2\pi \times 43$ Hz	4.97	4.94	0.60

Table 5.1: Applied and measured magnetic test field information.

diamond and cavity; see Appendix G.2) and corresponding amplitude spectral densities are depicted in fig. 5-3b-d. After digital low-pass filtering with a 3dB cutoff at 210 Hz, band-pass filtering at 60 Hz and 120 Hz, and high-pass filtering at 1 Hz, we apply the inverse $\mathbf{A}^{-1}$ of the transformation matrix to the time traces, and extract the laboratory-frame magnetic vector field components $B_x(t)$, $B_y(t)$, $B_z(t)$ (Fig. 5-3e-g). The single-sided equivalent noise bandwidth (f_{ENBW}) after filtering is ≈ 208 Hz. The resulting RMS test field amplitudes and their deviation from calibrated values are listed in table 5.1. We find agreement within 0.6% or better between the calibrated values and those extracted using the cavity readout vector magnetometer. This discrepancy falls within an expected range given the factory calibrated 0.4% uniformity of the Helmholtz coil field, and the 8 cm^3 uncertainty in the placement of the commercial magnetometer's sensing element. Finally, we determine the sensor dynamic range by applying a monotonically increasing static magnetic field (first in x, then y, then z) until the adjacent resonances of different NV orientations obscure one another, or until the AC bias field can no longer sweep either $|m_s = \pm 1\rangle$ spin state across the cavity resonance. We find the dynamic range in x to be 1 mT, 1.1 mT in y, and 1.6 mT in z.

5.5 Device sensitivity

We evaluate the sensitivity of the device by moving the sensor into a magnetically shielded environment, and taking magnetometry measurements in the absence of applied fields. We take one second of data, extract the time traces of $\Delta\tau_i(t)$, and transform them into the laboratory frame by applying $\mathbf{A}^{-1}$. The power spectral density (PSD) of each Cartesian direction (Fig. 5-4a-c) integrated over the sensing bandwidth, yields measurement variances

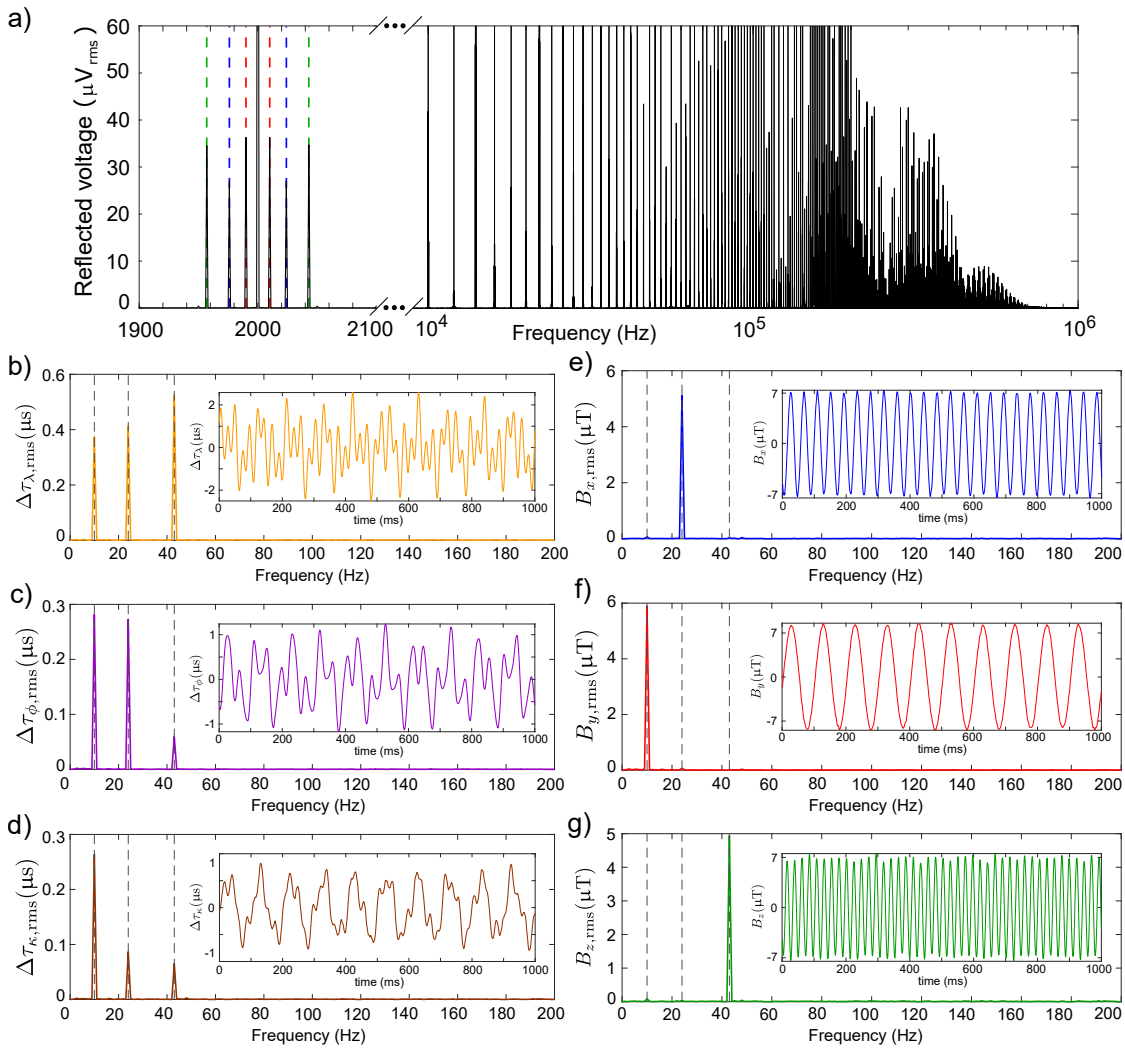

Figure 5-3: **Vector magnetometry demonstration** (a) A three-axis Helmholtz coil simultaneously applies test fields $B_x(t) = 5.13\ \mu$T, $B_y(t) = 5.92\ \mu$T, and $B_z(t) = 4.97\ \mu$T at the frequencies $\omega_x/(2\pi) = 24$ Hz (- -), $\omega_y/(2\pi) = 10$ Hz (- -), and $\omega_z/(2\pi) = 43$ Hz (- -), respectively. Under the application of an AC magnetic bias field at frequency $\omega_{\rm AC}/(2\pi) = 2$ kHz, the test fields are upmodulated, away from base-band 1/f noise, to the sum and difference frequencies $\omega_{\rm AC} \pm \omega_{j=x,y,z}$. The full cavity readout spectrum is encoded in the harmonics of $\omega_{\rm AC}$ up to ≈ 750 kHz. (b) - (d) Amplitude spectral densities of the magnetic field dependent peaks $\Delta\tau_{i,\rm rms}$ (where $i = \lambda, \phi, \kappa$ represents the respective NV axis) of 1 second of collected data. The insets depict the time series data $\Delta\tau_i(t)$ for each respective peak, after filtering. (e) - (f) Amplitude spectral densities of the measured fields in the laboratory frame of reference, extracted from $\Delta\tau_i$ after the application of the inverse linear transformation matrix $\mathbf{A}^{-1}$. Insets depict the time series data for each axis $B_x(t)$, $B_y(t)$, and $B_z(t)$. Residual cross talk between axes is present, but we calculate its effect to be on the order of 1% or better.

$\sigma^2_{B_x}$, $\sigma^2_{B_y}$, $\sigma^2_{B_z}$. We then compute the sensitivity per axis as [136],

$$\eta_j = \sqrt{\frac{\sigma^2_{B_j}}{2f_{\mathrm{ENBW}}}}. \tag{5.2}$$

The evaluated sensitivities are $\eta_x = 161\mathrm{pT}/\sqrt{\mathrm{Hz}}$, $\eta_y = 119\mathrm{pT}/\sqrt{\mathrm{Hz}}$, and $\eta_z = 192\mathrm{pT}/\sqrt{\mathrm{Hz}}$ which are limited by magnetic noise on the AC bias field. We determine magnetic noise as our limitation in two ways: One, using a dynamic signal analyzer we measure the voltage noise spectral density of the source and amplifier during operation, use the measured value to compute the bandwidth normalized magnetic noise density using the known coil impedance and geometry, and finally compare the result to the vector norm of our sensitivities. Two, keeping all other parameters fixed, we ensure the sensitivity of each axis scales linearly with the amplifier gain by taking measurements at different gain settings.

We also estimate the sensitivity in the absence of magnetic noise by measuring the slopes $\left[dV_{i,\mathrm{rms}}/dt\right]_{\max}$ of the resonances in fig. 5-1c. The sensitivity of each NV orientation can then be calculated as

$$\eta_i^{\mathrm{slope}} \approx \frac{e_n}{\left[dV_{i,\mathrm{rms}}/dt\right]_{\max}} \cdot \left[\frac{dB_i(t)}{dt}\right]_{t=\tau_i}, \tag{5.3}$$

where $e_n = 35\ \mathrm{nV}/\sqrt{\mathrm{Hz}}$ is the RMS noise floor of the double-sided spectrum at 2 kHz, and $\left[dB_i(t)/dt\right]_{t=\tau_i}$ is the slope of the bias field projected along the NV axis $i = \lambda, \phi, \kappa$ at the cross-over time τ_i. Using equation (5.3), we compute $\eta_\lambda^{\mathrm{slope}} = 17\mathrm{pT}/\sqrt{\mathrm{Hz}}$, $\eta_\phi^{\mathrm{slope}} = 27\mathrm{pT}/\sqrt{\mathrm{Hz}}$, and $\eta_\kappa^{\mathrm{slope}} = 62\mathrm{pT}/\sqrt{\mathrm{Hz}}$.

5.6 Discussion

The sensor exhibits different sensitivities along each axis due to NV-orientation-dependent couplings $g_{s,i}$ to the MW field (See Appendix H). Because only the component of the MW field projected onto a plane perpendicular to the NV axis drives the transition $|m_s = 0\rangle \longrightarrow |m_s = \pm 1\rangle$, the axis most aligned with the MW magnetic field, and coincidentally the AC magnetic bias field, exhibits the weakest coupling. The differences in $g_{s,i}$ are readily observed in the absorption spectrum of fig. 5-1c, where the amount of reflected MW voltage depends

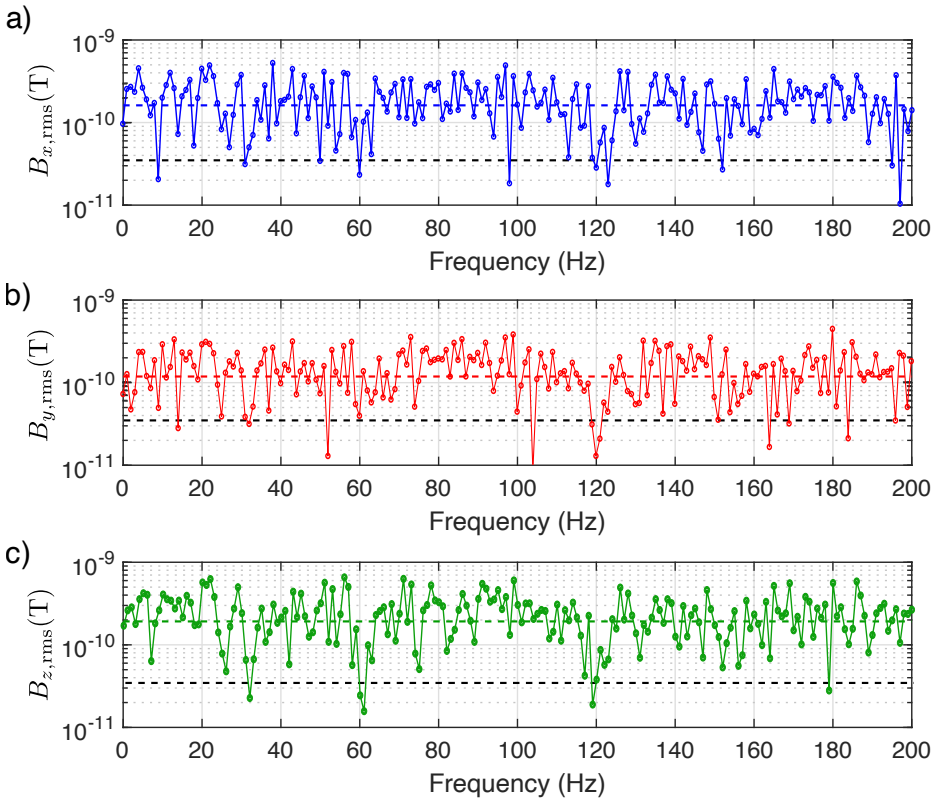

Figure 5-4: **Vector sensitivities** (a) - (c) Power spectral densities of each Cartesian axis in the absence of applied magnetic fields and after filtering. Colored dashed lines (– –,– –,– –) indicate the bandwidth normalized sensitivity (in $\mathrm{pT}/\sqrt{\mathrm{Hz}}$) as computed by equation (5.2). Black dashed lines (– –) indicate the average estimated broadband sensitivity per NV axis in the absence of magnetic bias field noise.

on which NV-axis is being interrogated by the cavity. The effect on the sensitivity is at most of order unity, and can be mitigated by rotating the cavity such that the MW field projects equally onto all four axes.

While the sensor is limited by noise on the AC magnetic bias field, there exist simple strategies to enable the full sensitivity of the device. Shrinking the bias field coil either by reducing the shield diameter, or by placing the coil inside the shield would reduce the current, and consequently the voltage, necessary to produce the AC bias field at the diamond. Simulations using finite element electromagnetics (FEMM) software suggest that reducing the coil and shield diameter by 50%, while maintaining the same number of turns, or placing the reduced coil within the confines of the shield, would reduce the necessary current to ≈ 0.38 A_{rms}. As a result, a low power amplifier with improved voltage noise could be employed, which would drive the magnetic noise down more than an order of magnitude. Shrinking the coil even further is possible, but would have to be met with changes to the cavity design as simulations in ANSYS HFSS show an inverse relationship between the coil diameter and cavity resonance frequency. To compensate for an increase in the resonance frequency, the resonator height could be increased [82], or additional dielectric material could be added to the cavity with minimal effect on g_s.

Beyond improving the performance of the AC bias field, the device sensitivity can be enhanced by more than an order of magnitude by increasing the number of polarized spins per NV axis N_i, and reducing the spin resonance linewidth κ_s^*. Simulations using the numerical model described in [55] suggest that a diamond of the same size with an NV density of 5ppm and a 500 ns T_2^* can achieve sub-picotesla sensitivities at the same input laser power. Finally, while the analysis found in [169] suggests that improving the Q above $\sim 30,000$ in our device would yield little increase in the sensitivity, an improvement in the spin-photon coupling g_s could be achieved via mode engineering techniques [35], or by introducing a circularly polarized MW mode.

5.7 Conclusion

This chapter demonstrates three-dimensional dynamic vector magnetometry using the recently developed cavity-enhanced microwave readout technique (see chapter 3). The magnetometer architecture relies on an AC magnetic bias field which modulates DC signals of interest into the low-noise band of the interrogation electronics. By choosing the direction of the AC field appropriately, the magnetic field projection along three-of-four diamond tetrahedral axes is measured and reconstructed in the laboratory frame. Because the AC field allows measurement of both $|m_s = \pm 1\rangle$ spin states, we introduce a unique measurement scheme which reduces systematic errors due to temperature drifts by up to two orders of magnitude. Locking of the MW drive tone to the composite cavity further serves to mitigate drifts in the sensitivity. The magnetometer achieves an average broadband sensitivity of 160 $\mathrm{pT}/\sqrt{\mathrm{Hz}}$ per Cartesian axis, limited by technical noise of the experimental device, but is expected to reach sensitivities of better than 17 $\mathrm{pT}/\sqrt{\mathrm{Hz}}$ per NV axis. While the device presented here is operated in CW mode, pulsed measurement protocols could be employed to reduce the effects of microwave power broadening on the spin ensemble.

Chapter 6

Summary and outlook

This thesis discussed two approaches to improving the readout fidelity of solid-state spin-ensembles. First, the loop gap resonator is presented as a means for applying strong and ultra-homogeneous MWs to large diamond sample sizes. For sample volumes of 3 mm^3 or less, the resonator provides field strengths of 4.8 G with an RMS uniformity of $\sigma_{\mathrm{rms}} = 0.8\%$, a drastic improvement over commonly employed planar-only geometries [7,83,95]. For bulk sensing, the sensitivity is often improved by increasing the total number of addressed NV centers, by either using samples with higher NV-densities or larger detection volumes. However, as the NV ensemble coherence time depends inversely on NV density [17], there exists an upper bound on the NV density after which larger sample sizes are utilized to further improve the sensitivity. For example, by increasing the interrogated volume by almost an order of magnitude, one can improve the sensitivity of a hypothetical NV-based magnetometer by more than a factor of 3. As discussed in section 2.5, increasing the sample size must be met with a larger volume of strong and homogeneous MWs to mitigate any deleterious effects on the readout fidelity. For the loop gap resonator, increasing the volume by an order of magnitude from 1 mm^3 incurs only a 3% reduction in the overall magnetic field homogeneity across the entire sample volume. Finally, the loop gap resonator has an open geometry, which allows for nearly half of the 4π solid angle to remain optically accessible. In a single compact design therefore, the loop gap resonator both improves on the MW magnetic field homogeneity, and allows the use of ever larger sample volumes. With these combined capabilities, we expect the device to be useful for bulk sensing [2, 15, 31, 40, 171]

and particularly imaging applications [15, 61, 66, 67, 84, 96, 173].

As optical fluorescence readout is intrinsically limited to low readout fidelities for devices based on ensembles of NV centers [14], this thesis discusses a novel readout method which provides high-fidelity, room temperature readout via strong collective coupling to a dielectric MW cavity. The cavity-enhanced readout technique is applicable to a host of solid-state crystals and paramagnetic defects, but is largely demonstrated using an ensemble of NV centers in diamond (cavity-enhanced microwave readout of chromium defects in sapphire is also briefly discussed). The technique is then applied to magnetometry and we project one of the highest reported broadband sensitivities of a device employing NV ensembles. In the current configuration, the sensitivity is limited by phase noise on the driving MW signal, and thermal noise of the readout electronics. Unlike shot noise however, these remain fixed as the signal strength increases, unlocking a straight forward path to improving the sensitivity toward the spin-projection limit: by increasing the spin-photon collective cooperativity parameter. Room-temperature magnetometry with sensitivity approaching the spin-projection limit would enable an increase in the utility of solid-state quantum sensors, for example in magnetoencephalography [25] and magnetocardiography [110] devices. In addition to magnetometry, we expect that this technique will find broad application in precision tests of fundamental physics [59], precision frequency generation [27], and electric field sensing [32, 51].

Finally, this thesis demonstrates the ability of the high-sensitivity cavity-enhanced MW readout technique to be used in applications that require measurements of the total magnetic vector field. The capability of vector magnetometry is achieved using an AC magnetic bias field to sequentially interrogate spin resonances of different NV orientations. Because the AC field sweeps both the $|m_s = \pm 1\rangle$ spin states across the cavity resonance, we introduce a measurement scheme which suppresses errors in the magnetometer output due to temperature fluctuations by almost two orders of magnitude. Finally, by modulating the NV resonances, the AC bias field upconverts fields of interest into the low-noise band of the readout electronics, enabling high measurement sensitivity. While our implementation is limited by technical noise, the method promises highly competitive sensitivities with the potential for magnetometry at the spin projection limit [53, 55]. Furthermore, it remains broadly applicable to a

number of other solid-state defects [169], and thus promises the development of new quantum sensors that do not rely on the optical properties of the sensor species. We envision future applications in magnetoencephalography [25, 68, 133], magnetocardiography [110], magnetic anomaly detection [140, 182], and space weather monitoring [145].

Appendix A

The nitrogen vacancy center in diamond

The negatively-charged NV color center (NV^-) is a deep band gap impurity within the diamond crystal lattice (Fig. A-1a). The point defect's C_{3v} symmetry results in a $^3A_2$ spin-triplet ground state and a ^3E spin-triplet excited state, separated by a zero phonon line (ZPL) of 637 nm [105]. Spin-spin interactions give rise to a zero-field splitting in the ground-state spin triplet, shifting the $m_s = \pm 1$ states with respect to the $m_s = 0$ state by $D_{gs} \approx 2.87$ GHz (Fig. A-1b). In the presence of a static magnetic field B_0, the $m_s = \pm 1$ sublevels experience Zeeman splitting proportional to the projection of the magnetic field along the NV symmetry axis. Above-band optical excitation (typically performed with a 532-nm laser) results in phononic relaxation of the NV spin within the ^3E excited state, followed by fluorescent emission in a broad band. While these optical transitions are generally spin-preserving, an alternate decay path through a pair of metastable singlet states ($^1A_1$ and ^1E) results in preferential relaxation from the $m_s = \pm 1$ excited states to the $m_s = 0$ ground state that is non-radiative in the typical $637 - 800$ nm fluorescence band. This behavior under optical excitation has two major consequences: (1) an optical means of polarizing the NV spin, and (2) optical detection via spin-state-dependent fluorescence intensity.

Measurement of the NV electron spin resonance spectrum can be performed by sweeping the carrier frequency of the MW drive field and monitoring NV fluorescence in the visible band. Generally, the continuous optical excitation pumps the NV spin population into the more fluorescent $m_s = 0$ state; however, when the carrier frequency is resonant with an NV spin transition, the NV spin population is cycled into an $m_s = \pm 1$ state, caus-

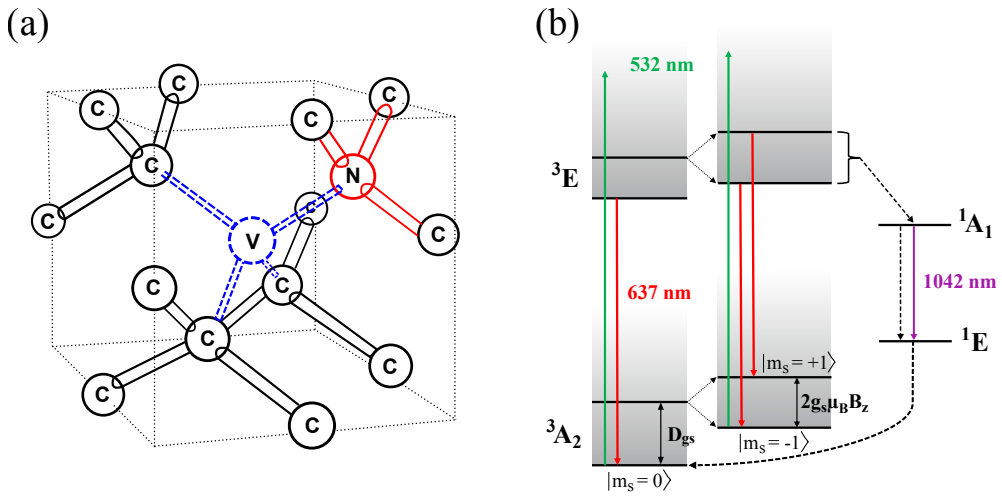

Figure A-1: **The NV center structure.** (a) Example of one NV center orientation within the diamond crystal structure. (b) The NV electronic energy level structure.

ing decreased fluorescence intensity, which appears as a dip in the electron spin resonance spectrum [79, 131]. Since the NV symmetry axis may be aligned along one of four possible crystal-defined orientations—each orientation being equally thermodynamically likely in low strain diamond—the electron spin resonance spectrum can contain up to eight distinct non-degenerate NV resonances, which probe different field components. The different orientations act as basis vectors, which collectively span three dimensional space, and allow the total vector field to be reconstructed [39, 79, 136].

Appendix B

Electromagnetic theory of dielectric resonators

In this section, I analyze the the electromagnetic fields of a dielectric cavity in order to extract the equivalent lumped element circuit components necessary to build a more convenient RLC model. Initially, I consider the case where only the input loop couples to the resonator (Fig. B-1a). From there I derive multiple equivalent circuit models, with circuit component values determined from analysis of the fields of the dielectric resonator's mode of interest (Fig B-1b-c). Finally, I extract the bare resonator lumped element circuit components which are necessary to build a circuit model which can be generalized to any number of coupled input or output loops (Fig B-1d).

B.1 Electric and magnetic field components

The electric and magnetic fields of a dielectric resonator are modeled as a dielectric wave guide which is open at both ends. Furthermore, we consider the outer boundary of the resonator with radius a as a perfect magnetic conductor which makes the tangential magnetic field component vanish at the sidewalls. We start by considering travelling waves for both

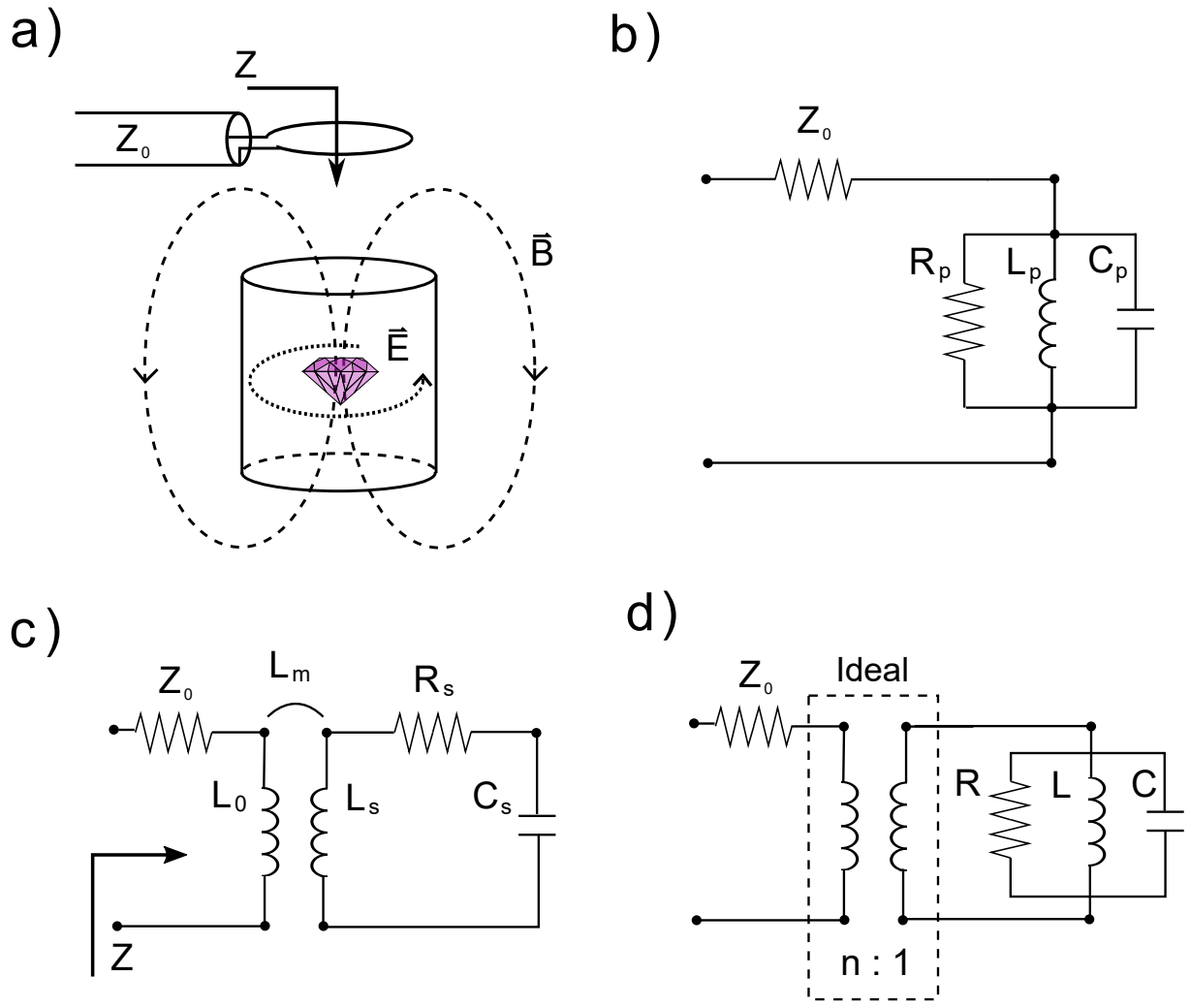

Figure B-1: **Electromagnetic field and equivalent circuit representations of the dielectric resonator** (a) Illustration of physical resonator and $TE_{01\delta}$ mode with impedance Z looking in to coupling loop. (b) Parallel RLC circuit as extracted from electromagnetic field model. Coupling is implicitly contained within calculated circuit components. (c) Circuit in (b) transformed as series RLC circuit. Coupling represented by mutual inductance L_m between loop inductance L_0 and series resonator inductance L_s. (d) Mutual inductance coupling represented as ideal transformer with ratio $n:1$ and lumped element components of Eq. (C.2).

the electric and magnetic fields in cylindrical coordinates,

$$\overline{E}(\rho,\phi,z) = \left[\hat{\rho}E_\rho(\rho,\phi) + \hat{\phi}E_\phi(\rho,\phi) + \hat{z}E_z(\rho,\phi)\right] e^{\pm j\beta z}$$
$$\overline{H}(\rho,\phi,z) = \left[\hat{\rho}H_\rho(\rho,\phi) + \hat{\phi}H_\phi(\rho,\phi) + \hat{z}H_z(\rho,\phi)\right] e^{\pm j\beta z}.$$

We plug the above equations into the source free Maxwell equations,

$$\begin{aligned} \nabla \times \overline{E} &= -j\omega\mu\overline{H} \\ \nabla \times \overline{H} &= j\omega\epsilon\overline{E} \end{aligned} \tag{B.1}$$

and compute the curl using the grad operator in cylindrical coordinates $\left[\frac{\partial}{\partial\rho}, \frac{1}{\rho}\frac{\partial}{\partial\phi}, \frac{\partial}{\partial z}\right]$,

$$\hat{\rho}\left[\frac{1}{\rho}\frac{\partial E_z}{\partial\phi} - (\pm j\beta)E_\phi\right] + \hat{\phi}\left[(\pm j\beta)E_\rho - \frac{\partial E_z}{\partial\rho}\right] + \hat{z}\left[\frac{\partial E_\phi}{\partial\rho} + \frac{E_\phi}{\rho} - \frac{\partial E_\rho}{\partial\phi}\right] = - j\omega\mu\left(\hat{\rho}H_\rho + \hat{\phi}H_\phi + \hat{z}H_z\right)$$

$$\hat{\rho}\left[\frac{1}{\rho}\frac{\partial H_z}{\partial\phi} - (\pm j\beta)H_\phi\right] + \hat{\phi}\left[(\pm j\beta)H_\rho - \frac{\partial H_z}{\partial\rho}\right] + \hat{z}\left[\frac{\partial H_\phi}{\partial\rho} + \frac{H_\phi}{\rho} - \frac{\partial H_\rho}{\partial\phi}\right] = j\omega\epsilon\left(\hat{\rho}E_\rho + \hat{\phi}E_\phi + \hat{z}E_z\right).$$

We then equate each vector component (for both $\overline{E}$ and $\overline{H}$) and solve for the transverse fields E_ρ, E_ϕ, and H_ρ, H_ϕ

$$\begin{aligned} H_\rho &= \frac{-j\beta}{k_c^2}\frac{\partial H_z}{\partial\rho} \\ E_\phi &= \frac{j\omega\mu}{k_c^2}\frac{\partial H_z}{\partial\rho} \\ H_\phi &= 0 \\ E_\rho &= 0, \end{aligned} \tag{B.2}$$

where we define the wave number $k_c^2 = \beta^2 + k_0^2$ and $k_0^2 = \omega^2\epsilon_0\mu_0$. Finally, to find the full expression for the transverse magnetic and electric field components, we solve for the longitudinal part of the magnetic field H_z. H_z is found by solving the Helmholtz equation,

$$\left(\nabla^2 + k^2\right)H_z = 0, \tag{B.3}$$

with the appropriate longitudinal boundary conditions for the dielectric resonator of length L,

$$k = \begin{cases} \sqrt{\epsilon_r}\sqrt{\epsilon_0\mu_0}\omega = \sqrt{\epsilon_r}k_0 & |z| < L/2 \\ \sqrt{\epsilon_0\mu_0}\omega = k_0 & |z| > L/2 \end{cases}$$

with k_0 as the free space resonant frequency wavenumber. H_z must vanish at $\rho = a$ and be finite at $\rho = 0$ which precludes higher order Bessel functions. Matching the boundary conditions and solving for H_z yields,

$$H_z = H_1 J_0(k_c\rho)e^{\pm j\beta z}, \tag{B.4}$$

where H_1 is the field amplitude, $J_n(x)$ are Bessel functions of the first kind of order n, $k_c = \frac{p_{01}}{a}$, and $J_0(p_{01}) = 0$. Finally, plugging H_z into (B.2) yields

$$\begin{aligned} E_\phi &= \frac{j\omega\mu_0 H_1}{k_c} J_0'(k_c\rho)e^{\pm j\beta z} \\ H_\rho &= \pm\frac{j\beta H_1}{k_c} J_0'(k_c\rho)e^{\pm j\beta z}, \end{aligned} \tag{B.5}$$

where the prime indicates a spatial derivative. Considering resonator boundaries the longitudinal magnetic field becomes,

$$\begin{aligned} H_z &= H_1 J_0(k_c\rho)\cos\beta z, \quad |z| < \frac{L}{2} \\ H_z &= H_1 \cos\frac{\beta L}{2} J_0(k_c\rho)e^{-\alpha(|z|-L/2)}, \quad |z| > \frac{L}{2} \end{aligned} \tag{B.6}$$

The radial magnetic field is

$$\begin{aligned} H_\rho &= -\frac{j\beta}{k_c} H_1 J_0'(k_c\rho)\sin\beta z, \quad |z| < \frac{L}{2} \\ H_\rho &= \mp\frac{j\alpha}{k_c} H_1 \cos\frac{\beta L}{2} J_0'(k_c\rho)e^{-\alpha(|z|-L/2)}, \quad |z| > \frac{L}{2} \end{aligned} \tag{B.7}$$

and the electric field is

$$\begin{aligned} E_\phi &= \frac{j\omega\mu_0}{k_c} H_1 J_0'(k_c\rho)\cos\beta z, \quad |z| < \frac{L}{2} \\ E_\phi &= \frac{j\omega\mu_0}{k_c} H_1 \cos\frac{\beta L}{2} J_0'(k_c\rho) e^{-\alpha(|z|-L/2)}, \quad |z| > \frac{L}{2}. \end{aligned} \tag{B.8}$$

We can simplify equations (B.6) - (B.8) by pulling out the longitudinal dependence $f(\tilde{z})$ and including the Bessel function identity $J_0'(x) = -J_1(x)$,

$$\begin{aligned} H_z &= H_1 J_0(k_c\rho) f(\tilde{z}), \\ H_\rho &= -\frac{j\beta}{k_c} H_1 J_1(k_c\rho) f'(\tilde{z}), \\ E_\phi &= -\frac{j\omega\mu_0}{k_c} H_1 J_1(k_c\rho) f(\tilde{z}). \end{aligned} \tag{B.9}$$

and

$$f(\tilde{z}) = \begin{cases} \cos\beta z, & |z| < \frac{L}{2} \\ \cos\frac{\beta L}{2} e^{-\alpha(|z|-L/2)}, & |z| > \frac{L}{2} \end{cases} \tag{B.10}$$

B.2 Power dissipated in the dielectric resonator

Dielectric losses in the resonator are due to bound charges and dipole relaxation, and almost entirely contribute to dissipation of the stored electric energy. We therefore start with the transverse electric field component in (B.9) and solve for the dissipated power as

$$P_d = \frac{1}{2}\int_{\text{resonator}} dv\, \sigma\, |E_\phi|^2 = \frac{1}{2}\int_z\int_\rho\int_\phi \sigma |E_\phi|^2 \rho\, d\phi d\rho dz. \tag{B.11}$$

Since only electric fields within the resonator dissipate real power we have,

$$|E_\phi|^2 = \left(\frac{\omega\mu_0}{k_c}\right)^2 H_1^2 J_1^2(k_c\rho)\cos^2(\beta z),$$

and computing the integral in (B.11) we have

$$P_d = \frac{a^2\pi\sigma L}{4}\left(\frac{\omega\mu_0}{k_c}\right)^2 H_1^2 J_1(p_{01})^2 \left(1 + \frac{1}{\beta L}\sin(\beta L)\right), \tag{B.12}$$

where $\sigma = \omega\epsilon'' = \omega\,\epsilon_r\epsilon_0\tan(\delta)$, and $p_{01} \approx 2.4$.

B.3 Stored electric and magnetic energy

Again, we begin by considering the electric field component of the mode in (B.9) and the electric energy

$$W_e = \frac{1}{4}\int_{\text{all space}} dv\;\epsilon|E_\phi|^2. \tag{B.13}$$

This time however, we have to integrate over all space since the mode extends past the bounds of the dielectric resonator.

$$W_{e,\text{resonator}} = \frac{a^2\pi\epsilon L}{8}\left(\frac{\omega\mu_0}{k_c}\right)^2 H_1^2 J_1(p_{01})^2\left(1+\frac{1}{\beta L}\sin(\beta L)\right)$$
$$W_{e,\text{outside}} = \frac{a^2\pi\epsilon}{4}\left(\frac{\omega\mu_0}{k_c}\right)^2 H_1^2 J_1(p_{01})^2\cos^2\left(\frac{\beta L}{2}\right)\alpha^{-1}.$$

and adding both together yields the total electric energy stored in the electromagnetic mode,

$$W_e = \frac{a^2\pi\epsilon L}{4}\left(\frac{\omega\mu_0}{k_c}\right) H_1^2 J_1(p_{01})^2\left[\frac{1}{2}\left(1+\frac{1}{\beta L}\sin(\beta L)\right)+\frac{1}{\epsilon_r\alpha L}\cos^2\left(\frac{\beta L}{2}\right)\right]. \tag{B.14}$$

Because the magnetic field has two vector components (one along z, the other along ρ) we have to consider both H_z and H_ρ when computing the magnetic energy W_m stored in the mode,

$$W_m = \frac{1}{4}\int_{\text{all space}} dv\;\mu|H|^2 = \frac{1}{4}\int_{\text{all space}} dv\;\mu\,(H_z^2+H_\rho^2), \tag{B.15}$$

which yields,

$$W_{m,\text{resonator}} = \frac{a^2\pi L\mu_0}{4}H_1^2 J_1(p_{01})^2\left(1-\frac{\beta^2}{k_c^2}\right)\frac{1}{2\beta L}\sin(\beta L)$$
$$W_{m,\text{outside}} = \frac{a^2\pi L\mu_0}{4}H_1^2 J_1(p_{01})^2\left(1+\frac{\beta^2}{k_c^2}\right)\left(\frac{1}{2}+\frac{1}{\alpha L}\cos^2\left(\frac{\beta L}{2}\right)\right).$$

Finally, adding everything together yields

$$W_m = \frac{a^2 \pi L \mu_0}{4} H_1^2 J_1(p_{01})^2 \left[\left(1 + \frac{\beta^2}{k_c^2}\right) \left(\frac{1}{2} + \frac{1}{\alpha L} \cos^2\left(\frac{\beta L}{2}\right)\right) + \left(1 - \frac{\beta^2}{k_c^2}\right) \frac{1}{2\beta L} \sin(\beta L) \right] \tag{B.16}$$

B.4 Computing coupled circuit parameters from stored energy

To compute the total impedance (Z) looking into the loop we consider ohm's law,

$$Z^* = \frac{V^*}{I^*} = \frac{1}{2} \frac{V^* V}{\frac{1}{2} I^* V} = \frac{|V|^2}{2P}. \tag{B.17}$$

The total complex power P drawn by the loop-coupled resonator is the real power attributed to dielectric loss P_d and the reactive power P_r attributed to the net energy stored in the electromagnetic field,

$$P = P_d + P_r = P_d + 2\, j\omega\, (W_m - W_e). \tag{B.18}$$

The induced electric potential V arises from integrating the electric field along the loop, or, by use of Stoke's theorem, integrating the magnetic field over the loop area,

$$V = \oint_l \overline{E} \cdot d\bar{l} = \int_S \nabla \times \overline{E} \cdot d\overline{S} = -j\omega\mu \int_S \overline{H} \cdot d\overline{S}. \tag{B.19}$$

Since the transverse component of $\overline{H}$ lies parallel to $d\overline{S}$ (ie. $\int_S H_\rho \cdot d\overline{S} = 0$) we only have to consider the longitudinal component H_z. Approximating the field to be uniform over the loop area (A) yields,

$$V = -j\omega\mu \int_S H_z \cdot d\overline{S} = -j\omega\mu H_1 \cos\left(\frac{\beta L}{2}\right) e^{-\alpha d} A, \tag{B.20}$$

where d is the distance between the loop and the top of the resonator. Finally,

$$|V|^2 = (\omega\mu)^2 H_1^2 \cos^2\left(\frac{\beta L}{2}\right) e^{-2\alpha d} A^2. \tag{B.21}$$

We compactify our notation somewhat by defining the following from equations (B.12),(B.14), and (B.16)

$$\begin{aligned}
\mathbf{X} &= 1 + \left(\frac{1}{\beta L}\sin(\beta L)\right) \\
\mathbf{Y} &= \left[\left(1 + \frac{\beta^2}{k_c^2}\right)\left(\frac{1}{2} + \frac{1}{\alpha L}\cos^2\left(\frac{\beta L}{2}\right)\right) + \left(1 - \frac{\beta^2}{k_c^2}\right)\frac{1}{2\beta L}\sin(\beta L)\right] \\
\mathbf{Z} &= \left[\frac{1}{2}\left(1 + \frac{1}{\beta L}\sin(\beta L)\right) + \frac{1}{\epsilon_r \alpha L}\cos^2\left(\frac{\beta L}{2}\right)\right].
\end{aligned} \tag{B.22}$$

Combining equations (B.12), (B.14), and (B.16) into (B.18), and consequently (B.18) and (B.21) into (B.17), we find the loop-coupled-resonator admittance as

$$\begin{aligned}
Y = \frac{a^4 \pi \sigma L}{2A^2 p_{01}^2} J_1(p_{01})^2 \cos^{-2}\left(\frac{\beta L}{2}\right) e^{2\alpha d} \cdot \mathbf{X} \\
- j\omega^{-1} \frac{\pi a^2 L}{\mu A^2} J_1(p_{01})^2 \cos^{-2}\left(\frac{\beta L}{2}\right) e^{2\alpha d} \cdot \mathbf{Y} \\
j\omega \frac{\pi a^4 L \epsilon}{p_{01}^2 A^2} J_1(p_{01})^2 \cos^{-2}\left(\frac{\beta L}{2}\right) e^{2\alpha d} \cdot \mathbf{Z}.
\end{aligned} \tag{B.23}$$

The above equation has a real part ($\propto \mathbf{X}$), an imaginary magnetic part ($\propto \mathbf{Y}$), and an imaginary electric part ($\propto \mathbf{Z}$) which act as the resistive, inductive, and capacitive components of the impedance, respectively. The admittance Y therefore has the form

$$Y = \frac{1}{R_p} + \frac{1}{j\omega L_p} + j\omega C_p. \tag{B.24}$$

By matching terms with $j\omega$, we identify the parameters that make up the lumped element circuit components of an analogous parallel RLC resonator (Fig. B-1b).

$$\begin{aligned}
R_p &= \frac{2A^2 p_{01}^2}{\pi a^4 L \sigma} \left[J_1(p_{01})\right]^{-2} \cos^2\left(\frac{\beta L}{2}\right) e^{-2\alpha d} \cdot \mathbf{X}^{-1} \\
L_p &= \frac{\mu A^2}{\pi a^2 L} \left[J_1(p_{01})\right]^{-2} \cos^2\left(\frac{\beta L}{2}\right) e^{-2\alpha d} \cdot \mathbf{Y}^{-1} \\
C_p &= \frac{\pi a^4 L \epsilon}{A^2 p_{01}^2} J_1(p_{01})^2 \cos^{-2}\left(\frac{\beta L}{2}\right) e^{2\alpha d} \cdot \mathbf{Z}.
\end{aligned} \tag{B.25}$$

It's important to note that the lumped element circuit components in (B.25) implicitly contain the mutual inductance L_m between the loop and the resonator. As a result, the values will change as a function of the coupling. However, the parallel circuit in Fig. B-1b can be transformed into an equivalent series RLC circuit representation [109] with explicit coupling between the loop and resonator (Fig. B-1c). In the next section, I compute the bare resonator inductance L_s and the mutual inductance L_m, discover their relationship to the coupled parallel inductance L_p, and compute the other uncoupled series lumped element circuit components.

B.5 Bare resonator lumped element circuit components

We can calculate the inductance L_s of the bare resonator directly from the magnetic energy and current in the resonator. The displacement current density $\vec{J}_d = \epsilon \partial \vec{E}/\partial t$ gives the current

$$I = \int \vec{J}_d \cdot d\vec{A} = \frac{2\epsilon_r k_0^2 H_1 \sin \frac{\beta L}{2}}{k_c^2 \beta}. \tag{B.26}$$

Using the average magnetic energy $W_m = L_s I^2/4$ then gives the resonator inductance

$$L_s = \frac{\mu_0 \pi \ a^2 L k_c^4 \beta^2}{4\epsilon_r^2 k_0^4} \frac{J_1(x_{01})^2}{\sin^2 \frac{\beta L}{2}} \cdot \mathbf{Y} \tag{B.27}$$

and we find, as expected, that L_s is independent of the coupling loop area or coupling loop distance above the resonator.

The mutual inductance L_m can be explicitly calculated from the voltage induced in the coupling loop due to current in the resonator,

$$V = L_m \frac{dI}{dt} = j\omega L_m I. \tag{B.28}$$

We have already computed I from equation (B.26) and V in (B.20), then

$$L_m = \frac{V}{j\omega I} = \frac{\mu A k_c^2 \beta}{2\epsilon_r k_0^2} \cot\left(\frac{\beta L}{2}\right) e^{-\alpha d}. \tag{B.29}$$

To discover the relationship between L_s, L_m, and L_p we start by considering that the

mutual inductance between two loops can be represented as $L_m = M\sqrt{L_1 L_2}$, where $L_{1,2}$ are the arbitrary inductances of the two mutually coupled loops, and M is a unitless coupling coefficient. We know that the bare resonator inductance L_s is independent of the coupling and thus the mutual inductance will follow

$$L_m^2 = M^2 L_0 L_s, \tag{B.30}$$

where the quantity $M^2 L_0$ is to be discovered. Solving for the product $M^2 L_0$, and plugging in for L_m and L_s yields

$$M^2 L_0 = \frac{L_m^2}{L_s} = \frac{\mu A^2}{\pi a^2 L} \left[J_1(p_{01})\right]^{-2} \cos^2\left(\frac{\beta L}{2}\right) e^{-2\alpha d} \cdot \mathbf{Y}^{-1}. \tag{B.31}$$

Comparing (B.31) to (B.25) we find that $M^2 L_0 = L_p$. The relationship between L_m, L_s and L_p therefore is

$$L_m^2 = L_p L_s, \tag{B.32}$$

and will aid in deriving the rest of the uncoupled series lumped element circuit components (R_s and C_s). We begin by noting that on resonance, both coupled and uncoupled circuits should resonate at the same frequency

$$\frac{1}{\sqrt{L_p C_p}} = \frac{1}{\sqrt{L_s C_s}}. \tag{B.33}$$

Solving for C_s and using the relationship in (B.32) we find

$$C_s = \frac{L_p^2}{L_m^2} C_p. \tag{B.34}$$

We find the relationship between resistances from the Q-factor

$$Q = \frac{\omega L_p}{R_p} = \frac{R_s}{\omega L_s}, \tag{B.35}$$

where, solving for R_s and using the relationship $\omega = 1/\sqrt{L_s C_s}$, and equation (B.32),

$$R_s = \frac{L_m^2}{L_p C_p R_p}. \tag{B.36}$$

To summarize, the relationship between the coupled parallel circuit elements depicted in Fig. B-1b and the uncoupled series circuit elements depicted in Fig. B-1c is

$$\begin{aligned} L_s &= \frac{L_m^2}{L_p}, \\ C_s &= \frac{C_p L_p^2}{L_m^2}, \\ R_s &= \frac{L_m^2}{C_p L_p R_p}. \end{aligned} \tag{B.37}$$

These circuit values represent the bare resonator apart from the coupling loop. In the following section, we use the uncoupled series circuit components to build a lumped element circuit model which can easily facilitate multiple coupling loops, and for which introducing the spin-ensemble-coupled admittance is a simple exercise in classical circuit theory.

B.6 Comparing analytical and numerical RLC values

Using the equations in B.37 we can compute values for the series equivalent circuit components given the cavity parameters in section 3.2.1. We calculate

$$L_s = 3.88 \text{ nH}, \, C_s = 0.776 \text{ pF}, \text{and} \, R_s = 3.17 \text{ m}\Omega. \tag{B.38}$$

Using ANSYS HFSS we can obtain the equivalent series RLC circuit component values of the bare cavity (i.e. the resonator cavity and diamond system in the absence of any spin polarization by the laser) which are computed using the following procedure: first, finite element modeling software (Ansys HFSS) calculates the $\vec{E}$ and $\vec{B}$ fields for a given stored energy in the cavity; next, the Ampere-Maxwell law is applied to determine the RMS displacement current I_D^{RMS}; third, the stored magnetic energy is set equal to $\frac{1}{2} L_s (I_D^{\text{RMS}})^2$ to determine the value of L_s; and finally, the capacitance is determined from the resonant

frequency and the inductance, with $C_s = \frac{1}{\omega_c^2 L_s}$. The series resistance R_s is computed by first experimentally measuring the composite cavity's unloaded quality factor Q_0, with $R_s = \frac{1}{Q_0}\sqrt{\frac{L_s}{C_s}}$. This procedure gives

$$L_s = 3.75 \text{ nH}, C_s = 0.803 \text{ pF}, \text{and } R_s = 3.15 \text{ m}\Omega. \tag{B.39}$$

These results quantitatively agree with the analytical model of the electromagnetic fields of the resonator $\text{TE}_{01\delta}$ mode described above to within 3.5%.

Appendix C

Generalized circuit model

For ease of analysis a further transformation can then be made, where the parallel RLC circuit described by the lumped elements in Eq. (B.25) is replaced by an ideal-transformer-coupled parallel RLC circuit with lumped elements constructed from the series equivalent RLC circuit (Fig. B-1c). The benefit of this construction is three fold: far from resonance the correct phase relationship between the voltage and current is maintained, the lumped element components remain independent from the coupling which allows for introducing an arbitrary number of additional loop couplings without loss of generality, and, finally, computation of the circuit reflection (and transmission in the case of added output couplings) coefficient becomes a trivial exercise in classical circuit theory.

C.1 Transformer coupled circuit

We rewrite Eq. (B.25) in terms of the series equivalent circuit values Eq. (B.37) and an effective turns ratio $n:1$, where we follow traditional electrical engineering convention and define n as the ratio of primary-to-secondary turns of an ideal transformer. The effective turns ratio is given by

$$n = \frac{L_m}{L_s} = \frac{L_p}{L_m}. \tag{C.1}$$

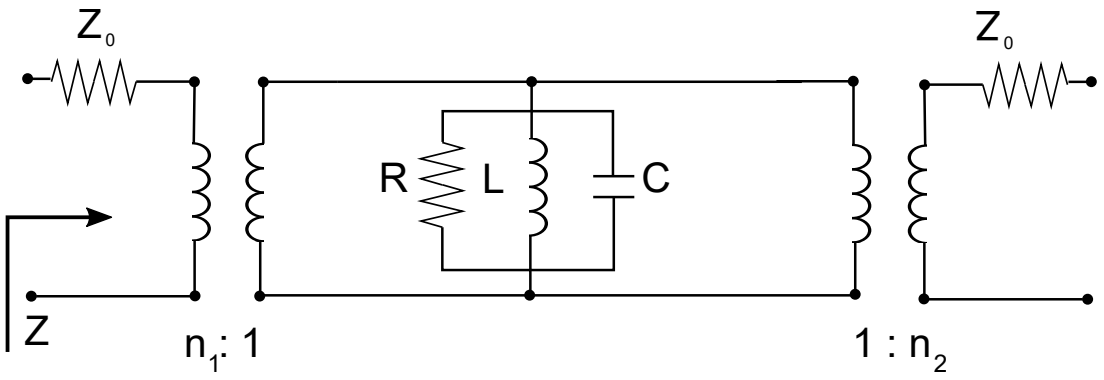

Figure C-1: **Full lumped element circuit model** Illustration of the ideal-transformer-coupled parallel RLC circuit with out- and input couplings. The lumped element components are Eq. (C.2) and the input and output coupling turns ratios are n_1 and n_2 respectively.

The modification of the series inductance as a result of this transformation is given by $L_s' = L_s - n^2 L_0$, where L_0 is the loop inductance. Here, however, we have $n^2 L_0 << L_s$, and thus we set $L_s' \approx L_s$ [109]. The ideal-transformer-coupled parallel RLC lumped element circuit components are

$$L = L_s \tag{C.2}$$

$$C = C_s \tag{C.3}$$

$$R = \frac{\omega^2 L_s^2}{R_s}. \tag{C.4}$$

As a result of this construction, we can add an additional output coupler $(1\!:\!n)$ to compute the transmission coefficient without modifying the lumped element circuit components in the model (Fig. C-1). We write the effective turns ratio of the input and output coupler as n_1 and n_2 respectively. Critical coupling of the input loop alone (with no output coupling) is achieved when $n_1 = \sqrt{Z_0/R}$, where Z_0 is the input line impedance (typically 50 Ω). The effective turns ratios can be controlled by changing the distance from the loop to the resonator.

C.2 Generalized reflection and transmission coefficients

The circuit representation for a ideal-transformer coupled parallel RLC resonator is depicted in Fig. C-1. As mentioned above, we define the turns ratio n_a, where a represents the index of the coupled line, as

$$n_a = \frac{N_p}{N_s}, \tag{C.5}$$

where N_p is the number of turns on the primary coil and N_s the number on the secondary coil. As a result, the voltage and current relations at the transformer are as follows,

$$\begin{aligned} V_s &= \frac{N_s}{N_p} V_p = \frac{1}{n_1} V_p, \\ I_s &= \frac{N_p}{N_s} I_p = n_1 I_p. \end{aligned} \tag{C.6}$$

We then write out the open- and closed-circuit equations in therms of the voltages across and the currents through each inductor,

$$\begin{aligned} V_p &= n_1 V_s + 0 I_s \\ I_p &= 0 V_s + \frac{1}{n_1} I_s. \end{aligned} \tag{C.7}$$

From here we build the matrix for the transformer as,

$$\tilde{N}_1 = \begin{bmatrix} n_1 & 0 \\ 0 & \frac{1}{n_1} \end{bmatrix}. \tag{C.8}$$

We identify Z_0 as V_p/I_p, then

$$Z_0 = \frac{V_p}{I_p} = \frac{n_1 V_s}{\frac{1}{n_1} I_s} = n_1^2 \frac{V_s}{I_s} = n_1^2 Z.$$

On resonance, the capacitive and inductive reactances cancel each other out and $Z = R$. Consequently, a critically coupled resonator has turns ratio

$$n_1 = \sqrt{\frac{Z_0}{R}}. \tag{C.9}$$

Given this construction, we identify, for transmission configurations depicted in Fig. C-1 the out-coupling transformer as the inverse of the in-coupling transformer,

$$\tilde{N}_2 = \begin{bmatrix} \frac{1}{n_2} & 0 \\ 0 & n_2 \end{bmatrix}. \tag{C.10}$$

In matrix form, the parallel admittance is represented as,

$$\tilde{Y} = \begin{bmatrix} 1 & 0 \\ Y & 1 \end{bmatrix}, \tag{C.11}$$

and the full circuit response is computed by

$$A_{ij} = \tilde{N}_1 \tilde{Y} \tilde{N}_2 = \begin{bmatrix} n_1/n_2 & 0 \\ Y/(n_1 n_2) & n_2/n_1 \end{bmatrix}.$$

We can now build the circuit reflection (Γ) and transmission (T) coefficients by use of [123]

$$\Gamma_{\text{struct}} = \frac{A_{00} + A_{01}/Z_0 - A_{10}Z_0 - A_{11}}{A_{00} + A_{01}/Z_0 + A_{10}Z_0 + A_{11}} \tag{C.12}$$

$$\mathrm{T}_{\text{struct}} = \frac{2}{A_{00} + A_{01}/Z_0 + A_{10}Z_0 + A_{11}}, \tag{C.13}$$

the result of which are the generalized circuit reflection and transmission coefficients with input impedance Z_0 and parallel resonator admittance Y,

$$\Gamma = \frac{n_1^2 + n_2^2 - YZ_0}{n_1^2 + n_2^2 + YZ_0}, \tag{C.14}$$

$$\mathrm{T} = \frac{2n_1 n_2}{n_1^2 + n_2^2 + YZ_0}. \tag{C.15}$$

We can now simply substitute in the admittance of the RLC resonator once we have determined how the spin ensemble modifies the bare resonator impedance.

C.3 Spin-coupled resonator admittance

To incorporate the spin ensemble's effect on the composite cavity response, consider the contribution of the spin-ensemble magnetization to the flux through the resonator. When a coil of inductance L is filled with a material of magnetic susceptibility χ_m, its inductance increases to $L(1+\chi_m)$ [147]. For the model investigated here, the complex susceptibility modifies the series inductance to $L(1+\chi'-j\chi'')$.

$$Y = \frac{1}{R} + \frac{1}{j\omega L(1+\chi)} + j\omega C. \tag{C.16}$$

Using the approximation that $\chi << 1$ the total admittance of the composite cavity can be written as

$$Y \approx \frac{1}{R} + \frac{1}{j\omega L} + j\omega C - \frac{\chi}{j\omega L}. \tag{C.17}$$

When χ is then written in terms of its real and imaginary components, we can collect terms and write the admittance in a more illuminating form

$$Y \approx \left[\frac{1}{R} + \frac{\chi''}{\omega L}\right] + \left[\frac{1}{j\omega L}(1-\chi') + j\omega_d C\right]. \tag{C.18}$$

Eq (C.18) shows the contribution of the absorption to the real part and the dispersion to the imaginary part of the impedance. Now that we've identified how the spin-ensemble magnetization influences the composite resonator's admittance, we can build the spin-coupled reflection and transmission coefficients by introducing (C.17) into the generalized circuit reflection and transmission coefficients of Eqs. (C.14) and (C.15),

$$\Gamma = -1 + \frac{2n_1^2/Z_0}{1/R + j2C(\omega_d - \omega_c) + n_1^2/Z_0 + n_2^2/Z_0 - \chi(j\omega_d L)^{-1}} \tag{C.19}$$

$$T = \frac{2n_1 n_2/Z_0}{1/R + j2C(\omega_d - \omega_c) + n_1^2/Z_0 + n_2^2/Z_0 - \chi(jL\omega_d)^{-1}}. \tag{C.20}$$

Here we have replaced $\omega = \omega_d$ and $\omega_c = 1/\sqrt{LC}$; a necessary distinction in order to decouple the driving field from the bare cavity resonance.

Appendix D

Spin ensemble dynamics

This section aims at calculating the components of the spin-ensemble's complex magnetic susceptibility $\chi = \chi' - j\chi''$ by analyzing the dynamics of a spin magnetization $\vec{M}$ which is subjected to a magnetic vector field $\vec{H}$. As a result of this analysis we will be able to build the final reflection and transmission coefficients which entirely describe the spin-ensemble-cavity-coupled system. The Bloch equations [21], describe the time evolution of the magnetization components, and introduce the phenomenological longitudinal relaxation T_1 and transverse relaxation T_2

$$\dot{M}_x = \gamma \left(M_y H_z - M_z H_y \right) - \frac{1}{T_2} M_x \tag{D.1}$$

$$\dot{M}_y = \gamma \left(M_z H_x - M_x H_z \right) - \frac{1}{T_2} M_y \tag{D.2}$$

$$\dot{M}_z = \gamma \left(M_x H_y - M_y H_x \right) - \frac{1}{T_1} (M_z - M_0), \tag{D.3}$$

where γ is the spin gyromagnetic ratio, and $M_0 = \chi_0 H_0$ is the equilibrium magnetization due to a static spin susceptibility χ_0 in a static magnetic field H_0. We now consider such a static magnetic field, and introduce a dynamic field H_1 rotating at an angular frequency ω such that

$$\vec{H} = \hat{x} \left[H_1 \cos \omega t \right] + \hat{y} \left[H_1 \sin \omega t \right] + \hat{z} \left[H_0 \right]. \tag{D.4}$$

In the frame rotating at ω the magnetization components become

$$\tilde{M}_x = \tilde{M}_x \cos\omega t - \tilde{M}_y \sin\omega t \tag{D.5}$$

$$\tilde{M}_x = \tilde{M}_x \sin\omega t + \tilde{M}_y \cos\omega t \tag{D.6}$$

$$\tilde{M}_z = M_z, \tag{D.7}$$

which yields

$$\dot{\tilde{M}}_x = -\frac{\tilde{M}_x}{T_2} + (\omega - \omega_0)\tilde{M}_y \tag{D.8}$$

$$\dot{\tilde{M}}_y = -(\omega - \omega_0)\tilde{M}_x - \frac{\tilde{M}_y}{T_2} - \omega_1 M_z \tag{D.9}$$

$$\dot{\tilde{M}}_z = \omega_1 \tilde{M}_y - \frac{1}{T_1}(\tilde{M}_z - M_0). \tag{D.10}$$

Here we have defined $\omega_0 = -\gamma H_0$ and $\omega_1 = -\gamma H_1$. We are only interested in the steady state solutions ($\dot{\tilde{M}}_x = \dot{\tilde{M}}_y = \dot{\tilde{M}}_z = 0$) of eqs. (D.8)-(D.10) since we will be driving the spins using a single continuous microwave tone. Solving the steady-state coupled equations for the magnetization components in the rotating frame yields,

$$\tilde{M}_x = \frac{(\omega - \omega_0)\gamma H_1 T_2^2}{1 + ((\omega - \omega_0)T_2)^2 + \gamma^2 H_1^2 T_1 T_2} M_0 \tag{D.11}$$

$$\tilde{M}_y = \frac{\gamma H_1 T_2}{1 + ((\omega - \omega_0)T_2)^2 + \gamma^2 H_1^2 T_1 T_2} M_0 \tag{D.12}$$

$$\tilde{M}_z = \frac{1 + ((\omega - \omega_0)T_2)^2}{1 + ((\omega - \omega_0)T_2)^2 + \gamma^2 H_1^2 T_1 T_2} M_0. \tag{D.13}$$

We now evaluate the steady-state solution to the Bloch equations under the application of a linearly polarized field $H(t) = H_1 \cos\omega t$. We note that the susceptibility χ obeys $\vec{M} = \chi\vec{H}$, and as such can be evaluated by [1]

$$\chi' = \frac{\tilde{M}_x}{2H_1} \tag{D.14}$$

$$\chi'' = \frac{\tilde{M}_y}{2H_1}. \tag{D.15}$$

Replacing $M_0 = \chi_0 H_0 = -\chi_0 \omega_0/\gamma$ yields the magnetic susceptibilities

$$\chi' = -\frac{1}{2}\chi_0 \frac{\omega_0(\omega-\omega_0)T_2^2}{1+(\omega-\omega_0)^2T_2^2+\left(\frac{\gamma H_1}{2}\right)^2 T_1 T_2} \tag{D.16}$$

$$\chi'' = \frac{1}{2}\chi_0 \frac{\omega_0 T_2}{1+(\omega-\omega_0)^2T_2^2+\left(\frac{\gamma H_1}{2}\right)^2 T_1 T_2}. \tag{D.17}$$

To aid in deriving the final reflection and transmission coefficients we substitute ω for the driving field ω_d, ω_0 with the spin resonance frequency ω_s, and rewrite the complex susceptibility into the compact form,

$$\chi = -\frac{\chi_0 \omega_s T_2}{2} \frac{j}{1+j(\omega_d-\omega_s)T_2+\frac{\left(\gamma B_1^{\perp}/2\right)^2 T_1^{\mathrm{op}} T_2}{1-j(\omega_d-\omega_s)T_2}}. \tag{D.18}$$

Here, $B_1^{\perp} = \mathfrak{n}_{\perp} B_1$ is the projection of the driving field ($\mu_0 H_1 = B_1$) onto the plane perpendicular to each of the NV axes (consequently $\mathfrak{n}_{\perp} = \sqrt{\frac{2}{3}}$), T_1^{op} is the optical pumping relaxation time (in analogy to the thermalization time T_1 for an NMR system), and T_2 is the decoherence time.

Appendix E

Quantum mechanical system parameters

E.1 Vacuum magnetic field B_v

In this section we outline the steps that go into calculating the single spin-photon coupling rate g_s. The single spin-photon coupling describes the coupling of a single spin to the vacuum field in the cavity. We start by considering the time-averaged energy density in the $\mathrm{TE}_{01\delta}$ mode of the cavity,

$$\langle \mathcal{E} \rangle = \underbrace{\int_{\text{all space}} \frac{1}{4}\,\epsilon_0\,|E|^2\,d^3\vec{r}}_{W_e} + \underbrace{\int_{\text{all space}} \frac{1}{4}\,\mu_0\,|H|^2\,d^3\vec{r}}_{W_m}. \tag{E.1}$$

Where $\langle \mathcal{E} \rangle = W_e + W_m$ and, on resonance $W_e = W_m$. Then, making the on-resonance approximation we find

$$\langle \mathcal{E} \rangle = 2\,W_m. \tag{E.2}$$

In section B.3 we calculated the magnetic energy stored in the mode on resonance as (see eq. B.16),

$$W_m = \frac{a^2 \pi L \mu_0}{4} H_1^2 \left[J_1(p_{01})\right]^2 \cdot \mathbf{Y}. \tag{E.3}$$

Plugging into eq. E.2 we get

$$\langle \mathcal{E} \rangle = \hbar\omega = 2\,\frac{\pi a^2 L}{4}\,\left[J_1(p_{01})\right]^2\,\mu_0\,H_1^2 \cdot \mathbf{Y}. \tag{E.4}$$

Now we note a few things:

1. $\pi a^2 L$ is the total resonator volume and we'll call it V_{res}.

2. $[J_1(\rho_{01})]^2$ is unitless and is $\approx (1/2)^2$.

3. $\mathbf{Y}$ is also unitless and is ≈ 0.8 for our experimental system.

Now using $\mu_0 H_1 = B_v$ we have,

$$B_v = \sqrt{2}\,\sqrt{\frac{\mu_0\,\hbar\omega}{V_{\text{res}}\,[J_1(p_{01})]^2\,\mathbf{Y}}}, \tag{E.5}$$

which describes the vacuum B-field in the cavity, at the $\text{TE}_{01\delta}$ mode anti-node. We identify that the factor $[V_{\text{res}}\,[J_1(p_{01})]^2\,\mathbf{Y}]$ represents the area in the center of the cavity over which the field amplitude is maximally concentrated. This collection of terms is often referred to as the cavity mode volume which, for an arbitrary cavity geometry, is calculated as

$$V_{\text{cav}} = \frac{\int |\mathbf{B}(\mathbf{r})|^2 dV}{|\mathbf{B}_{\text{max}}|^2}. \tag{E.6}$$

The RMS-vacuum B-field at the cavity anti-node then is described by the equation

$$B_v^{\text{RMS}} = \sqrt{\frac{\mu_0\,\hbar\omega}{V_{\text{cav}}}}. \tag{E.7}$$

E.2 Single spin-photon coupling g_s

The transition dipole moment m_0 and the oscillating magnetic field $\vec{B}_1$ projected onto the transverse plane induce Rabi oscillations Ω_{R}.

$$\hbar\Omega_{\text{R}} = \frac{m_0}{2}\,\mathfrak{n}_\perp\,B_v^{\text{RMS}}. \tag{E.8}$$

Here $B_v^{\text{RMS}}(\vec{r})$ is the RMS vacuum B-field in the cavity at the spin defect location $\vec{r}$ and $\mathfrak{n}_\perp$ denotes the projection of $\hat{B}_v^{\text{RMS}}$ onto a plane perpendicular to the NV axis (i.e., the component of $\vec{B}_v^{\text{RMS}}$ capable of driving a transition $|m_s = 0\rangle \rightarrow |m_s = \pm 1\rangle$). We take $\vec{B}_v^{\text{RMS}} \parallel$

$\vec{B}_1$, where $\vec{B}_1$ is the magnetic field of the cavity-enhanced MW drive. The factor of $\frac{1}{2}$ results from a combination of the rotating wave approximation and the linear polarization of B_1 in the lab frame. For estimation purposes, we can assume the B_1 field projects equally onto all four NV axes so that $\mathfrak{n}_\perp = \sqrt{\frac{2}{3}}$. Assuming the spins are located at the cavity antinode, which is a reasonable approximation for this geometry, we have

$$g_s = \frac{m_0}{2\hbar}\,\mathfrak{n}_\perp\, B_v^{\mathrm{RMS}}, \tag{E.9}$$

where we have replaced Ω_{R} with g_s since we are interested in oscillations between a single spin in the cavity and the vacuum field. Here $m_0 = -g_e\,\mu_B\,m_s$, where for the NV $m_s = \{-1, 0, +1\}$. Then for $m_0 = g_e\mu_B$ and $m_s = -1$,

$$g_s = \frac{\gamma}{2}\,\mathfrak{n}_\perp B_v^{\mathrm{RMS}}, \tag{E.10}$$

where $\gamma = \frac{g_e\mu_B}{\hbar}$ is the spin gyromagnetic ratio. Finally, inserting eq. (E.7) into the above we have [138, 180],

$$g_s = \frac{\gamma}{2}\,\mathfrak{n}_\perp\sqrt{\frac{\mu_0\,\hbar\omega}{V_{\mathrm{cav}}}}. \tag{E.11}$$

Based on finite element software modeling of the cavity (ANSYS HFSS), we find that $g_s/(2\pi) = 0.02 \pm 0.001$ Hz. When the number of cavity photons $n_{\mathrm{cav}} \gg 1$, the Rabi frequency Ω_R can be approximated as

$$\Omega_R \approx \gamma\mathfrak{n}_\perp\sqrt{\frac{\hbar\omega_c\mu_0}{V_{\mathrm{cav}}}}\sqrt{n_{\mathrm{cav}}}. \tag{E.12}$$

Then we have

$$g_s = \frac{\Omega_R}{2\sqrt{n_{\mathrm{cav}}}}. \tag{E.13}$$

E.3 Cooperativity ξ

The collective cooperativity is given by [154]

$$\xi = \frac{4g_{\mathrm{eff}}^2}{\kappa_c\kappa_s}, \tag{E.14}$$

where $\kappa_c = \omega_c/Q_L$ is the cavity loss rate and κ_s is the spin decoherence time (each in angular frequency units).

E.4 Reflection and transmission using quantum mechanical parameters

In this section, I introduce χ as given in eq. (D.18) back into the reflection eq. (C.19) and transmission eq. (C.20) and make the appropriate substitutions in order to formulate the resulting equations in terms of the quantum mechanical parameters of the system.

We identify $\kappa_{c0} = 1/(RC)$, $\kappa_{c1} = n_1^2/(Z_0 C)$, and $\kappa_{c2} = n_2^2/(Z_0 C)$. Furthermore, the approximation $\omega_d \approx \omega_c$ and the substitutions $\kappa_s = 2/T_2$ and $\kappa_{\text{op}} = 1/T_1^{\text{op}}$ and the relationship

$$\left(\gamma \frac{B_1^{\perp}}{2}\right)^2 = g_s^2 n_{\text{cav}} \tag{E.15}$$

between the single-spin-photon coupling g_s and the driving magnetic field B_1, along with the relationship

$$g_{\text{eff}}^2 = \frac{\chi_0}{4}\omega_c \omega_s \tag{E.16}$$

between the effective collective coupling g_{eff} and the static susceptibility χ_0, gives the reflection and transmission expressions

$$\Gamma = -1 + \frac{\kappa_{c1}}{\frac{\kappa_{c0}+\kappa_{c1}+\kappa_{c2}}{2} + j(\omega_d - \omega_c) + \frac{g_{\text{eff}}{}^2}{\frac{\kappa_s}{2} + j(\omega_d - \omega_s) + \frac{g_s^2 n_{\text{cav}} \kappa_s/(2\kappa_{op})}{\frac{\kappa_s}{2} - j(\omega_d - \omega_s)}}} \tag{E.17}$$

$$\text{T} = \frac{\sqrt{\kappa_{c1}\kappa_{c2}}}{\frac{\kappa_{c0}+\kappa_{c1}+\kappa_{c2}}{2} + j(\omega_d - \omega_c) + \frac{g_{\text{eff}}{}^2}{\frac{\kappa_s}{2} + j(\omega_d - \omega_s) + \frac{g_s^2 n_{\text{cav}} \kappa_s/(2\kappa_{op})}{\frac{\kappa_s}{2} - j(\omega_d - \omega_s)}}}. \tag{E.18}$$

These are equivalent to those obtained through the circuit QED treatment [38, 65]. To incorporate the inhomogeneous distribution of spin resonance frequencies, we integrate the spin response over the appropriate probability density function $\rho(\Delta)$ where, for example, for inhomogeneous distributions due to crystal strain, $\rho(\Delta)$ is given by a Gaussian probability

density function. The full reflection and transmission coefficients become

$$\Gamma = -1 + \frac{\kappa_{c1}}{\frac{\kappa_{c0}+\kappa_{c1}+\kappa_{c2}}{2} + j(\omega_d - \omega_c) + \int_{-\infty}^{\infty} \rho(\Delta) \left[\frac{g_{\text{eff}}^2}{\frac{\kappa_s}{2} + j(\omega_d - \omega_s - \Delta) + \frac{g_s^2 n_{\text{cav}} \kappa_s / (2\kappa_{op})}{\frac{\kappa_s}{2} - j(\omega_d - \omega_s - \Delta)}} \right] d\Delta} \tag{E.19}$$

$$T = \frac{\sqrt{\kappa_{c1}\kappa_{c2}}}{\frac{\kappa_{c0}+\kappa_{c1}+\kappa_{c2}}{2} + j(\omega_d - \omega_c) + \int_{-\infty}^{\infty} \rho(\Delta) \left[\frac{g_{\text{eff}}^2}{\frac{\kappa_s}{2} + j(\omega_d - \omega_s - \Delta) + \frac{g_s^2 n_{\text{cav}} \kappa_s / (2\kappa_{op})}{\frac{\kappa_s}{2} - j(\omega_d - \omega_s - \Delta)}} \right] d\Delta}. \tag{E.20}$$

Appendix F

AC bias field optimization

F.1 Bias field resonant circuit

The AC magnetic bias field is produced by a 49 mm long, three-layer coil of 20 American Wire Gauge (AWG) magnet wire. The total inductance of the coil is $L = 1.03$ mH which was measured using an HP4192A LF impedance analyzer at 2 kHz. The equivalent series resistance (R) at 2 kHz is 1.1 Ω and was measured using the same device. The resonant circuit topology is depicted in Fig. F-1a. Capacitor $C_1 = 5.27$ μF along with the bias field coil L build the parallel resonant circuit. Capacitor $C_2 = 0.95$ μF acts as an impedance matching reactance which allows maximum power transfer from the RF source to the load at 2 kHz. We measure the coil Q-factor by applying an AM modulated square wave with a 70 Hz modulation frequency and 100% AM modulation depth (Fig. F-1b). We fit the envelope of the decaying sinusoid to an exponential function, and extract a Q factor of ≈ 6 [54].

F.2 Bias field frequency optimization

The finite time required (on average) to optically initialize a spin (T_1^{op}) places a constraint on the AC magnetic bias field frequency. To determine the optimal sweeping frequency, we operate the bias field coil in a non-resonant configuration, and apply frequencies between 100 Hz and 10 kHz while measuring the maximal reflected voltage. Because the coil reactance is frequency dependent, we adjust the amplifier gain to ensure the same field magnitude

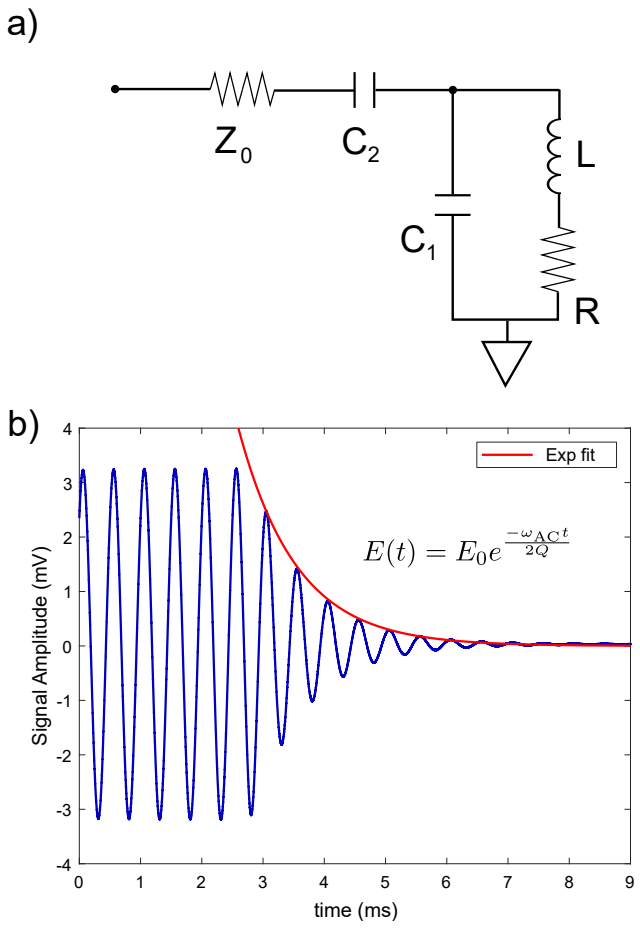

Figure F-1: **RLC resonant AC bias field circuit** (a) The resonant bias field circuit consists of tank circuit comprised of the coil inductance L and the parallel capacitance C_1. Matching the load impedance Z_0 to the tank circuit is accomplished using a series capacitor C_2. (b) The Q is measured by applying an AM modulated square wave to the AC bias field coil while measuring the signal decay (—) using a proximal and concentric pickup coil. We fit (—) the envelope of the decaying sinusoid to extract the coil Q factor.

is applied for each measurement. We apply the working laser power (3W) and, at each frequency, measure the signal to noise ratio (SNR) of the reflected MW signal. The SNR increases almost linearly until approximately 1.5 kHz at which point the curve flattens out (Fig. F-2). The SNR begins to decrease at 5 kHz which quantitatively agrees with our estimate $T_1^{op} \approx 50\ \mu s$ as it takes up to $5\,T_1^{op}$ to fully initialize the ensemble. We choose to operate the bias field at 2 kHz because it offers near optimal SNR while maintaining a low coil reactance. A high coil reactance increases the necessary voltage and consequently the power required to apply the minimum field necessary to sweep three-of-four NV resonances

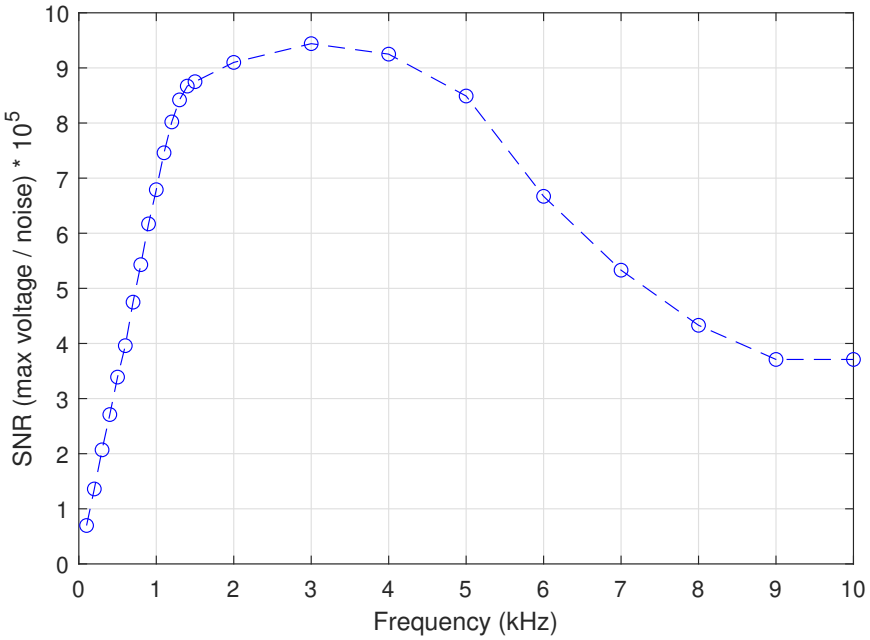

Figure F-2: **Optimizing bias field frequency** Using a non-resonant circuit configuration we measure the maximum signal-to-noise ratio of the cavity readout spectrum in figure 5-1 at varying frequencies. The plateau between 2 kHz and 4 kHz indicates that for optimal sensitivity, the AC bias field frequency can lie anywhere within that range.

past the cavity resonance.

Appendix G

Calibrating the magnetometer output

G.1 Calibration matrix

We relate a shift in the peaks in the cavity readout spectrum $\Delta\tau_i$ of a particular NV axis $i = \lambda, \kappa, \phi, \chi$ to changes in the magnetic field via a linear transformation matrix $\mathbf{A}$,

$$\mathbf{A} = \begin{bmatrix} \frac{\partial\tau_\lambda}{\partial B_x} & \frac{\partial\tau_\lambda}{\partial B_y} & \frac{\partial\tau_\lambda}{\partial B_z} \\ \frac{\partial\tau_\phi}{\partial B_x} & \frac{\partial\tau_\phi}{\partial B_y} & \frac{\partial\tau_\phi}{\partial B_z} \\ \frac{\partial\tau_\kappa}{\partial B_x} & \frac{\partial\tau_\kappa}{\partial B_y} & \frac{\partial\tau_\kappa}{\partial B_z} \\ \frac{\partial\tau_\chi}{\partial B_x} & \frac{\partial\tau_\chi}{\partial B_y} & \frac{\partial\tau_\chi}{\partial B_z} \end{bmatrix}. \tag{G.1}$$

In our implementation we measure three-of-four orientations, and thus use a reduced matrix where the last row (corresponding to shifts of τ_χ) is dropped. We determine $\mathbf{A}$ experimentally by applying perturbing fields $\Delta B_{j=x,y,z}$ and measuring changes in the peaks $\Delta\tau_{\pm i}$. Each element of $\mathbf{A}$ is then determined by computing

$$\frac{\partial\tau_i}{\partial B_j} = \frac{\Delta\tau_{+i} + \Delta\tau_{-i}}{2\Delta B_j}. \tag{G.2}$$

To determine how robust $\mathbf{A}$ is to changes in the AC magnetic bias field amplitude, we apply a 10 Hz, 10.2 μTpp (3.6 μT rms) test field to the diamond and adjust the peak-to-peak AC magnetic bias field amplitude in steps of ≈ 55 μT taking a field measurement at each step. The results are depicted in figure G-1 along with two insets: one illustrating the change

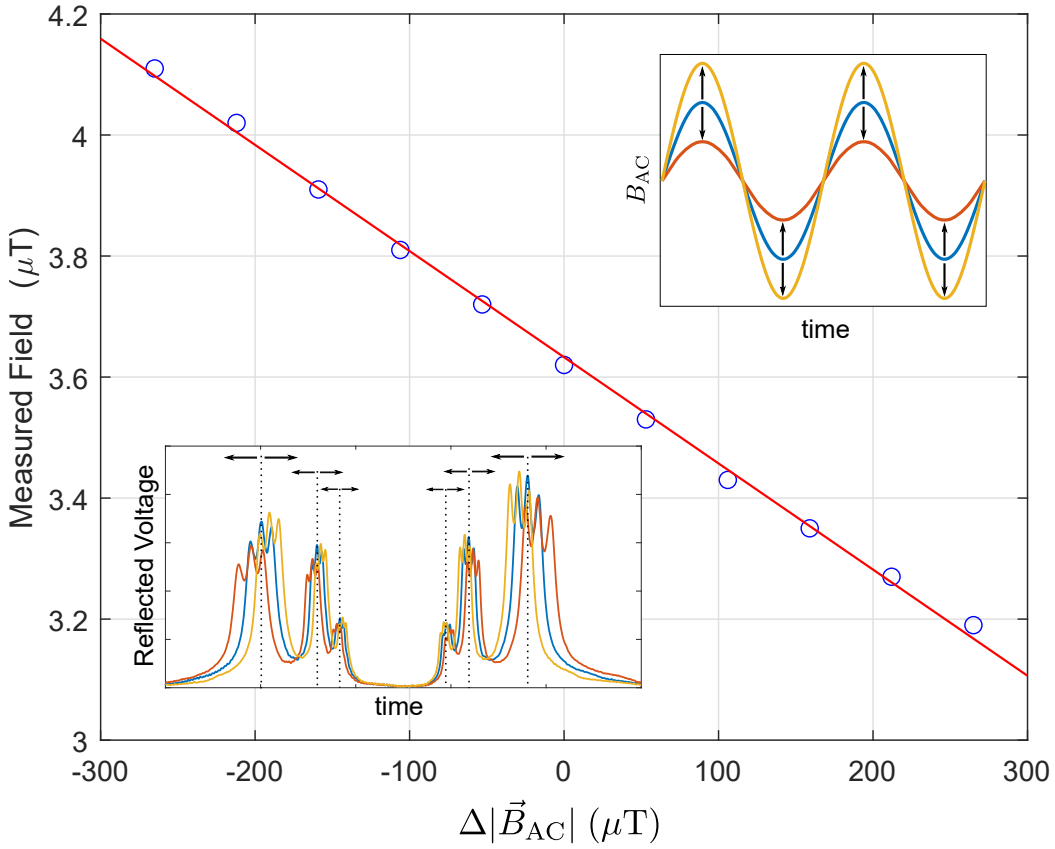

Figure G-1: **Accuracy error bias field drift** Changing the magnetic bias field amplitude $|\vec{B}_{\mathrm{AC}}|$ (inset top right) causes changes in the cavity readout spectrum (inset bottom left). Because the calibration matrix **A** is measured at a specific value of $|\vec{B}_{\mathrm{AC}}|$, changes $\Delta|\vec{B}_{\mathrm{AC}}|$ will cause an error in the magnetometer output. We measure how robust the magnetometer output is by sweeping $\Delta|\vec{B}_{\mathrm{AC}}|$ over a ± 300 μT range, while applying a 10 Hz test field with constant amplitude of 5.1 μT (3.6 μT rms), and recording the magnetometer output.

in the magnetic bias field amplitude, another illustrating how the cavity-enhanced readout spectrum changes as the amplitude is varied. The slope, plotted in red, gives the sensitivity of the magnetometer output to changes in the bias field amplitude (assuming **A** remains static). A 10 μT change in the bias magnetic field amplitude changes the magnetometer output by less than 0.5% (≈ 11 nT) indicating that the magnetometer is robust to changes in the AC magnetic bias field amplitude. Drifts in the NV zero field splitting D, as well as the cavity frequency ω_c, also affect the magnetometer output and are covered in Appendix section G.2.

G.2 Drift suppression scheme

By measuring the both the $|m_s = \pm 1\rangle$ spin states over a half cycle of the AC magnetic bias field, we can introduce a measurement scheme which suppresses errors due to temperature fluctuations of both the cavity and spins. As the system temperature changes, the NV zero field splitting D is modified as $D + \beta_T \Delta T$, where $\beta_T = -74$ kHz/K [40] and ΔT is the change in temperature in Kelvin. Likewise, the resonance frequency of the composite cavity can either increase or decrease depending on material properties and design. For our system we measure the cavity to shift $\approx +3$ kHz/K. The changes in resonance frequencies manifest as differential mode shifts of the peaks of the cavity readout spectrum. Changes in the magnetic field however, manifest as common mode shifts. By adding the peaks corresponding to the $|m_s = \pm 1\rangle$ spin states of each NV orientation, drifts in D and ω_c can be largely suppressed. To determine the degree of suppression, we first operate the magnetometer at 1.5 W of laser power, while applying a 1 μT rms oscillating test field along the z-direction. At the 1s mark (see fig. G-2), we increase the laser power by 1 W (to a total of 2.5 W applied to the diamond) which increases the temperature of the diamond by ≈ 25 K. After 4 s, we return the laser to its original power setting and allow the temperature to return to its equilibrium value. Data are collected for 10 seconds during this process, and capture drifts in the peaks as the laser power is adjusted. Fig. G-2 depicts the response of the $|m_s = \pm 1\rangle$ spin states of NV orientation λ. The peaks drift by ± 0.18 μs as the laser power is increased, which corresponds to an error in the measured DC level of ≈ 0.9 μT in the x-direction, 1.1 μT in the y-direction, and 1.47 μT in the z-direction. By summing the responses, the drifts largely cancel and we measure a peak shift of only 0.002 μs, corresponding to an error of ≈ 10 nT in the x-direction, 12 nT in the y-direction, and 16 nT in the z-direction.

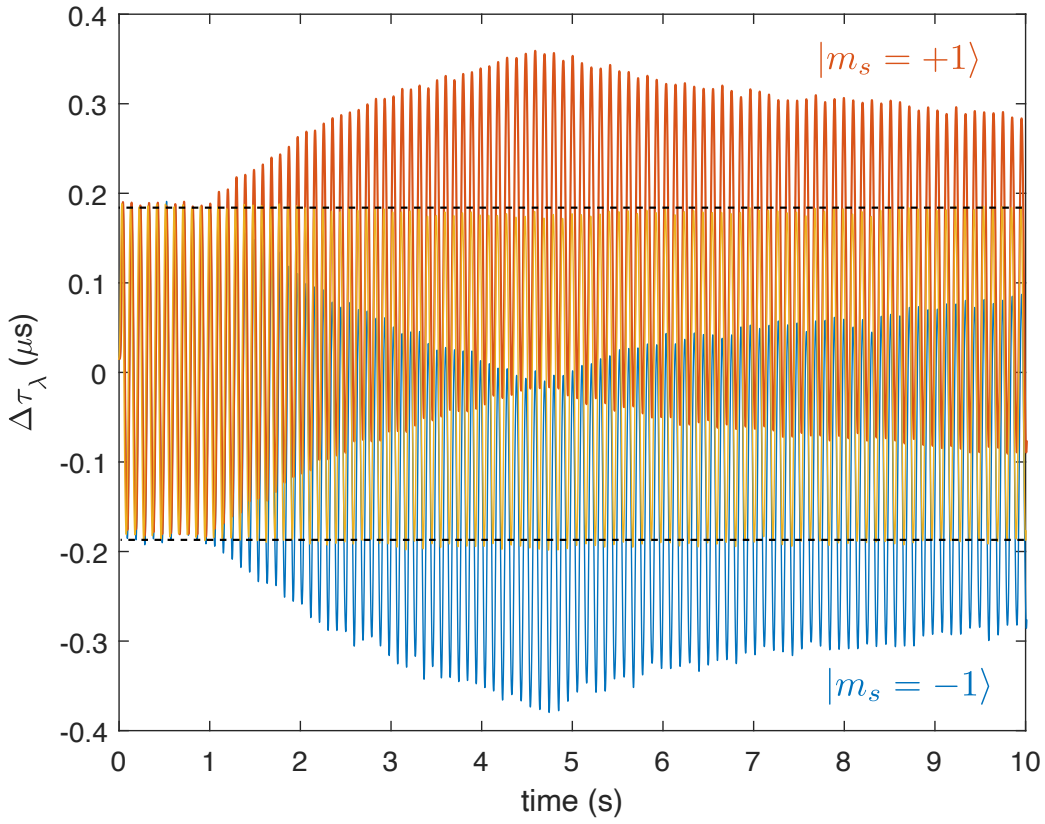

Figure G-2: **Magnetometer drift suppression** Changes in the cavity readout spectrum due to mechanical drifts or temperature are suppressed by adding the peaks of both the $|m_s = \pm 1\rangle$ spin states. We operate the magnetometer over a 10 second period, and induce a change in the diamond temperature by increasing the laser power by 1 W at the 1 second mark. After 4 seconds, we again reduce the laser power back to its initial value. Depicted is the response of the NV_λ orientation $|m_s = +1\rangle$ state (—), $|m_s = -1\rangle$ state (—), and the sum of both $|m_s = \pm 1\rangle$ states (—). By adding the $|m_s = \pm 1\rangle$ states we suppress the drift in the peaks at the 5 second mark from ± 0.18 μs to 0.002 μs.

Appendix H

Orientation dependent spin-photon coupling g_s

Because only the component of the MW field which projects onto the transverse plane of the NV symmetry axis drives Rabi oscillations, the vacuum coupling $g_{s,i}$ will differ between NV orientations. For a MW field aligned perfectly transverse to the NV symmetry axis, the single spin-photon coupling is

$$g_s = \frac{\gamma}{2} B_v^{\mathrm{rms}}(\mathbf{r}), \tag{H.1}$$

where $\gamma \approx 2.8$ MHz/Gauss is the electron gyromagnetic ratio, and B_v^{rms} is the RMS vacuum B-field in the cavity at the spin location $\mathbf{r}$. For a spin at an angle δ relative to the plane, (H) is modified by a multiplicative geometric factor

$$\mathfrak{n} = \vec{u} - ||\vec{u}||\ \vec{n}\cos\delta, \tag{H.2}$$

where $\vec{u}$ is the unit normal vector aligned with the MW polarization, and $\vec{n}$ is the unit normal vector aligned with the NV symmetry axis. In the diamond coordinate system, $\vec{u} = \vec{u_B} = (-0.53, 0.23, 0.82)$ and $\vec{n}_\lambda = (0, \sqrt{2/3}, -\sqrt{1/3})$, $\vec{n}_\phi = (0, -\sqrt{2/3}, -\sqrt{1/3})$, $\vec{n}_\kappa = (-\sqrt{2/3}, 0, \sqrt{1/3})$, $\vec{n}_\chi = (\sqrt{2/3}, 0, \sqrt{1/3})$. Applying (H.2) yields $\mathfrak{n}_\lambda = 0.96$, $\mathfrak{n}_\phi = 0.75$, $\mathfrak{n}_\kappa = 0.43$, and $\mathfrak{n}_\chi = 0.99$. We find good agreement in comparing the ratios of the reflected MW voltage between NV axes in fig. 5-1c and the values computed here. Additional differences

in the reflected MW voltage between axes arise from differences in the number of polarized NVs between orientations due to the linear polarization of the pump laser.

Bibliography

[1] A Abragam. *Principles of Nuclear Magnetism*. Oxford Univ. Press, 1961.

[2] V. M. Acosta, E. Bauch, M. P. Ledbetter, C. Santori, K.-M. C. Fu, P. E. Barclay, R. G. Beausoleil, H. Linget, J. F. Roch, F. Treussart, S. Chemerisov, W. Gawlik, and D. Budker. Diamonds with a high density of nitrogen-vacancy centers for magnetometry applications. *Physical Review B*, 80(11):115202, September 2009.

[3] R. Akhmedzhanov, L. Gushchin, N. Nizov, V. Nizov, D. Sobgayda, I. Zelensky, and P. Hemmer. Microwave-free magnetometry based on cross-relaxation resonances in diamond nitrogen-vacancy centers. *Physical Review A*, 96(1):013806, July 2017.

[4] Scott T. Alsid, John F. Barry, Linh M. Pham, Jennifer M. Schloss, Michael F. O'Keeffe, Paola Cappellaro, and Danielle A. Braje. Photoluminescence decomposition analysis: A technique to characterize N-V creation in diamond. *Physical Review Applied*, 12:044003, Oct 2019.

[5] R. Amsüss, Ch. Koller, T. Nöbauer, S. Putz, S. Rotter, K. Sandner, S. Schneider, M. Schramböck, G. Steinhauser, H. Ritsch, J. Schmiedmayer, and J. Majer. Cavity QED with Magnetically Coupled Collective Spin States. *Physical Review Letters*, 107(6):060502, Aug 2011.

[6] P. Andrich, C. F. de las Casas, X. Liu, H. L. Bretscher, J. R. Berman, F. J. Heremans, P. F. Nealey, and D. D. Awschalom. Long-range spin wave mediated control of defect qubits in nanodiamonds. *npj Quantum Information*, 3:28, July 2017.

[7] Andreas Angerer, Thomas Astner, Daniel Wirtitsch, Hitoshi Sumiya, Shinobu Onoda, Junichi Isoya, Stefan Putz, and Johannes Majer. Collective strong coupling with homogeneous Rabi frequencies using a 3D lumped element microwave resonator. *Applied Physics Letters*, 109(3):033508, Jul 2016.

[8] Andreas Angerer, Stefan Putz, Dmitry O. Krimer, Thomas Astner, Matthias Zens, Ralph Glattauer, Kirill Streltsov, William J. Munro, Kae Nemoto, Stefan Rotter, Jörg Schmiedmayer, and Johannes Majer. Ultralong relaxation times in bistable hybrid quantum systems. *Science Advances*, 3(12):e1701626, Dec 2017.

[9] T. Astner, S. Nevlacsil, N. Peterschofsky, A. Angerer, S. Rotter, S. Putz, J. Schmiedmayer, and J. Majer. Coherent Coupling of Remote Spin Ensembles via a Cavity Bus. *Physical Review Letters*, 118(14):140502, Apr 2017.

[10] Gopalakrishnan Balasubramanian, I. Y. Chan, Roman Kolesov, Mohannad Al-Hmoud, Julia Tisler, Chang Shin, Changdong Kim, Aleksander Wojcik, Philip R. Hemmer, Anke Krueger, Tobias Hanke, Alfred Leitenstorfer, Rudolf Bratschitsch, Fedor Jelezko, and Jörg Wrachtrup. Nanoscale imaging magnetometry with diamond spins under ambient conditions. *Nature*, 455(7213):648–651, Oct 2008.

[11] Gopalakrishnan Balasubramanian, Philipp Neumann, Daniel Twitchen, Matthew Markham, Roman Kolesov, Norikazu Mizuochi, Junichi Isoya, Jocelyn Achard, Johannes Beck, Julia Tissler, et al. Ultralong spin coherence time in isotopically engineered diamond. *Nature materials*, 8(5):383, 2009.

[12] N. Bar-Gill, L. M. Pham, A. Jarmola, D. Budker, and R. L. Walsworth. Solid-state electronic spin coherence time approaching one second. *Nature Communications*, 4:1743, Apr 2013.

[13] B Barrett, A Bertoldi, and P Bouyer. Inertial quantum sensors using light and matter. *Physica Scripta*, 91(5):053006, 2016.

[14] John F Barry, Jennifer M Schloss, Erik Bauch, Matthew J Turner, Connor A Hart, Linh M Pham, and Ronald L Walsworth. Sensitivity optimization for nv-diamond magnetometry. *Reviews of Modern Physics*, 92(1):015004, 2020.

[15] John F Barry, Matthew J Turner, Jennifer M Schloss, David R Glenn, Yuyu Song, Mikhail D Lukin, Hongkun Park, and Ronald L Walsworth. Optical magnetic detection of single-neuron action potentials using quantum defects in diamond. *Proceedings of the National Academy of Sciences*, 113(49):14133–14138, 2016.

[16] Erik Bauch, Connor A. Hart, Jennifer M. Schloss, Matthew J. Turner, John F. Barry, Pauli Kehayias, Swati Singh, and Ronald L. Walsworth. Ultralong Dephasing Times in Solid-State Spin Ensembles via Quantum Control. *Physical Review X*, 8(3):031025, Jul 2018.

[17] Erik Bauch, Swati Singh, Junghyun Lee, Connor A Hart, Jennifer M Schloss, Matthew J Turner, John F Barry, Linh M Pham, Nir Bar-Gill, Susanne F Yelin, et al. Decoherence of ensembles of nitrogen-vacancy centers in diamond. *Physical Review B*, 102(13):134210, 2020.

[18] K. Bayat, J. Choy, M. Farrokh Baroughi, S. Meesala, and M. Loncar. Efficient, Uniform, and Large Area Microwave Magnetic Coupling to NV Centers in Diamond Using Double Split-Ring Resonators. *Nano Letters*, 14:1208–1213, March 2014.

[19] MI Bichurin, VM Petrov, RV Petrov, AS Tatarenko, and A Grosz. High sensitivity magnetometers, smart sensors, measurement and instrumentation, 2016.

[20] Alexandre Blais, Ren-Shou Huang, Andreas Wallraff, S. M. Girvin, and R. J. Schoelkopf. Cavity quantum electrodynamics for superconducting electrical circuits: An architecture for quantum computation. *Physical Review A*, 69(6):062320, Jun 2004.

[21] Felix Bloch. Nuclear induction. *Physical review*, 70(7-8):460, 1946.

[22] BJ Bloom, TL Nicholson, JR Williams, SL Campbell, M Bishof, X Zhang, W Zhang, SL Bromley, and J Ye. An optical lattice clock with accuracy and stability at the 10-18 level. *Nature*, 506(7486):71–75, 2014.

[23] Dolev Bluvstein, Zhiran Zhang, and Ania C. Bleszynski Jayich. Identifying and mitigating charge instabilities in shallow diamond nitrogen-vacancy centers. *Physical Review Letters*, 122:076101, Feb 2019.

[24] T. W. Borneman and D. G. Cory. Bandwidth-limited control and ringdown suppression in high-Q resonators. *Journal of Magnetic Resonance*, 225:120–129, December 2012.

[25] Elena Boto, Niall Holmes, James Leggett, Gillian Roberts, Vishal Shah, Sofie S Meyer, Leonardo Duque Muñoz, Karen J Mullinger, Tim M Tierney, Sven Bestmann, et al. Moving magnetoencephalography towards real-world applications with a wearable system. *Nature*, 555(7698):657–661, 2018.

[26] E. Bourgeois, A. Jarmola, P. Siyushev, M. Gulka, J. Hruby, F. Jelezko, D. Budker, and M. Nesladek. Photoelectric detection of electron spin resonance of nitrogen-vacancy centres in diamond. *Nature Communications*, 6:8577, Oct 2015.

[27] Jonathan D. Breeze, Enrico Salvadori, Juna Sathian, Neil McN. Alford, and Christopher W. M. Kay. Room-temperature cavity quantum electrodynamics with strongly coupled dicke states. *npj Quantum Information*, 3(1):40, 2017.

[28] Jonathan D. Breeze, Enrico Salvadori, Juna Sathian, Neil Mcn. Alford, and Christopher W. M. Kay. Continuous-wave room-temperature diamond maser. *Nature*, 555(7697):493–496, Mar 2018.

[29] Dmitry Budker and Michael Romalis. Optical magnetometry. *Nature physics*, 3(4):227–234, 2007.

[30] Stefania Castelletto and Alberto Boretti. Silicon carbide color centers for quantum applications. *Journal of Physics: Photonics*, 2(2):022001, mar 2020.

[31] Georgios Chatzidrosos, Arne Wickenbrock, Lykourgos Bougas, Nathan Leefer, Teng Wu, Kasper Jensen, Yannick Dumeige, and Dmitry Budker. Miniature cavity-enhanced diamond magnetometer. *Physical Review Applied*, 8:044019, Oct 2017.

[32] Edward H. Chen, Hannah A. Clevenson, Kerry A. Johnson, Linh M. Pham, Dirk R. Englund, Philip R. Hemmer, and Danielle A. Braje. High-sensitivity spin-based electrometry with an ensemble of nitrogen-vacancy centers in diamond. *Physical Review A*, 95:053417, May 2017.

[33] Lilian Isabel Childress. *Coherent manipulation of single quantum systems in the solid state*. PhD thesis, Harvard University, March 2007.

[34] M. Chipaux, A. Tallaire, J. Achard, S. Pezzagna, J. Meijer, V. Jacques, J.-F. Roch, and T. Debuisschert. Magnetic imaging with an ensemble of nitrogen vacancy-centers in diamond. *European Physical Journal D*, 69:166, July 2015.

[35] Hyeongrak Choi and Dirk Englund. Ultrastrong magnetic light-matter interaction with cavity mode engineering. *arXiv preprint arXiv:2108.13266*, 2021.

[36] A Chwala, J Kingman, R Stolz, M Schmelz, V Zakosarenko, S Linzen, F Bauer, M Starkloff, M Meyer, and HG Meyer. Noise characterization of highly sensitive squid magnetometer systems in unshielded environments. *Superconductor Science and Technology*, 26(3):035017, 2013.

[37] Valeria Cimini, Marta Mellini, Giordano Rampioni, Marco Sbroscia, Livia Leoni, Marco Barbieri, and Ilaria Gianani. Adaptive tracking of enzymatic reactions with quantum light. *Optics Express*, 27(24):35245–35256, 2019.

[38] A. A. Clerk, M. H. Devoret, S. M. Girvin, Florian Marquardt, and R. J. Schoelkopf. Introduction to quantum noise, measurement, and amplification. *Reviews of Modern Physics*, 82(2):1155–1208, Apr 2010.

[39] Hannah Clevenson, Linh M. Pham, Carson Teale, Kerry Johnson, Dirk Englund, and Danielle Braje. Robust high-dynamic-range vector magnetometry with nitrogen-vacancy centers in diamond. *Applied Physics Letters*, 112(25):252406, Jun 2018.

[40] Hannah Clevenson, Matthew E. Trusheim, Carson Teale, Tim Schröder, Danielle Braje, and Dirk Englund. Broadband magnetometry and temperature sensing with a light-trapping diamond waveguide. *Nature Physics*, 11(5):393–397, May 2015.

[41] Corey J Cochrane, Jordana Blacksberg, Mark A Anders, and Patrick M Lenahan. Vectorized magnetometer for space applications using electrical readout of atomic scale defects in silicon carbide. *Scientific reports*, 6(1):1–13, 2016.

[42] Yves Colombe, Tilo Steinmetz, Guilhem Dubois, Felix Linke, David Hunger, and Jakob Reichel. Strong atom-field coupling for Bose-Einstein condensates in an optical cavity on a chip. *Nature*, 450(7167):272–276, Nov 2007.

[43] Scott E Crawford, Roman A Shugayev, Hari P Paudel, Ping Lu, Madhava Syamlal, Paul R Ohodnicki, Benjamin Chorpening, Randall Gentry, and Yuhua Duan. Quantum sensing for energy applications: Review and perspective. *Advanced Quantum Technologies*, 4(8):2100049, 2021.

[44] D. L. Creedon, J.-M. Le Floch, M. Goryachev, W. G. Farr, S. Castelletto, and M. E. Tobar. Strong coupling between P 1 diamond impurity centers and a three-dimensional lumped photonic microwave cavity. *Physical Review B*, 91(14):140408, April 2015.

[45] Conner Dailey, Colin Bradley, Derek F Jackson Kimball, Ibrahim A Sulai, Szymon Pustelny, Arne Wickenbrock, and Andrei Derevianko. Quantum sensor networks as exotic field telescopes for multi-messenger astronomy. *Nature Astronomy*, 5(2):150–158, 2021.

[46] Hunter C. Davis, Pradeep Ramesh, Aadyot Bhatnagar, Audrey Lee-Gosselin, John F. Barry, David R. Glenn, Ronald L. Walsworth, and Mikhail G. Shapiro. Mapping the microscale origins of magnetic resonance image contrast with subcellular diamond magnetometry. *Nature Communications*, 9:131, Jan 2018.

[47] Christian L Degen, F Reinhard, and Paola Cappellaro. Quantum sensing. *Reviews of Modern Physics*, 89(3):035002, 2017.

[48] R. H. Dicke. Coherence in spontaneous radiation processes. *Physical Review*, 93:99–110, Jan 1954.

[49] I. Diniz, S. Portolan, R. Ferreira, J. M. Gérard, P. Bertet, and A. Auffèves. Strongly coupling a cavity to inhomogeneous ensembles of emitters: Potential for long-lived solid-state quantum memories. *Physical Review A*, 84(6):063810, Dec 2011.

[50] Marcus W Doherty, Neil B Manson, Paul Delaney, Fedor Jelezko, Jörg Wrachtrup, and Lloyd CL Hollenberg. The nitrogen-vacancy colour centre in diamond. *Physics Reports*, 528(1):1–45, 2013.

[51] F. Dolde, H. Fedder, M. W. Doherty, T. Nöbauer, F. Rempp, G. Balasubramanian, T. Wolf, F. Reinhard, L. C. L. Hollenberg, F. Jelezko, and J. Wrachtrup. Electric-field sensing using single diamond spins. *Nature Physics*, 7(6):459–463, Jun 2011.

[52] Gareth R. Eaton, Sandra S. Eaton, David P. Barr, and Ralph T. Weber. *Quantitative EPR*. Springer-Verlag Wien, 2010.

[53] J Ebel, T Joas, M Schalk, P Weinbrenner, A Angerer, J Majer, and F Reinhard. Dispersive readout of room-temperature ensemble spin sensors. *Quantum Science and Technology*, 6(3):03LT01, 2021.

[54] ER Eisenach, JF Barry, LM Pham, RG Rojas, Dirk R Englund, and DA Braje. Broadband loop gap resonator for nitrogen vacancy centers in diamond. *Review of Scientific Instruments*, 89(9):094705, 2018.

[55] Erik R Eisenach, John F Barry, Michael F O'Keeffe, Jennifer M Schloss, Matthew H Steinecker, Dirk R Englund, and Danielle A Braje. Cavity-enhanced microwave readout of a solid-state spin sensor. *Nature communications*, 12(1):1–7, 2021.

[56] Abram L Falk, Bob B Buckley, Greg Calusine, William F Koehl, Viatcheslav V Dobrovitski, Alberto Politi, Christian A Zorman, Philip X-L Feng, and David D Awschalom. Polytype control of spin qubits in silicon carbide. *Nature Communications*, 4(1):1–7, 2013.

[57] S. Felton, A. M. Edmonds, M. E. Newton, P. M. Martineau, D. Fisher, D. J. Twitchen, and J. M. Baker. Hyperfine interaction in the ground state of the negatively charged nitrogen vacancy center in diamond. *Physical Review B*, 79:075203, Feb 2009.

[58] Ilja Fescenko, Andrey Jarmola, Igor Savukov, Pauli Kehayias, Janis Smits, Joshua Damron, Nathaniel Ristoff, Nazanin Mosavian, and Victor M. Acosta. Diamond magnetometer enhanced by ferrite flux concentrators. *Physical Review Research*, 2:023394, Jun 2020.

[59] Graeme Flower, Maxim Goryachev, Jeremy Bourhill, and Michael E. Tobar. Experimental implementations of cavity-magnon systems: from ultra strong coupling to applications in precision measurement. *New Journal of Physics*, 21(9):095004, Sep 2019.

[60] W. Froncisz and J. S. Hyde. The loop-gap resonator: a new microwave lumped circuit ESR sample structure. *Journal of Magnetic Resonance*, 47:515–521, 1982.

[61] Roger R Fu, Benjamin P Weiss, Eduardo A Lima, Richard J Harrison, Xue-Ning Bai, Steven J Desch, Denton S Ebel, Clément Suavet, Huapei Wang, David Glenn, et al. Solar nebula magnetic fields recorded in the semarkona meteorite. *Science*, 346(6213):1089–1092, 2014.

[62] C. W. Gardiner and M. J. Collett. Input and output in damped quantum systems: Quantum stochastic differential equations and the master equation. *Physical Review A*, 31(6):3761–3774, Jun 1985.

[63] DT Germain-Jones. Post-war developments in geophysical instrumentation for oil prospecting. *Journal of Scientific Instruments*, 34(1):1, 1957.

[64] A. Ghirri, C. Bonizzoni, F. Troiani, N. Buccheri, L. Beverina, A. Cassinese, and M. Affronte. Coherently coupling distinct spin ensembles through a high-T_c superconducting resonator. *Physical Review A*, 93(6):063855, Jun 2016.

[65] Steven M Girvin. Circuit qed: superconducting qubits coupled to microwave photons. *Quantum Machines: Measurement and Control of Engineered Quantum Systems*, 113:2, 2011.

[66] D. R. Glenn, R. R. Fu, P. Kehayias, D. Le Sage, E. A. Lima, B. P. Weiss, and R. L. Walsworth. Micrometer-scale magnetic imaging of geological samples using a quantum diamond microscope. *Geochemistry, Geophysics, Geosystems*, 18(8):3254–3267, Aug 2017.

[67] David R Glenn, Kyungheon Lee, Hongkun Park, Ralph Weissleder, Amir Yacoby, Mikhail D Lukin, Hakho Lee, Ronald L Walsworth, and Colin B Connolly. Single-cell magnetic imaging using a quantum diamond microscope. *Nature methods*, 12(8):736–738, 2015.

[68] Matti Hämäläinen, Riitta Hari, Risto J Ilmoniemi, Jukka Knuutila, and Olli V Lounasmaa. Magnetoencephalography—theory, instrumentation, and applications to noninvasive studies of the working human brain. *Reviews of Modern Physics*, 65(2):413, 1993.

[69] J. G. Hartnett, M. E. Tobar, E. N. Ivanov, and J. Krupka. Room temperature measurement of the anisotropic loss tangent of sapphire using the whispering gallery mode technique. *IEEE Transactions on Ultrasonics, Ferroelectrics, and Frequency Control*, 53(1):34–38, Jan 2006.

[70] Jonathan S Hodges, Norman Ying Yao, Dougal Maclaurin, C Rastogi, Mikhail D Lukin, and D Englund. Timekeeping with electron spin states in diamond. *Physical Review A*, 87(3):032118, 2013.

[71] David A. Hopper, Richard R. Grote, Annemarie L. Exarhos, and Lee C. Bassett. Near-infrared-assisted charge control and spin readout of the nitrogen-vacancy center in diamond. *Physical Review B*, 94:241201, Dec 2016.

[72] V. R. Horowitz, B. J. Alemán, D. J. Christle, A. N. Cleland, and D. D. Awschalom. Electron spin resonance of nitrogen-vacancy centers in optically trapped nanodiamonds. *Proceedings of the National Academy of Science*, 109:13493–13497, August 2012.

[73] A. Horsley, P. Appel, J. Wolters, J. Achard, A. Tallaire, P. Maletinsky, and P. Treutlein. Microwave device characterisation using a widefield diamond microscope. *ArXiv e-prints*, February 2018.

[74] Andrew Horsley and Philipp Treutlein. Frequency-tunable microwave field detection in an atomic vapor cell. *Applied Physics Letters*, 108(21):211102, 2016.

[75] Hans Huebl, Christoph W. Zollitsch, Johannes Lotze, Fredrik Hocke, Moritz Greifenstein, Achim Marx, Rudolf Gross, and Sebastian T. B. Goennenwein. High Cooperativity in Coupled Microwave Resonator Ferrimagnetic Insulator Hybrids. *Physical Review Letters*, 111(12):127003, Sep 2013.

[76] Atac Imamoğlu. Cavity QED Based on Collective Magnetic Dipole Coupling: Spin Ensembles as Hybrid Two-Level Systems. *Physical Review Letters*, 102(8):083602, Feb 2009.

[77] J. C. Jaskula, B. J. Shields, E. Bauch, M. D. Lukin, A. S. Trifonov, and R. L. Walsworth. Improved Quantum Sensing with a Single Solid-State Spin via Spin-to-Charge Conversion. *Physical Review Applied*, 11(6):064003, Jun 2019.

[78] F. Jelezko, T. Gaebel, I. Popa, A. Gruber, and J. Wrachtrup. Observation of Coherent Oscillations in a Single Electron Spin. *Physical Review Letters*, 92(7):076401, February 2004.

[79] Kasper Jensen, Pauli Kehayias, and Dmitry Budker. Magnetometry with Nitrogen-Vacancy Centers in Diamond. In *High Sensitivity Magnetometers*, pages 553–576. Springer, 2017.

[80] Wenfei Jia, Zhifu Shi, Xi Qin, Xing Rong, and Jiangfeng Du. Ultra-broadband coplanar waveguide for optically detected magnetic resonance of nitrogen-vacancy centers in diamond. *Review of Scientific Instruments*, 89(6):064705, 2018.

[81] L. Jiang, J. S. Hodges, J. R. Maze, P. Maurer, J. M. Taylor, D. G. Cory, P. R. Hemmer, R. L. Walsworth, A. Yacoby, A. S. Zibrov, and M. D. Lukin. Repetitive readout of a single electronic spin via quantum logic with nuclear spin ancillae. *Science*, 326(5950):267–272, 2009.

[82] Darko Kajfez and Pierre Guillon, editors. *Dielectric resonators*. Artech House Microwave Library. Artech House, Dedham, Mass., 1986.

[83] P. Kapitanova, V. Soshenko, V. Vorobyov, D. Dobrykh, S. Bolshedvorskiih, V. Sorokin, and A. Akimov. Dielectric resonator antenna for coupling to NV centers in diamond. In *American Institute of Physics Conference Series*, volume 1874 of *American Institute of Physics Conference Series*, page 030017, September 2017.

[84] S. Karaveli, O. Gaathon, A. Wolcott, R. Sakakibara, O. A. Shemesh, D. S. Peterka, E. S. Boyden, J. S. Owen, R. Yuste, and D. Englund. Modulation of nitrogen vacancy charge state and fluorescence in nanodiamonds using electrochemical potential. *Proceedings of the National Academy of Science*, 113:3938–3943, April 2016.

[85] Donggyu Kim, Mohamed I Ibrahim, Christopher Foy, Matthew E Trusheim, Ruonan Han, and Dirk R Englund. A cmos-integrated quantum sensor based on nitrogen–vacancy centres. *Nature Electronics*, 2(7):284–289, 2019.

[86] JR Kirtley, MB Ketchen, KG Stawiasz, JZ Sun, WJ Gallagher, SH Blanton, and SJ Wind. High-resolution scanning squid microscope. *Applied Physics Letters*, 66(9):1138–1140, 1995.

[87] Anton Frisk Kockum, Adam Miranowicz, Simone De Liberato, Salvatore Savasta, and Franco Nori. Ultrastrong coupling between light and matter. *Nature Reviews Physics*, 1(1):19–40, 2019.

[88] IK Kominis, TW Kornack, JC Allred, and Michael V Romalis. A subfemtotesla multichannel atomic magnetometer. *Nature*, 422(6932):596–599, 2003.

[89] M. F. Koskinen and K. R. Metz. The concentric loop-gap resonator—A compact, broadly tunable design for NMR applications. *Journal of Magnetic Resonance*, 98:576–588, 1992.

[90] Dmitry O. Krimer, Stefan Putz, Johannes Majer, and Stefan Rotter. Non-Markovian dynamics of a single-mode cavity strongly coupled to an inhomogeneously broadened spin ensemble. *Physical Review A*, 90(4):043852, Oct 2014.

[91] Y. Kubo, F. R. Ong, P. Bertet, D. Vion, V. Jacques, D. Zheng, A. Dréau, J. F. Roch, A. Auffeves, F. Jelezko, J. Wrachtrup, M. F. Barthe, P. Bergonzo, and D. Esteve. Strong Coupling of a Spin Ensemble to a Superconducting Resonator. *Physical Review Letters*, 105(14):140502, Oct 2010.

[92] G. Kucsko, P. C. Maurer, N. Y. Yao, M. Kubo, H. J. Noh, P. K. Lo, H. Park, and M. D. Lukin. Nanometre-scale thermometry in a living cell. *Nature*, 500(7460):54–58, Aug 2013.

[93] Akihiro Kuwahata, Takahiro Kitaizumi, Kota Saichi, Takumi Sato, Ryuji Igarashi, Takeshi Ohshima, Yuta Masuyama, Takayuki Iwasaki, Mutsuko Hatano, Fedor Jelezko, et al. Magnetometer with nitrogen-vacancy center in a bulk diamond for detecting magnetic nanoparticles in biomedical applications. *Scientific reports*, 10(1):1–9, 2020.

[94] J.-M. Le Floch, C. Bradac, N. Nand, S. Castelletto, M. E. Tobar, and T. Volz. Addressing a single spin in diamond with a macroscopic dielectric microwave cavity. *Applied Physics Letters*, 105(13):133101, September 2014.

[95] J. M. Le Floch, N. Delhote, M. Aubourg, V. Madrangeas, D. Cros, S. Castelletto, and M. E. Tobar. Towards achieving strong coupling in three-dimensional-cavity with solid state spin resonance. *Journal of Applied Physics*, 119(15):153901, Apr 2016.

[96] D. Le Sage, K. Arai, D. R. Glenn, S. J. Devience, L. M. Pham, L. Rahn-Lee, M. D. Lukin, A. Yacoby, A. Komeili, and R. L. Walsworth. Optical magnetic imaging of living cells. *Nature*, 496(7446):486–489, Apr 2013.

[97] Sang-Yun Lee, Matthias Niethammer, and Jörg Wrachtrup. Vector magnetometry based on s= 3 2 electronic spins. *Physical Review B*, 92(11):115201, 2015.

[98] James Lenz and S Edelstein. Magnetic sensors and their applications. *IEEE Sensors Journal*, 6(3):631–649, 2006.

[99] James E Lenz. A review of magnetic sensors. *Proceedings of the IEEE*, 78(6):973–989, 1990.

[100] Yan Xia Liu, Xi Sheng Li, Xiao Juan Zhang, and Yi Bo Feng. Novel calibration algorithm for a three-axis strapdown magnetometer. *Sensors*, 14(5):8485–8504, 2014.

[101] J H N Loubser and J A van Wyk. Electron spin resonance in the study of diamond. *Reports on Progress in Physics*, 41(8):1201–1248, aug 1978.

[102] I. Lovchinsky, A. O. Sushkov, E. Urbach, N. P. de Leon, S. Choi, K. De Greve, R. Evans, R. Gertner, E. Bersin, C. Müller, L. McGuinness, F. Jelezko, R. L. Walsworth, H. Park, and M. D. Lukin. Nuclear magnetic resonance detection and spectroscopy of single proteins using quantum logic. *Science*, 351(6275):836–841, 2016.

[103] BJ Maertz, AP Wijnheijmer, GD Fuchs, ME Nowakowski, and DD Awschalom. Vector magnetic field microscopy using nitrogen vacancy centers in diamond. *Applied Physics Letters*, 96(9):092504, 2010.

[104] Mason C Marshall, Matthew J Turner, Mark JH Ku, David F Phillips, and Ronald L Walsworth. Directional detection of dark matter with diamond. *Quantum Science and Technology*, 6(2):024011, 2021.

[105] J. R. Maze, A. Gali, E. Togan, Y. Chu, A. Trifonov, E. Kaxiras, and M. D. Lukin. Properties of nitrogen-vacancy centers in diamond: the group theoretic approach. *New Journal of Physics*, 13(2):025025, February 2011.

[106] J. Maze Rios. *Quantum manipulation of nitrogen-vacancy centers in diamond: From basic properties to applications*. PhD thesis, Harvard University, 2010.

[107] Julia Michl, Jakob Steiner, Andrej Denisenko, André Bülau, André Zimmermann, Kazuo Nakamura, Hitoshi Sumiya, Shinobu Onoda, Philipp Neumann, Junichi Isoya, and Jörg Wrachtrup. Robust and Accurate Electric Field Sensing with Solid State Spin Ensembles. *Nano Letters*, 19(8):4904–4910, Aug 2019.

[108] N. Mizuochi, S. Yamasaki, H. Takizawa, N. Morishita, T. Ohshima, H. Itoh, and J. Isoya. Continuous-wave and pulsed epr study of the negatively charged silicon vacancy with $s = \frac{3}{2}$ and C_{3v} symmetry in n-type $4\mathrm{H} - \mathrm{SiC}$. *Physical Review B*, 66:235202, Dec 2002.

[109] C. J. Montgomery, R. H. Dicke, and E. M. Purcell. *MIT Radiation Laboratory Series: Principles of Microwave Circuits*, volume 8. McGraw-Hill, 1948.

[110] S Morales, MC Corsi, W Fourcault, F Bertrand, G Cauffet, C Gobbo, F Alcouffe, F Lenouvel, M Le Prado, F Berger, et al. Magnetocardiography measurements with 4he vector optically pumped magnetometers at room temperature. *Physics in Medicine & Biology*, 62(18):7267, 2017.

[111] M. Mrózek, J. Mlynarczyk, D. S. Rudnicki, and W. Gawlik. Circularly polarized microwaves for magnetic resonance study in the GHz range: Application to nitrogen-vacancy in diamonds. *Applied Physics Letters*, 107(1):013505, July 2015.

[112] Philipp Neumann, Johannes Beck, Matthias Steiner, Florian Rempp, Helmut Fedder, Philip R. Hemmer, Jörg Wrachtrup, and Fedor Jelezko. Single-shot readout of a single nuclear spin. *Science*, 329(5991):542–544, 2010.

[113] Philipp Neumann, Ingmar Jakobi, Florian Dolde, Christian Burk, Rolf Reuter, Gerald Waldherr, Jan Honert, Thomas Wolf, Andreas Brunner, Jeong Hyun Shim, et al. High-precision nanoscale temperature sensing using single defects in diamond. *Nano letters*, 13(6):2738–2742, 2013.

[114] Travis L Nicholson, SL Campbell, RB Hutson, G Edward Marti, BJ Bloom, Rees L McNally, Wei Zhang, MD Barrett, Marianna S Safronova, GF Strouse, et al. Systematic evaluation of an atomic clock at 2× 10- 18 total uncertainty. *Nature Communications*, 6(1):1–8, 2015.

[115] Matthias Niethammer, Matthias Widmann, Sang-Yun Lee, Pontus Stenberg, Olof Kordina, Takeshi Ohshima, Nguyen Tien Son, Erik Janzén, and Jörg Wrachtrup. Vector magnetometry using silicon vacancies in 4 h-sic under ambient conditions. *Physical Review Applied*, 6(3):034001, 2016.

[116] Yushi Nishimura, Keisuke Oshimi, Yumi Umehara, Yuka Kumon, Kazu Miyaji, Hiroshi Yukawa, Yutaka Shikano, Tsutomu Matsubara, Masazumi Fujiwara, Yoshinobu Baba, and Yoshio Teki. Wide-field fluorescent nanodiamond spin measurements toward real-time large-area intracellular thermometry. *Sci. Rep.*, 11(1):4248, Feb 2021.

[117] A. S. Peshkovsky, J. Forguez, L. Cerioni, and D. J. Pusiol. RF probe recovery time reduction with a novel active ringing suppression circuit. *Journal of Magnetic Resonance*, 177:67–73, November 2005.

[118] S. Pfenninger, W. Froncisz, J. Forrer, J. Luglio, and J. S. Hyde. General method for adjusting the quality factor of EPR resonators. *Review of Scientific Instruments*, 66:4857–4865, October 1995.

[119] L. M. Pham. *Magnetic field sensing with nitrogen-vacancy color centers in diamond*. PhD thesis, Harvard University, 2013.

[120] W. Piasecki and W. Froncisz. Field distributions in loop-gap resonators. *Measurement Science and Technology*, 4:1363–1369, December 1993.

[121] Stefano Pirandola, B Roy Bardhan, Tobias Gehring, Christian Weedbrook, and Seth Lloyd. Advances in photonic quantum sensing. *Nature Photonics*, 12(12):724–733, 2018.

[122] Charles P. Poole. *Electron Spin Resonance: A Comprehensive Treatise on Experimental Techniques*. Interscience Publishers, New York, 1967.

[123] David M Pozar. *Microwave engineering*. John Wiley & Sons, 2009.

[124] S. Probst, H. Rotzinger, S. Wünsch, P. Jung, M. Jerger, M. Siegel, A. V. Ustinov, and P. A. Bushev. Anisotropic Rare-Earth Spin Ensemble Strongly Coupled to a Superconducting Resonator. *Physical Review Letters*, 110(15):157001, Apr 2013.

[125] Nakib Haider Protik, Ankita Katre, Lucas Lindsay, Jesus Carrete, Natalio Mingo, and David Broido. Phonon thermal transport in 2h, 4h and 6h silicon carbide from first principles. *Materials Today Physics*, 1:31–38, 2017.

[126] S. Putz, D. O. Krimer, R. Amsüss, A. Valookaran, T. Nöbauer, J. Schmiedmayer, S. Rotter, and J. Majer. Protecting a spin ensemble against decoherence in the strong-coupling regime of cavity QED. *Nature Physics*, 10(10):720–724, Oct 2014.

[127] Xin Qian, Puqing Jiang, and Ronggui Yang. Anisotropic thermal conductivity of 4h and 6h silicon carbide measured using time-domain thermoreflectance. *Materials Today Physics*, 3:70–75, 2017.

[128] Troy C Richards and Carmen E Lucas. A robust calibration and alignment procedure for collocated magnetometer and accelerometer sensors, 2015.

[129] George A. Rinard and Gareth R. Eaton. *Loop-Gap Resonators*. Kluwer Academic/-Plenum Publishers, 2005.

[130] Gian Luca Romani, Samuel J Williamson, and Lloyd Kaufman. Biomagnetic instrumentation. *Review of Scientific Instruments*, 53(12):1815–1845, 1982.

[131] L. Rondin, J.-P. Tetienne, T. Hingant, J.-F. Roch, P. Maletinsky, and V. Jacques. Magnetometry with nitrogen-vacancy defects in diamond. *Reports on Progress in Physics*, 77(5):056503, May 2014.

[132] B. C. Rose, A. M. Tyryshkin, H. Riemann, N. V. Abrosimov, P. Becker, H.-J. Pohl, M. L. W. Thewalt, K. M. Itoh, and S. A. Lyon. Coherent Rabi Dynamics of a Superradiant Spin Ensemble in a Microwave Cavity. *Physical Review X*, 7(3):031002, July 2017.

[133] TH Sander, J Preusser, R Mhaskar, J Kitching, L Trahms, and S Knappe. Magnetoencephalography with a chip-scale atomic magnetometer. *Biomedical optics express*, 3(5):981–990, 2012.

[134] Kento Sasaki, Yasuaki Monnai, Soya Saijo, Ryushiro Fujita, Hideyuki Watanabe, Junko Ishi-Hayase, Kohei M Itoh, and Eisuke Abe. Broadband, large-area microwave antenna for optically detected magnetic resonance of nitrogen-vacancy centers in diamond. *Review of Scientific Instruments*, 87(5):053904, 2016.

[135] R. Schirhagl, K. Chang, M. Loretz, and C. L. Degen. Nitrogen-Vacancy Centers in Diamond: Nanoscale Sensors for Physics and Biology. *Annual Review of Physical Chemistry*, 65:83–105, April 2014.

[136] Jennifer M. Schloss, John F. Barry, Matthew J. Turner, and Ronald L. Walsworth. Simultaneous Broadband Vector Magnetometry Using Solid-State Spins. *Physical Review Applied*, 10(3):034044, Sep 2018.

[137] D. I. Schuster, Lev S. Bishop, I. L. Chuang, D. DeMille, and R. J. Schoelkopf. Cavity QED in a molecular ion trap. *Physical Review A*, 83(1):012311, Jan 2011.

[138] D. I. Schuster, A. P. Sears, E. Ginossar, L. Dicarlo, L. Frunzio, J. J. L. Morton, H. Wu, G. A. D. Briggs, B. B. Buckley, D. D. Awschalom, and R. J. Schoelkopf. High-Cooperativity Coupling of Electron-Spin Ensembles to Superconducting Cavities. *Physical Review Letters*, 105(14):140501, Oct 2010.

[139] Peter DD Schwindt, Svenja Knappe, Vishal Shah, Leo Hollberg, John Kitching, Li-Anne Liew, and John Moreland. Chip-scale atomic magnetometer. *Applied Physics Letters*, 85(26):6409–6411, 2004.

[140] Arie Sheinker, Lev Frumkis, Boris Ginzburg, Nizan Salomonski, and Ben-Zion Kaplan. Magnetic anomaly detection using a three-axis magnetometer. *IEEE Transactions on Magnetics*, 45(1):160–167, 2009.

[141] Dehong Sheng, S Li, Nezih Dural, and Michael V Romalis. Subfemtotesla scalar atomic magnetometry using multipass cells. *Physical Review Letters*, 110(16):160802, 2013.

[142] B. J. Shields, Q. P. Unterreithmeier, N. P. de Leon, H. Park, and M. D. Lukin. Efficient readout of a single spin state in diamond via spin-to-charge conversion. *Physical Review Letters*, 114(13):136402, 03 2015.

[143] David A. Simpson, Robert G. Ryan, Liam T. Hall, Evgeniy Panchenko, Simon C. Drew, Steven Petrou, Paul S. Donnelly, Paul Mulvaney, and Lloyd C. L. Hollenberg. Electron paramagnetic resonance microscopy using spins in diamond under ambient conditions. *Nature Communications*, 8(1):458, 2017.

[144] David A. Simpson, Jean-Philippe Tetienne, Julia M. McCoey, Kumaravelu Ganesan, Liam T. Hall, Steven Petrou, Robert E. Scholten, and Lloyd C. L. Hollenberg. Magneto-optical imaging of thin magnetic films using spins in diamond. *Scientific Reports*, 6:22797, Mar 2016.

[145] Howard Singer, Lorne Matheson, Richard Grubb, Ann Newman, and David Bouwer. Monitoring space weather with the goes magnetometers. In *GOES-8 and Beyond*, volume 2812, pages 299–308. International Society for Optics and Photonics, 1996.

[146] Petr Siyushev, Milos Nesladek, Emilie Bourgeois, Michal Gulka, Jaroslav Hruby, Takashi Yamamoto, Michael Trupke, Tokuyuki Teraji, Junichi Isoya, and Fedor Jelezko. Photoelectrical imaging and coherent spin-state readout of single nitrogen-vacancy centers in diamond. *Science*, 363(6428):728–731, 2019.

[147] C.P. Slichter. *Principles of Magnetic Resonance*. Springer Series in Solid-State Sciences. Springer Berlin Heidelberg, 1996.

[148] B. Smeltzer, J. McIntyre, and L. Childress. Robust control of individual nuclear spins in diamond. *Physical Review A*, 80(5):050302, November 2009.

[149] M. Steiner, P. Neumann, J. Beck, F. Jelezko, and J. Wrachtrup. Universal enhancement of the optical readout fidelity of single electron spins at nitrogen-vacancy centers in diamond. *Physical Review B*, 81:035205, Jan 2010.

[150] Felix M Stuerner, Andreas Brenneis, Julian Kassel, Uwe Wostradowski, Robert Roelver, Tino Fuchs, Kazuo Nakamura, Hitoshi Sumiya, Shinobu Onoda, Junichi Isoya, et al. Compact integrated magnetometer based on nitrogen-vacancy centres in diamond. *Diamond and Related Materials*, 93:59–65, 2019.

[151] Felix M Stürner, Andreas Brenneis, Julian Kassel, Uwe Wostradowski, Robert Roelver, Tino Fuchs, Kazuo Nakamura, Hitoshi Sumiya, Shinobu Onoda, Junichi Isoya, et al. Compact integrated magnetometer based on nitrogen-vacancy centres in diamond. *Diamond and Related Materials*, 93:59–65, 2019.

[152] Y. Tabuchi, M. Negoro, K. Takeda, and M. Kitagawa. Total compensation of pulse transients inside a resonator. *Journal of Magnetic Resonance*, 204:327–332, June 2010.

[153] Yutaka Tabuchi, Seiichiro Ishino, Toyofumi Ishikawa, Rekishu Yamazaki, Koji Usami, and Yasunobu Nakamura. Hybridizing Ferromagnetic Magnons and Microwave Photons in the Quantum Limit. *Physical Review Letters*, 113(8):083603, Aug 2014.

[154] Haruka Tanji-Suzuki, Ian D. Leroux, Monika H. Schleier-Smith, Marko Cetina, Andrew T. Grier, Jonathan Simon, and Vladan Vuletić. Interaction between Atomic Ensembles and Optical Resonators. *Advances in Atomic Molecular and Optical Physics*, 60:201–237, Jan 2011.

[155] Michael Tavis and Frederick W Cummings. Exact solution for an n-molecule—radiation-field hamiltonian. *Physical Review*, 170(2):379, 1968.

[156] JM Taylor, Paola Cappellaro, L Childress, Liang Jiang, Dmitry Budker, PR Hemmer, Amir Yacoby, R Walsworth, and MD Lukin. High-sensitivity diamond magnetometer with nanoscale resolution. *Nature Physics*, 4(10):810–816, 2008.

[157] Jean-Philippe Tetienne, Nikolai Dontschuk, David A Broadway, Alastair Stacey, David A Simpson, and Lloyd CL Hollenberg. Quantum imaging of current flow in graphene. *Science advances*, 3(4):e1602429, 2017.

[158] Mark Tseitlin, Richard W. Quine, George A. Rinard, Sandra S. Eaton, and Gareth R. Eaton. Combining absorption and dispersion signals to improve signal-to-noise for rapid-scan EPR imaging. *Journal of Magnetic Resonance*, 203(2):305–310, Apr 2010.

[159] Y. Twig, E. Dikarov, and A. Blank. Ultra miniature resonators for electron spin resonance: Sensitivity analysis, design and construction methods, and potential applications. *Molecular Physics*, 111:2674–2682, October 2013.

[160] Y. Twig, E. Suhovoy, and A. Blank. Sensitive surface loop-gap microresonators for electron spin resonance. *Review of Scientific Instruments*, 81(10):104703–104703–11, October 2010.

[161] V. Vins. Technique of production of fancy red diamonds. *U.S. Patent Application 2007/0053823 A1*, 2007.

[162] A. Sils W. B. Westphal. *Dielectric Constant and Loss Data.* Air Force Materials Laboratory, Air Force Systems Command, 4 1972.

[163] A. Wallraff, D. I. Schuster, A. Blais, L. Frunzio, J. Majer, M. H. Devoret, S. M. Girvin, and R. J. Schoelkopf. Approaching Unit Visibility for Control of a Superconducting Qubit with Dispersive Readout. *Physical Review Letters*, 95(6):060501, Aug 2005.

[164] Daniel F Walls and Gerard J Milburn. *Quantum Optics.* Springer, 2007.

[165] Tao Wang, Yong Zhou, Chong Lei, Jun Luo, Shaorong Xie, and Huayan Pu. Magnetic impedance biosensor: A review. *Biosensors and Bioelectronics*, 90:418–435, 2017.

[166] WL Webb. Aircraft navigation instruments. *Electrical Engineering*, 70(5):384–389, 1951.

[167] A. Wickenbrock, H. Zheng, L. Bougas, N. Leefer, S. Afach, A. Jarmola, V. M. Acosta, and D. Budker. Microwave-free magnetometry with nitrogen-vacancy centers in diamond. *Applied Physics Letters*, 109(5):053505, August 2016.

[168] John P Wikswo, John P Barach, and John A Freeman. Magnetic field of a nerve impulse: first measurements. *Science*, 208(4439):53–55, 1980.

[169] Reginald Wilcox, Erik Eisenach, John Barry, Matthew Steinecker, Michael O'Keeffe, Dirk Englund, and Danielle Braje. Thermally polarized solid-state spin sensor. *Physical Review Applied*, 17(4):044004, 2022.

[170] Stefan Wildermuth, S Hofferberth, Igor Lesanovsky, Steffen Groth, Peter Krüger, Jörg Schmiedmayer, and Israel Bar-Joseph. Sensing electric and magnetic fields with bose-einstein condensates. *Applied Physics Letters*, 88(26):264103, 2006.

[171] T. Wolf, P. Neumann, K. Nakamura, H. Sumiya, T. Ohshima, J. Isoya, and J. Wrachtrup. Subpicotesla Diamond Magnetometry. *Physical Review X*, 5(4):041001, October 2015.

[172] R. L. Wood, W. Froncisz, and J. S. Hyde. The loop-gap resonator. II. Controlled return flux three-loop, two-gap microwave resonators for ENDOR and ESR spectroscopy. *Journal of Magnetic Resonance*, 58:243–253, 1984.

[173] Yuzhou Wu, Fedor Jelezko, Martin B Plenio, and Tanja Weil. Diamond quantum devices in biology. *Angewandte Chemie International Edition*, 55(23):6586–6598, 2016.

[174] Ze-Liang Xiang, Sahel Ashhab, J. Q. You, and Franco Nori. Hybrid quantum circuits: Superconducting circuits interacting with other quantum systems. *Reviews of Modern Physics*, 85(2):623–653, Apr 2013.

[175] Bang Yang, Takuya Murooka, Kosuke Mizuno, Kwangsoo Kim, Hiromitsu Kato, Toshiharu Makino, Masahiko Ogura, Satoshi Yamasaki, Marek E. Schmidt, Hiroshi Mizuta, Amir Yacoby, Mutsuko Hatano, and Takayuki Iwasaki. Vector electrometry in a wide-gap-semiconductor device using a spin-ensemble quantum sensor. *Physical Review Applied*, 14:044049, Oct 2020.

[176] Matthias Zens, Dmitry O. Krimer, and Stefan Rotter. Critical phenomena and nonlinear dynamics in a spin ensemble strongly coupled to a cavity. II. Semiclassical-to-quantum boundary. *Physical Review A*, 100(1):013856, Jul 2019.

[177] Chen Zhang, Heng Yuan, Ning Zhang, Lixia Xu, Jixing Zhang, Bo Li, and Jiancheng Fang. Vector magnetometer based on synchronous manipulation of nitrogen-vacancy centers in all crystal directions. *Journal of Physics D: Applied Physics*, 51(15):155102, 2018.

[178] Ning Zhang, Chen Zhang, Lixia Xu, Ming Ding, Wei Quan, Zheng Tang, and Heng Yuan. Microwave magnetic field coupling with nitrogen-vacancy center ensembles in diamond with high homogeneity. *Applied Magnetic Resonance*, 47(6):589, 2016.

[179] Shao-Chun Zhang, Yang Dong, Bo Du, Hao-Bin Lin, Shen Li, Wei Zhu, Guan-Zhong Wang, Xiang-Dong Chen, Guang-Can Guo, and Fang-Wen Sun. A robust fiber-based quantum thermometer coupled with nitrogen-vacancy centers. *Review of Scientific Instruments*, 92(4):044904, 2021.

[180] Xufeng Zhang, Chang-Ling Zou, Liang Jiang, and Hong X. Tang. Strongly coupled magnons and cavity microwave photons. *Physical Review Letters*, 113:156401, Oct 2014.

[181] Zheshen Zhang and Quntao Zhuang. Distributed quantum sensing. *Quantum Science and Technology*, 6(4):043001, 2021.

[182] Yue Zhao, Junhai Zhang, Jiahui Li, Shuangqiang Liu, Peixian Miao, Yanchao Shi, and Enming Zhao. A brief review of magnetic anomaly detection. *Measurement Science and Technology*, 32(4):042002, 2021.